OLYMPUS
Technical Design Report
DRAFT

The OLYMPUS Collaboration
http://web.mit.edu/olympus/

August 31, 2009

Contents

THE OLYMPUS COLLABORATION

Arizona State University, USA
DESY,Hamburg, Germany
Hampton University, USA
INFN, Bari, Italy
INFN, Ferrara, Italy
INFN, Rome, Italy
Massachusetts Institute of Technology, USA
St. Petersburg Nuclear Physics Institute, Russia
Universität Bonn, Germany
University of Colorado, USA
Universität Erlangen-Nürnberg, Germany
University of Glasgow, United Kingdom
University of Kentucky, USA
Universität Mainz, Germany
University of New Hampshire,USA
Yerevan Physics Institute, Armenia

Chapter 1

The Scientific Goals of the OLYMPUS Experiment

1.1 Introduction

Recent determinations of the proton electric to magnetic form factor ratio from polarization transfer measurements at JLab indicate an unexpected and dramatic discrepancy with the form factor ratio obtained using the Rosenbluth separation technique in unpolarized cross section measurements. This discrepancy has been explained as the effects of multiple photon exchange beyond the usual one-photon exchange approximation in the calculation of the elastic electron-proton scattering cross section. Since most of our understanding on the structure of the proton and atomic nuclei is based upon lepton scattering analyzed in terms of the single photon approximation; it is essential to definitively verify the contribution of multiple photon exchange.

In June 2007, our collaboration submitted to DESY a letter of intent to carry out an experiment to definitively determine the contribution of multiple photon exchange in elastic lepton-nucleon scattering. The most direct evidence for multiple photon exchange would be a deviation from unity in the ratio of positron-proton to electron-proton elastic scattering cross sections. The experiment would utilize intense beams of electrons and positrons in the DORIS ring incident on an internal hydrogen gas target at an incident energy of 2.0 GeV and precisely measure elastic scattering at angles about 60° with high statistical and systematic precision. For this experiment we proposed to use the existing Bates Large Acceptance Spectrometer Toroid (BLAST) from MIT [1] and an unpolarized internal gas target as used by the HERMES experiment at HERA.

The letter of intent was favorably reviewed by the DESY Physics Research Committee (PRC) at its Fall 2007 meeting. By May 2008, the experiment had been studied by the DESY machine group and it was determined that the experiment was feasible. Further, it was determined that the proposed experiment can be installed and commissioned in parallel with existing light source operation at DORIS but will require dedicated data taking time. A formal proposal [2] was submitted to DESY in September 2008. It was favorably reviewed by the DESY PRC in October 2008 and formally approved by the DESY Directorate in December 2008, conditional upon the necessary funding being secured. In early 2009, the

institutes of the collaboration have initiated the process to obtain funding for the OLYMPUS experiment from the funding agencies in their different countries.

The OLYMPUS collaboration comprises over fifty physicists from fifteen insitutions in Germany, Italy, Russia, the United Kingdom, and the United States. This document describes in detail the technical design for the proposed OLYMPUS experiment. OLYMPUS is made possible by the availability of much existing equipment ($>$ \$ 5 million investment) from the recently completed BLAST experiment at MIT-Bates. The design of OLYMPUS has been carefully optimized to keep the operating costs low. Three months of dedicated beam time at 2 GeV on the DORIS ring are requested to carry out the OLYMPUS experiment.

The report is divided into eight chapters. Chapter 1 is an overview of the experiment. It presents the physics motivation, describes the principle of the experiment, and the anticipated precision for the measured ratio of cross-sections. Chapter 2 describes the impact on the DORIS ring and the necessary modifications to carry out the experiment. Chapter 3 decribes the OLYMPUS spectrometer which is the existing BLAST spectrometer with some significant modifications. Chapter 4 describes the luminosity monitor, which is essential in determining the ratio of the positron to electron cross-sections. Chapter 5 contains a detailed discussion of the OLYMPUS internal target system. Chapter 6 describes the plans for commissioning and operating the experiment. Chapter 7 details the expected performance based upon a GEANT 4 simulation. Chapter 8 addresses the logistics of the experiment and describes the expected schedule, the necessary budget, and the institutional responsibilities in the OLYMPUS collaboration.

1.2 Physics motivation

In the course of the more than 50 year long history of elastic electron-proton scattering since Hofstadter [3] the separation of the proton's electric and magnetic form factors, $G_E^p(Q^2)$ and $G_M^p(Q^2)$, has been of particular interest. These two functions of Q^2 describe the distribution of charge and magnetism of the proton and it is expected that precise *ab initio* calculations in terms of quarks and gluons will become available in the foreseeable future using lattice QCD techniques [4]. Until the 1990's the experimental method to separate $G_E(Q^2)$ and $G_M(Q^2)$ was based on the procedure by Rosenbluth [5] measuring the unpolarized elastic cross section at fixed four-momentum transfer, Q^2, but with different electron scattering angles and incident beam energies. It was found that the Q^2 dependence of both G_E and G_M, to a good approximation, followed the form of the Fourier transform of an exponentially decaying distribution, namely the dipole form factor $(1 + Q^2/0.71)^{-2}$, implying a ratio of $\mu G_E/G_M \approx 1$ as shown by the open symbols in Figure 1.1 (left panel).

Due to the nature of the Rosenbluth formula

$$\frac{d\sigma/d\Omega}{(d\sigma/d\Omega)_{Mott}} = \frac{G_E^2(Q^2) + \tau G_M^2(Q^2)}{1+\tau} + 2\tau G_M^2(Q^2)\tan^2\frac{\theta}{2} = \frac{\epsilon\, G_E^2(Q^2) + \tau G_M^2(Q^2)}{\epsilon\,(1+\tau)}, \quad (1.1)$$

where $\tau = Q^2/(4M_p^2)$, the transverse virtual photon polarization $\epsilon = [1+2(1+\tau)\tan^2(\theta/2)]^{-1}$, and $(d\sigma/d\Omega)_{Mott} = \alpha^2/(4E^2)\,(\cos^2\frac{\theta}{2}/\sin^4\frac{\theta}{2})(E'/E)$; the weight of G_E in the cross section becomes less at higher Q^2 making the Rosenbluth separation of $G_E(Q^2)$ and $G_M(Q^2)$ at high

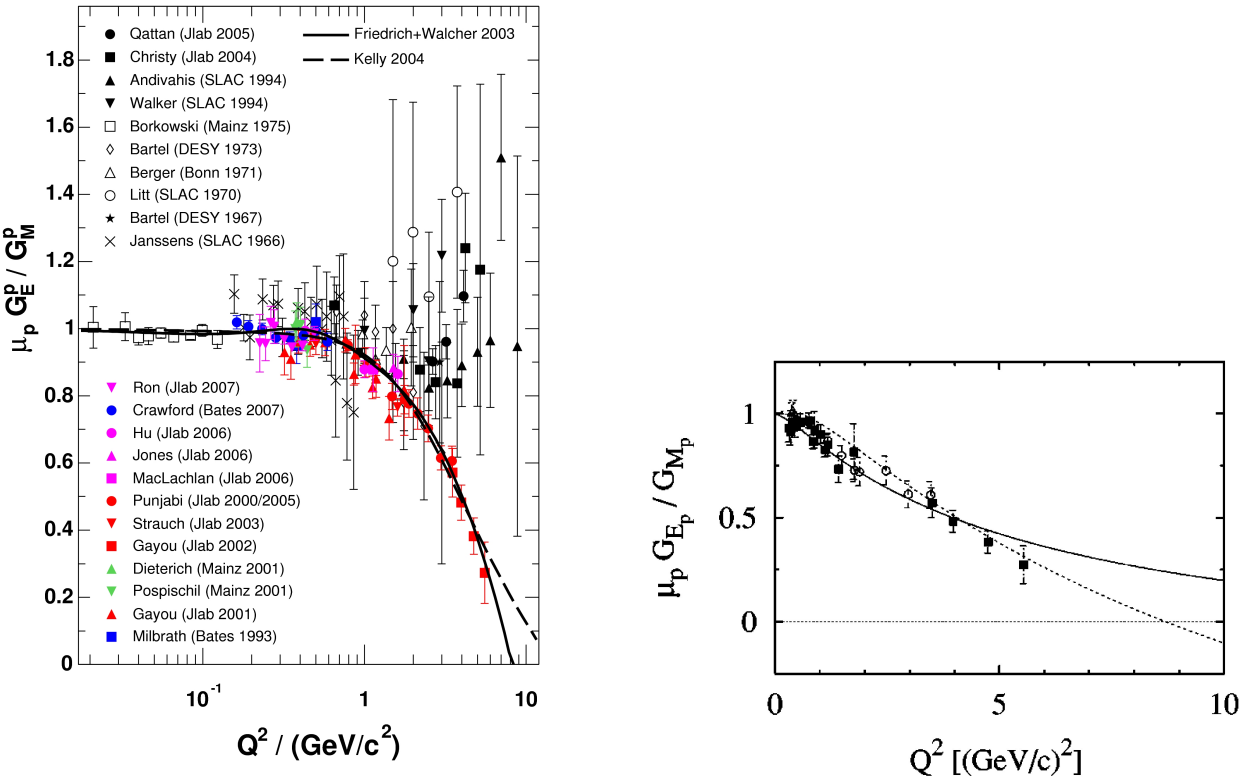

Figure 1.1: Left panel: Proton electric to magnetic form factor ratio from unpolarized measurements (black symbols) using the Rosenbluth method [6, 7, 8] and from double polarization experiments (colored symbols) [9, 10, 11, 12, 13, 14, 15, 16]. Also shown are two recent parameterizations [17, 18]. Right panel: form factor ratio $\mu G_E/G_M$ from recoil polarization compared with calculations by Iachello from 2004 (solid) [19] and 1973 (dashed) [20].

momentum transfer rather difficult. While some experiments reported a scaling of the form factors; others occasionally observed significant deviations of the ratio $\mu G_E/G_M$ from unity. The world data for elastic e-p scattering has recently been compiled by [21]. The most recent Rosenbluth-type measurements have again confirmed the scaling behavior of the proton form factor ratio [7, 8], and additional unpolarized precision measurements are underway [22].

In the late 1990's, development of polarized beams, targets and polarimeters permitted a new way to measure the form factor ratio more directly through the interference of G_E and G_M in the spin-dependent elastic cross section asymmetry [11, 12, 13, 14]. It came as a big surprise when the high precision polarization transfer measurements at Jefferson Laboratory at higher momentum transfers (up to 5.5 $(\mathrm{GeV/c})^2$) gave striking evidence that the proton form factor ratio $\mu G_E/G_M$ was monotonically falling with Q^2 [9]. This Q^2 dependence was dramatically different from that observed with the unpolarized Rosenbluth method. Linear extrapolation would even suggest a node of the electric form factor near 8 $(\mathrm{GeV/c})^2$. Note that this decline of the proton form factor ratio was predicted already in 1973 by calculations

based on vector-meson dominance including the expected node around 8 (GeV/c)^2 [19, 20] shown in Figure 1.1 (right panel). Future recoil polarization experiments at Jefferson Lab will extend the Q^2 range up to 9 (GeV/c)^2 with a new recoil polarimeter [23] and up to 14 (GeV/c)^2 after the 12 GeV upgrade [24].

Alternative measurements of G_E/G_M are based on the spin-dependent asymmetries with polarized beam and target. Experiments of this kind are considered equivalent to polarization transfer and constitute important independent tests to verify the recoil polarization results. Such measurements have recently been performed with the Bates Large Acceptance Spectrometer Toroid (BLAST) at low Q^2 using an internal polarized hydrogen target [16]. The result is consistent with scaling of the form factor ratio, albeit at low Q^2 where no discrepancy between polarized and unpolarized measurements was expected. Another experiment used a frozen-spin ammonia target [15] to extract the form factor ratio at somewhat higher $Q^2 \approx 1.51$ (GeV/c)^2 with a result for $\mu G_E/G_M$ between the unpolarized and polarization transfer data (magenta triangle in left plot of Figure 1.1). Clearly, further measurements are needed to resolve this discrepancy.

The generally accepted explanation for the discrepancy between the recoil polarization and Rosenbluth determinations of the elastic proton form factor ratio is the exchange of multiple (>1) photons during the electron-proton elastic scattering process [25, 35]. This implies that certain lepton-nucleon scattering observables will differ significantly from their one-photon exchange (or first-order Born approximation) expectation value.

Multiple-photon exchange processes will exhibit a characteristic dependence of the elastic lepton-proton scattering cross section on the value of the virtual photon polarization, ϵ. As ϵ decreases, the effects of multiple-photon exchange on the elastic cross section tend to increase in magnitude.

The discrepancy between the recoil polarization and Rosenbluth determinations of the elastic proton form factor ratio grows with increasing Q^2. At high Q^2, the cross section is dominated by magnetic (*i.e.* transverse) scattering. This explains why the effect on the extraction of G_E from Rosenbluth separations can be sizable, while the effect on the cross section at all values of Q^2 is rather modest. At the same time, the form factor ratio from polarization experiments is less affected.

The effect of multiple-photon exchange on the electromagnetic elastic form factors involves the real part of the multiple-photon exchange amplitude. The observable most sensitive to this amplitude is the ratio of the elastic cross section for electron-proton to positron-proton scattering. In the presence of multiple-photon exchange, the cross section for unpolarized lepton-proton scattering contains an interference term between the one- and two-photon amplitudes. This interference is odd under time reversal, and hence has the opposite sign for elastic positron-proton and electron-proton scattering. Therefore, a non-zero two-photon amplitude would result in different cross sections for unpolarized electron-proton and positron-proton scattering.

Figure 1.2 shows the ratio of the two cross sections as a function of the virtual photon polarization, ϵ. The ratio would be unity in the case of pure single photon exchange, *i.e.* the Born approximation. The sensitivity is enhanced at low ϵ, exceeding 4% for $\epsilon \leq 0.4$, provided $Q^2 \geq 2$ (GeV/c)^2. Beyond $Q^2 = 2$ (GeV/c)^2 the Q^2 dependence of the two-photon effect is small, and since the cross section decreases rapidly with Q^2, one would want to keep Q^2 as low as possible for optimized statistics. This is clear in Figure 1.3 which displays the

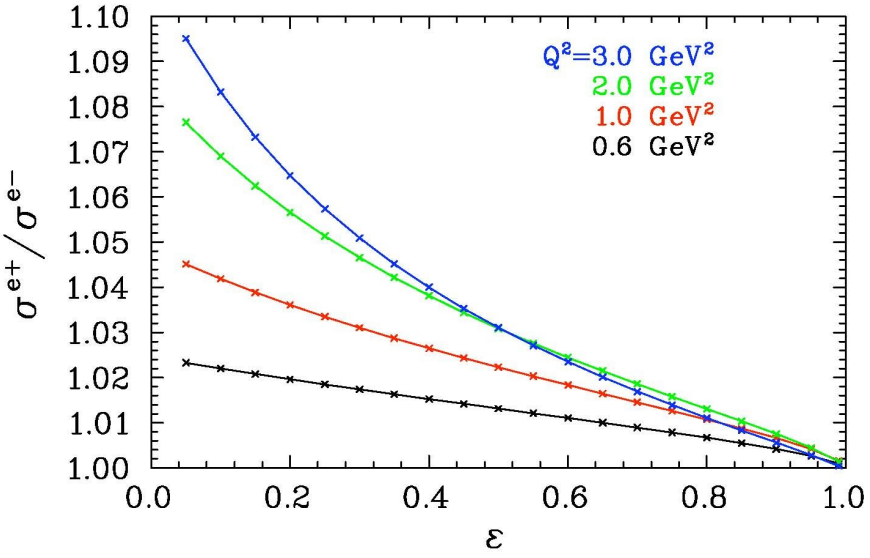

Figure 1.2: Ratio of elastic positron-proton to electron-proton cross section versus virtual photon polarization for given Q^2 [35].

e^+p/e^-p cross section ratio as a function of the scattering angle for three beam energies. Up to scattering angles of about 80°, the cross section ratio is almost independent of the beam energy, and hence of Q^2 for a given scattering angle.

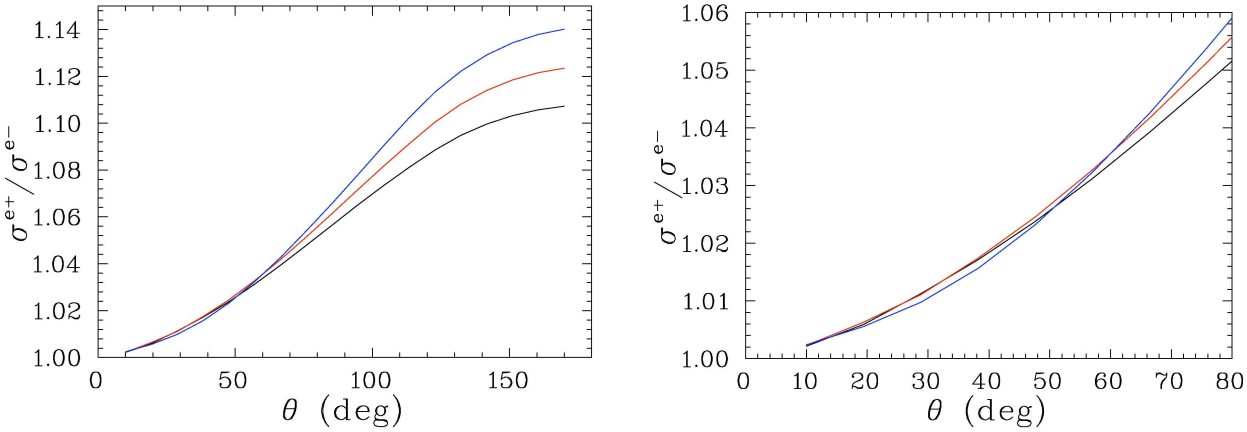

Figure 1.3: e^+p/e^-p cross section ratio as a function of scattering angle, for three beam energies (black=2.0 GeV, red=2.5 GeV, blue=3.0 GeV) [35]. The figure on the right shows the region up to 80° where only little energy dependence of the two-photon effect is evident.

The effects of radiative corrections on the e^+p/e^-p cross section ratio are expected to be negligible. Bethe-Heitler corrections will be identical for positrons and electrons and interference effects which change sign for e^+ and e^-, *e.g.* between the lepton bremsstrahlung process and the proton bremsstrahlung process (a very small effect at these energies) are also expected to be negligible [26].

Figure 1.4 shows the elastic proton electric to magnetic form factor ratio under vari-

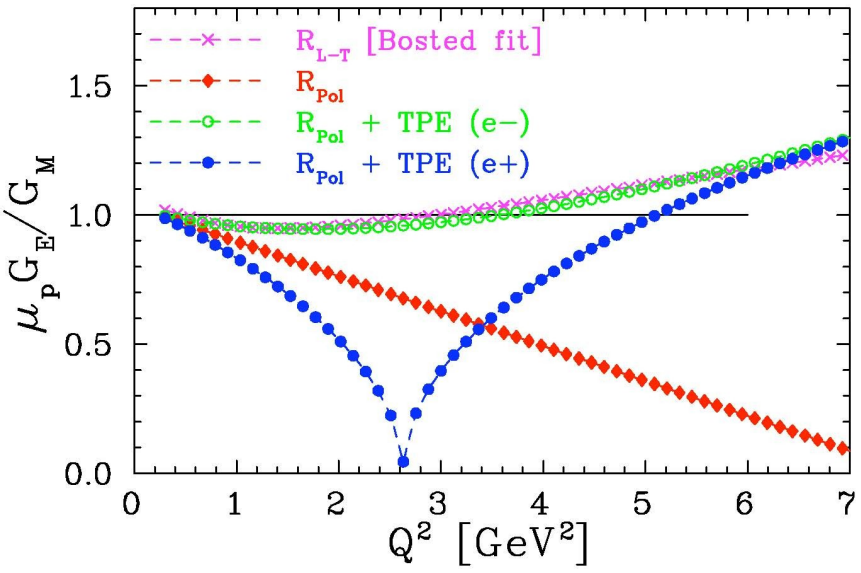

Figure 1.4: Proton electric to magnetic form factor ratio $\mu_p G_E^p/G_M^p$ without (red diamonds) and with two-photon effects calculated for e^-p (green open circles) and e^+p (blue solid circles) Rosenbluth separations [35]. The magenta crosses represent a fit to existing Rosenbluth-separated e^-p data. The electric form factor G_E^p from unpolarized e^+p scattering has a node expected at $Q^2 \approx 2.6$ (GeV/c)^2, with ${G_E^p}^2 < 0$ for $Q^2 > 2.6$ (GeV/c)^2.

ous conditions: The red diamonds correspond to the form factor ratio as determined from recoil polarization, which has only little sensitivity to multi-photon effects. The magenta crosses correspond to the form factor ratio from existing e^-p Rosenbluth separation data (Bosted fit [28]). The green open circles represent the effect of two-photon exchange on the Rosenbluth measurements, using a simple fit to the two-photon correction that explains that discrepancy between polarization and Rosenbluth measurements. The blue solid circles are the result of applying this two-photon correction to Rosenbluth measurements using e^+p scattering. The expected node at ≈ 2.6 (GeV/c)^2 is remarkable. Above 2.6 (GeV/c)^2, one would expect to find negative values for ${G_E^p}^2$ from e^+p Rosenbluth separations.

Previous experiments from the 1960's at SLAC [29] have measured the e^+p/e^-p cross section ratio. However, high-precision measurements with uncertainties of 1% were done only at low Q^2 or very large ϵ, where the multiple-photon exchange effects appear to be small. Measurements at low ϵ had uncertainties of $\approx 5\%$, too large to see conclusive deviations from unity. Recent reanalysis of the (limited) low-ϵ data give an indication of multiple-photon exchange effects, consistent with recent calculations, but only at the three-sigma level [21].

Recently, two new experiments have been proposed to study the e^+p and e^-p cross section ratio: one at Jefferson Lab [30] using a secondary electron/positron beam from a pair production target, and another at Novosibirsk [31] based on stored electron and positron beams incident on an internal unpolarized hydrogen target.

The effect of two-photon exchange on the real part of the lepton-nucleon scattering amplitude can also be investigated by studying the ϵ-dependence of the proton form factor ratio from polarization experiments. Such an experiment has been proposed at Jefferson Lab [32].

Precise mapping of Rosenbluth cross sections in unpolarized e^-p scattering will also reveal any nonlinearities in the ϵ-dependence of the cross section [22].

The imaginary part of the two-photon amplitude would give rise to non-zero transverse single-spin asymmetries, of either the beam (A_n), the target (A_y) or the induced polarization (P_y). These single-spin asymmetries will be studied at Jefferson Lab as well [32, 33].

The elastic form factors of the proton are defined in the context of the Born cross section, *i.e.* the single photon exchange term in the perturbative QED expansion. Corrections for radiative processes involving the incoming and outgoing charged particles must be applied to extract the Born cross section. These corrections are well understood and are calculable in QED.

The use of the intense, multi-GeV stored electron and positron beams at the storage ring DORIS at DESY, Hamburg, Germany in combination with the BLAST detector can produce the most definitive data to determine the effect of multiple photon exchange in elastic lepton-proton scattering and verify the recent theoretical predictions.

1.3 Overview of the OLYMPUS experiment

We propose to measure the ratio of electron-proton to positron-proton elastic cross sections over a range of ϵ with the BLAST detector using an internal, unpolarized hydrogen target and intense stored beams of unpolarized positrons and electrons at an energy of 2.0 GeV at the site of the ARGUS experiment on the storage ring DORIS at DESY in Hamburg, Germany. To carry out this experiment it will be required:

- to operate the DORIS storage ring at an energy of 2.0 GeV,
- to switch between beams of electrons and positrons at a frequency on the order of once per day,
- to relocate the BLAST detector from MIT-Bates to DESY/DORIS, and
- to install an unpolarized hydrogen internal gas target in the DORIS storage ring.

At DORIS, both electron and positron beams can be stored with high intensity and energies up to 4.5 GeV. The DORIS storage ring was operated as a e^+e^- collider until 1993, and is currently used as a source for synchrotron radiation using $\approx$ 150 mA positrons with a lifetime of about 20 hours. Comparable beam intensities for electrons as for positrons are anticipated. With modification of the ring magnet power supplies, it is expected that switching between electron and positron beams in DORIS could be accomplished in about one hour.

With sufficient luminosity and appropriate control of systematic uncertainties, a storage ring experiment with both electrons and positrons incident on an internal hydrogen gas target is the best way to measure the e^+p/e^-p cross section ratio. Simultaneous measurement both at low and at high ϵ with a large-acceptance detector configuration (BLAST) will allow a determination of the ϵ-dependence of the cross section ratio, and hence the size of the multiple photon contribution. Measurement at different beam energies will also enable a

Rosenbluth separation for the positron cross sections for a wide range of four-momentum transfer when the measured e^+p/e^-p ratios are combined with existing Rosenbluth data for elastic electron-proton scattering.

We propose to utilize the existing Bates Large Acceptance Spectrometer Toroid (BLAST) detector system from MIT-Bates. BLAST is a toroidal spectrometer with eight sectors. The two horizontal sectors are instrumented with wire chambers for charged-particle tracking, plastic scintillators for trigger and relative timing, and aerogel-Cerenkov counters for pion rejection. The detector is symmetric about the beam direction and allows for complete reconstruction of coincident elastic events with both electron and proton four-vectors being determined. The symmetry of the detector doubles the solid angle for elastic scattering. The angle acceptance covers approximately 20° to 80° of the polar and ±15° for the azimuthal angle.

The kinematic coverage of the BLAST detector is shown in Figure 1.5 for virtual photon

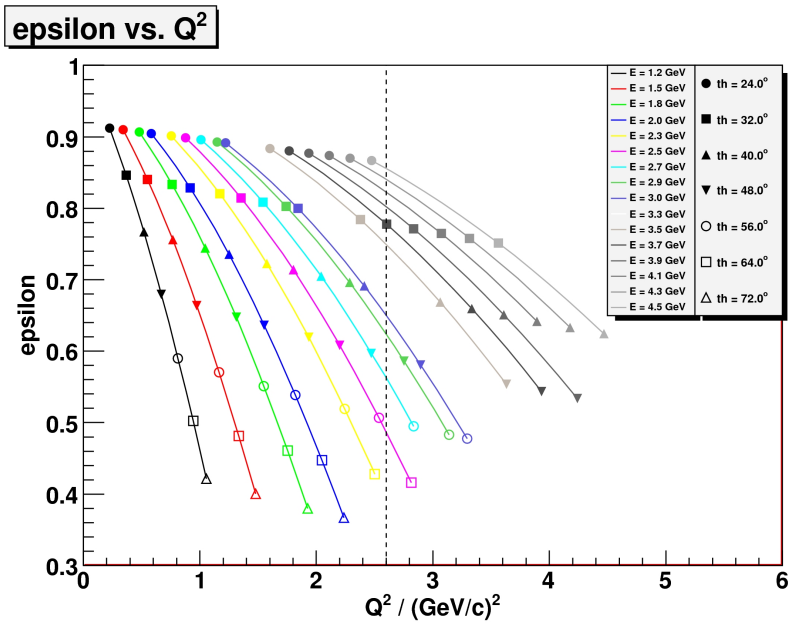

Figure 1.5: Kinematic coverage of ϵ versus Q^2 for the BLAST detector for various beam energies.

polarization ϵ versus Q^2 for different incident beam energies (colors) and scattering angles (symbols) corresponding to the BLAST acceptance. For any given beam energy, the parameters ϵ and Q^2 are kinematically correlated within the large angle acceptance. For the BLAST detector geometry, the acceptance becomes smaller at higher beam energies, thereby setting a lower limit for the reachable value of ϵ since for backward lepton scattering angles the scattered proton is recoiling at decreasing angles and eventually misses the detector system. For the acceptance limitation by BLAST a proton angle $\theta_p > 23°$ was assumed.

As a consequence, the lowest reachable values of ϵ are about 0.4 and are only established at a beam energy of less than 2.3 GeV. At the same time, the beam energy should also not be smaller than 2 GeV in order to maintain a $Q^2 > 2$ (GeV/c)^2.

For a fixed Q^2 of 2.6 (GeV/c)^2 (where the $G_E(e^+)$ node is expected), only beam energies of 2.3-4.5 GeV are appropriate for use with BLAST. At this value of Q^2 the BLAST acceptances for these beam energies are overlapping, suitable to map out the ϵ-dependence of the cross section ratio at fixed Q^2 (similar to a Rosenbluth separation). The lowest beam energy corresponds to the lowest ϵ value for that respective Q^2 value. In combination with existing electron-proton cross sections, a Rosenbluth separation of the positron-proton elastic cross section can be carried out.

The target will be an unpolarized hydrogen gas target confined by a thin walled, cryogenically cooled aluminum tube, similar to that used in the HERMES/DESY and BLAST/MIT experiments. To carry out measurements of the elastic electron-proton cross section at the lowest value of $\epsilon \approx 0.4$ with $\approx 1\%$ statistical uncertainty in about 1 month, a luminosity of $2 \cdot 10^{33}/(\mathrm{cm}^2\mathrm{s})$ will be required for this experiment. Assuming 100 mA circulating electron and positron currents, this implies a target thickness of about $3 \cdot 10^{15}$ atoms/cm^2. Large vacuum pumps will be required to pump away the hydrogen gas so that the lifetime of the stored beam can be on the order of several hours. The Erlangen, Ferrara, and MIT groups have considerable experience in designing, installing and operating such internal gas targets in storage rings [41].

The target thickness will be monitored over time by continuously measuring the pressure and temperature of the reservoir and by an additional flow meter to measure the flux from the buffer. The stored current of positrons and electrons in the ring will be measured with an absolute precision of 1% with a parametric current transformer as was done for BLAST running at MIT-Bates, providing a precise monitor of the luminosity when combined with the gas flow information from the buffer system.

Besides measuring target thickness and beam current separately, we also propose to measure and monitor the luminosity with elastic scattering at low momentum transfer. At low $Q^2 < 1$ (GeV/c)^2, the proton form factors G_E and G_M are known to the 1% level. Moreover, at ϵ close to 1, two-photon effects are expected to be negligible, hence the rate for both e^+p and e^-p elastic scattering is proportional to the luminosity. Since this experiment aims to precisely measure the ratio of elastic cross sections with positrons and electrons scattered from protons, only the relative or ratio of luminosities needs to be known with high precision.

To this extent, we will use a set of position-sensitive counters at a forward angle of about 12° to detect electrons or positrons in coincidence with the recoiling proton at large angle covered by the acceptance of BLAST. At such a forward angle, the field integral of the BLAST toroid is quite small, resulting in almost straight tracks for elastically scattered electrons or positrons. Nevertheless, the curvature of the track will be observed and used to reconstruct the track parameters at the target by using three tracking planes, as in the case of the wire chambers. The forward-angle detector will have to be radiation-hard, capable of handling high rates in the MHz region and has to provide good angular ($< 0.5°$) and vertex resolution (< 1 cm) for the forward tracks.

A promising possibility for the forward detector would be a package of three planar triple-GEM detectors, similar to the COMPASS-GEM [56] and the MIT prototype [57], allowing the lepton tracks to be measured with high resolution. An alternative would be several crossed layers of thin scintillator hodoscopes read out on both ends with fast photomultipliers for good position resolution. The angular resolution of the track should be better than 0.5°,

which corresponds to a spatial resolution requirement of about 2cm. While this modest requirement could already be achieved with a scintillator hodoscope, a higher resolution is required as also the vertex needs to be resolved.

For beam energies between 2.0 and 4.5 GeV, the four-momentum transfer at $\theta_e = 12°$ varies between 0.17 and 0.80 $(\mathrm{GeV/c})^2$, and the virtual photon polarization parameter ϵ is above 0.97. Here the single photon approximation is good to better than 1%. The proton is recoiling with momenta of 400-900 MeV/c at angles of 59°–72°, well within the rear-angle acceptance of the OLYMPUS detector.

The coincidence requirement between the forward detector and BLAST, as well as further kinematic correlations between the lepton and proton track, will suppress backgrounds from any source including random coincidences.

The cross section at low Q^2 and $\epsilon > 0.97$ is large enough to provide $< 1\%$ statistical error for the above configuration in less than 15 minutes for 2.0 GeV energy, indicating the suitability of this setup as a luminosity monitor.

1.4 The Proposed Measurements

Figure 1.6 shows the expected number of counts in any given angle bin and for various beam energies for a canonical run of 500 h at a luminosity of $2 \cdot 10^{33}/(\mathrm{cm^2 s})$ as a function of Q^2. Höhler form factor [52] based cross sections were used for this estimate, good to within 10% for both e^+ and e^- up to $Q^2 \approx 3$ $(\mathrm{GeV/c})^2$. We see that for $Q^2 \simeq 2.6$ $(\mathrm{GeV/c})^2$, the number of counts per angle bin ranges between $\approx 2{\cdot}10^4$ (at 2.3 $(\mathrm{GeV/c})^2$ and smallest ϵ) and $\approx 2{\cdot}10^5$ (at 4.5 $(\mathrm{GeV/c})^2$ and highest ϵ).

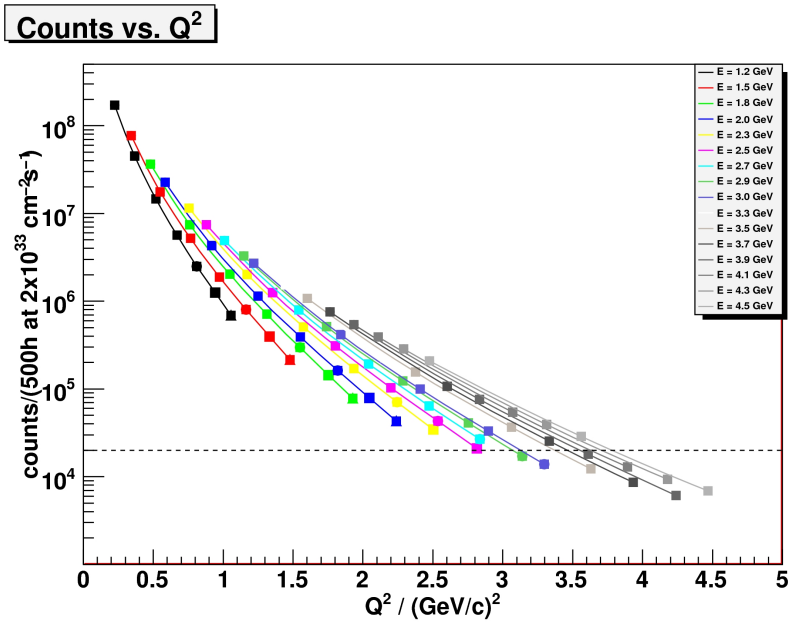

Figure 1.6: Expected distribution of counts per marked angle bin for the BLAST detector for various beam energies, as a function of Q^2. The assumed luminosity is $2 \cdot 10^{33}/(\mathrm{cm^2 s}) \times$ 500 hours.

E_0 [GeV]	Q^2 [(GeV/c)^2]	θ_e	$p_{e'}$ [GeV/c]	ϵ	θ_p	p_p [GeV/c]
4.5	2.6	24.9°	3.114	0.86	38.0°	2.125
3.0	2.6	43.0°	1.614	0.65	31.2°	2.125
2.3	2.6	67.6°	0.914	0.39	23.4°	2.125

Table 1.1: Kinematics for three beam energies and $Q^2 = 2.6$ (GeV/c)^2.

Figure 1.7 shows the expected number of counts in any given angle bin and for various beam energies versus ϵ. Generally, lowest ϵ values at reasonable counts of $> 2 \times 10^4$, as required to provide statistical errors of the cross section ratio of $< 1\%$, are possible down to $\epsilon \approx 0.4$, for which the beam energy should not exceed ≈ 2.5 GeV. At higher energies, the lowest value of ϵ reachable with the rearmost scattering angle increases due to the proton forward angle acceptance limit, while at the same time the count rate decreases. However, also for energies lower than 2.0 GeV, the lowest reachable value of ϵ tends to increase as well due the lepton's rear angle acceptance limit. A beam energy of 2.0 GeV appears to be ideal for the configuration of the BLAST detector to maximize count rate, acceptance and reach in ϵ.

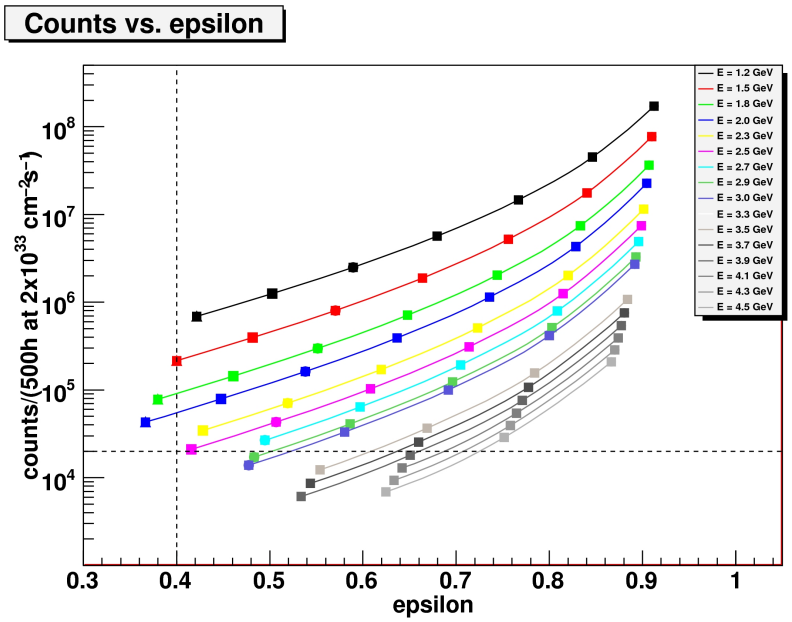

Figure 1.7: Expected distribution of counts per marked angle bin for the BLAST detector for various beam energies, as a function of ϵ. The assumed luminosity is $2 \cdot 10^{33}/(\text{cm}^2\text{s}) \times$ 500 hours.

Measurements at three beam energies, as listed in Table 1.1, can yield precise ratios of e^+p and e^-p cross sections at $Q^2 = 2.6$ (GeV/c)^2 for a wide range of ϵ. The counts for each Q^2 point in the table are in excess of $\approx 2 \cdot 10^4$ counts. In combination with world electron-proton cross section data this would allow for a precise Rosenbluth separation of the elastic positron-proton cross section at a value of Q^2 where the node of G_E^p when probed

E_0 [GeV]	θ_e	$p_{e'}$ [GeV/c]	θ_p	p_p [GeV/c]	Q^2 [(GeV/c)^2]	ϵ	Counts
2.0	24	1.69	56.4	2.45	0.6	0.905	22613100
	32	1.51	48.1	2.26	0.9	0.828	4321570
	40	1.46	41.3	2.07	1.2	0.736	1141960
	48	1.27	35.7	1.89	1.6	0.636	389822
	56	1.10	31.0	1.73	1.8	0.538	162355
	64	0.97	27.1	1.59	2.0	0.447	78744
	72	0.85	23.8	1.47	2.2	0.367	42954

Table 1.2: Kinematics for 2.0 GeV beam energy and count estimate per 8° bin for 500 h at $2 \cdot 10^{33}$ / (cm^{2}s).

with positrons is expected (viz. Fig. 1.4).

For this experiment, however, we propose to run only at one beam energy, 2.0 GeV, to optimize cost and effectiveness of the measurement. At $\epsilon = 0.37$ and $Q^2 = 2.2$ (GeV/c)^2, the effect on $\sigma(e^+/e^-)$ is expected to be of the order 5%. For a 1% statistical error of the cross section ratio, about $2 \cdot 10^4$ counts are required for both electron and positron measurements. For a 500 h measurement each with electron and positron beams, the cross section ratio will be determined statistically to better than 1% throughout the BLAST acceptance. In particular, the precision in the low-ϵ region for Q^2 up to 2.2 (GeV/c)^2 will not be limited by statistics.

It should be emphasized that the large angular acceptance of BLAST includes a wide distribution of ϵ values in a single measurement. Table 1.2 summarizes kinematics and expected count rate per 8° angle bin for the proposed run at a beam energy of 2.0 GeV.

Figure 1.8 shows the projected uncertainties of the e^+p/e^-p cross section ratio as a function of the virtual photon polarization ϵ, assuming a luminosity of $2 \cdot 10^{33}/(\text{cm}^2\text{s})$ and a running time of 500 h for both e^+ and e^-. Also shown are various theoretical predictions for the cross section ratio, evaluated for constant beam energy of 2.0 GeV as a function of ϵ. The black curve corresponds to a parameterization of the two-photon amplitude obtained by fitting the data of polarization transfer and unpolarized cross sections [34]. This curve hence corresponds to the maximum possible signal of deviation of the ratio from unity, when all of the form factor discrepancy is associated with the effects of two-photon exchange. The red curves are derived from a hadronic description of the two-photon exchange amplitude [35, 36]. In the intermediate hadronic state, contributions from the nucleon ground state [35] (red dashed curve) and both the ground state and Δ excited states [36] (red solid curve) are accounted for. The green curves correspond to a dispersion theory ansatz for the elastic contribution [37], which avoids the need for off-shell form factors and is very close to the hadronic prediction. In [38], dispersion relations are used to predict the inelastic contributions to the e^+/e^- cross section ratio at forward angles (shown as green dotted curve). The prediction from a partonic description of two-photon exchange based on Generalized Parton Distributions (GPD) [39] is shown as the blue curves for fixed $Q^2 = 2$ (GeV/c)^2 (solid) and $Q^2 = 5$ (GeV/c)^2 (dashed). Finally, the purple points correspond to predictions of the ratio within a QCD factorization approach [40] for the COZ (squares) and BLW models (circles)

evaluated at various Q^2 values between 2.2 and 4.5 $(\mathrm{GeV/c})^2$. Note that the pQCD and GPD framework is only valid at sufficiently large value of $Q^2 > 2$ $(\mathrm{GeV/c})^2$, while for a fixed energy of 2.0 GeV the large ϵ region would correspond to low $Q^2 < 1$ $(\mathrm{GeV/c})^2$.

The spread of the various theoretical curves is a measure of theoretical uncertainties and underlines the need for precise experimental data of this quantity.

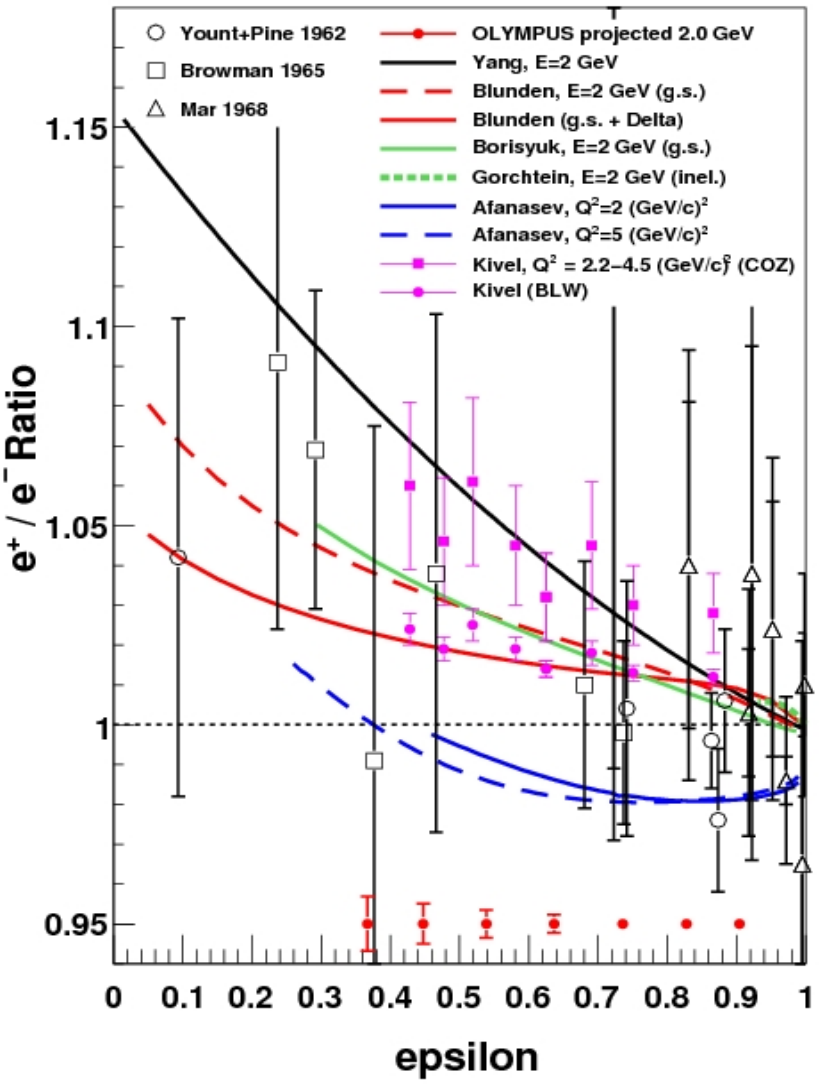

Figure 1.8: Projected uncertainties in the determination of the cross section ratio e^+p/e^-p for the OLYMPUS detector for a beam energy of 2.0 GeV, as a function of ϵ. The assumed luminosity is $2 \cdot 10^{33}/(\mathrm{cm}^2\mathrm{s}) \times 500$ hours each for running with electrons and positrons, respectively. Also shown are several theoretical predictions. Black curve: A parameterization of the form factor discrepancy under the assumption that it is fully caused by TPE [34]. Red curves: A hadronic description of TPE with elastic intermediate state [35] (dashed) and including the Δ resonance [36] (solid curve). Green curves: A dispersion theory ansatz [37] for the elastic intermediate state (solid) and at forward angles for the inelastic contributions [38] (dotted). These above curves have been evaluated for fixed beam energy at OLYMPUS of 2.0 GeV. Blue curves: A partonic description of TPE based on GPDs [39] at constant $Q^2 = 2$ (solid) and 5 $(\mathrm{GeV/c})^2$ (dashed). **The purple points are NOT data but rather a theoretical prediction**: A QCD factorization approach [40] for the COZ (squares) and BLW models (circles) for Q^2 between 2.2 and 4.5 $(\mathrm{GeV/c})^2$.

Chapter 2

The DORIS Storage Ring

The DORIS storage ring at DESY in Hamburg was built in 1974 as an electron-positron collider to investigate the physics of elementary particles. Since then the emphasis of the research shifted towards the use of the emitted synchrotron radiation. In 1993 the last high energy physics experiment, the ARGUS detector, has been removed and DORIS serves as a pure synchrotron radiation source since then. In 2009 it was decided to shut down DORIS at the end of the year 2012. The former BLAST detector is planned to be installed at the same position as the ARGUS detector was placed. The pit with rails to support the detector are still in place, as well as a 11,5m $\times$ 7,5m container which will be used for the electronics and controlling. This container is placed on wheels and moves together with the detector.

The OLYMPUS experiment requires 100 mA of electrons and positrons incident on an internal hydrogen gas target of thickness $3 \cdot 10^{15}$ atoms/cm^2 at an energy of 2.0 GeV. The lifetime of the stored beam is about 1 hour under these conditions. It is required to reverse the charge of the stored beam on a timescale of about 1 hour.

This chapter summarizes the implications of the Olympus experiment on the machine and the operation of DORIS and PETRA.

2.1 Machine physics considerations

2.1.1 Linear optics

Since the DORIS storage ring is designed as an e^+/e^- collider ring, the necessary changes to the present magnet lattice are minimal. It's not feasible to remove the target chamber during the synchrotron radiation runs, therefore the solution has to fulfill the restrictions for both modes of operation. In the present beam optic the beam cross section at the IP is rather large both in horizontal and vertical direction. Since the target cell will have a reduced cross section compared to the standard vacuum chamber, the beta functions must be reduced at the IP. At the same time the optical functions at the synchrotron radiation source points should not change significantly to allow an undisturbed operation of the optical beamlines.

Especially the reduced beam size at the nearby HARWI wiggler (20m downstream) must be conserved, therefore an additional quadrupole on each side of the IP, at $\pm$ 7m is needed to gain the necessary flexibility to match the optic between these two points.

A side effect of this optic is the reduction of the dispersion in the cavities, which should reduce the influence of the synchro-betatron resonances. These are rather strong in the present configuration.

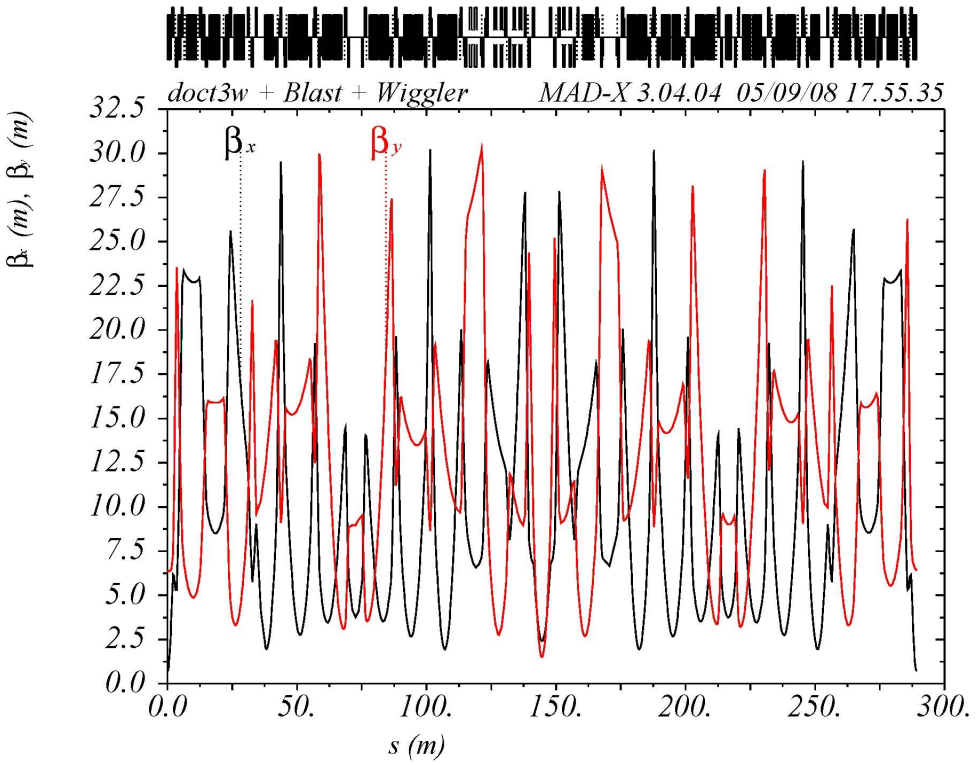

Figure 2.1: Optical amplitude functions of the DORIS storage ring, modified for the gas target IP in the center.

2.1.2 Target cell

The target cell should not be larger than necessary to reduce the needed gas flow at a given target density. On the other hand it must be avoided that particles are scattered at the walls of the cell. To find safe limits for the dimension the limiting existing apertures in DORIS were transformed to the position of the target. To these values 2 mm in each direction were added to allow the insertion of a collimator in front of the cell. The results are given in table 2.2.

	β_x		α_x		β_z		α_z	
Wiggler	doct3w	Olympus	doct3w	Olymp.	doct3w	Olymp.	doct3w	Olymp.
BW1	18.23	17.98	-1.07	-1.04	3.95	4.02	0.398	0.459
BW2	8.69	8.55	-0.038	-0.050	16.19	15.73	-0.022	-0.068
BW3	22.52	22.70	-0.014	-0.033	5.35	5.65	-0.120	-0.133
BW4	0.72	0.71	-0.010	0	6.58	6.41	0.027	0.074
BW5	22.30	22.74	0.037	0.036	5.03	4.94	0.148	0.093
BW6	8.46	8.54	0.033	0.051	15.09	15.90	-0.012	0.004
BW7	18.22	17.92	1.04	1.037	4.17	3.95	-0.451	-0.433
Harwi	12.88	14.56	-0.209	-0.459	4.04	3.21	0.266	-0.414
Roewi	4.78	3.75	0.021	-0.037	11.72	9.01	0.027	0.014
IP	**26.16**	**2.41**	**-0.022**	**-0.001**	**9.707**	**1.52**	**0.048**	**-0.026**

Table 2.1: Comparison of optical functions at center of wigglers – actual standard optic (doct3w) versus optic for Olympus

2.1.3 Beam dynamics

At 4.5 GeV beam energy the single bunch current is limited to 60 mA. The standard filling consists of 5 bunches with a beam current of 140 mA. This limit is given by the maximum allowed heat load due to synchrotron radiation. To reach this current a multi bunch feedback (MBFB) for the horizontal plane is needed. The oscillations in the vertical and longitudinal plane are not strong enough that beam gets lost but are nevertheless damped by MBFB systems. The bandwidth of the MBFBs installed at DORIS is sufficient to work on up to 10 bunches corresponding to a bunch repetition rate of 10 MHz.

The main difference of the planned Olympus operation is the low energy of 2.0 to 2.3 GeV. First the wake fields which act on the bunches are of the same strength or even stronger due to the shorter bunch length, but the effect on the particles scales with $1/E$. The second effect is the reduced radiation damping which results in much longer damping times as seen in table 2.2. Due to these effects it is expected that the current threshold will be lower at low energies.

These effects were investigated during machine studies. In a first test without a longitudinal MBFB a total current of 170 mA in 10 bunches could be reached. At the same time strong longitudinal oscillations were observed which could produce increased particle background and thus reduce the detector efficiency.

During a second test with an improved longitudinal MBFB the oscillations could be damped - the beam was stable in all three dimensions. The current limits reached were 90 mA with 5 bunches and 120 mA with 10 bunches. The beam lifetime was 5 hours. The lower thresholds compared to the first test need further investigations but might well have their reason in the shorter bunch length due to the longitudinal stability.

Further and more detailed studies are planned to examine these effects and find the optimal conditions.

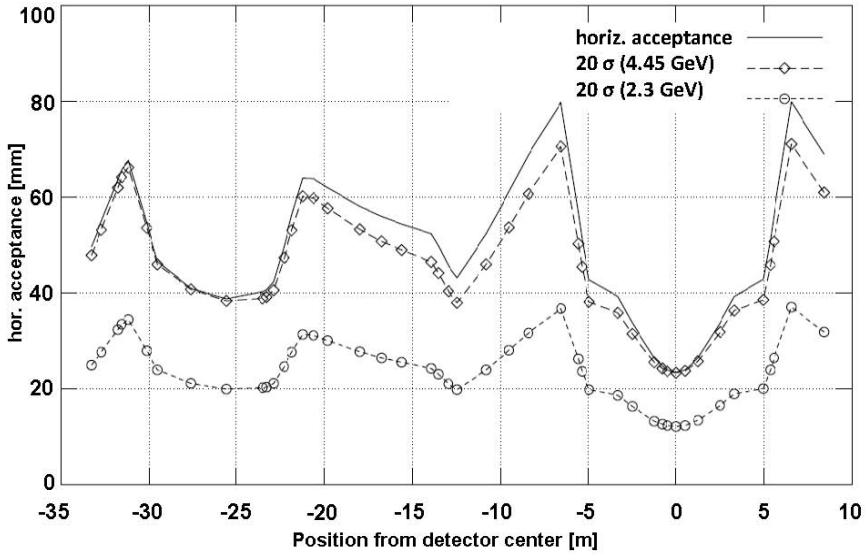

Figure 2.2: horizontal acceptance scaled with beta functions and horizontal 20 σ beam sizes

2.2 Hardware modifications to DORIS

The Olympus detector should be placed at the former ARGUS IP. The space for the detector is still available as well as the rails to support the detector which allow to build up the detector in the hall and move it into the ring at a later stage. Indeed the ARGUS detector is still present in the hall as part of an exhibition but will be disassembled and removed from the hall at the end of the year 2009.

2.2.1 Quadrupoles

To reach more flexibility for the matching of the optic, an additional pair of quadrupoles at 7 m on each side of the IP would be installed. The quadrupoles of the standard DORIS type are existent. In order to increase the gradient of the quadrupoles, the bore radius has to be reduced. This has already been done for most of the DORIS quads by adding machined pole pieces. There are still 24 pole pieces available and the 6 quadrupoles for the IP region will be modified in 2009. It is planned to replace the 4 existing quadrupoles in the ring in winter 2009/2010.

2.2.2 Polarity Switching

One of the key features of the Olympus experiment is the frequent switching between the particle polarities.

The pre accelerators, namely the linear accelerator, the accumulator ring and the DESY synchrotron are already able to switch between electrons and positrons within approx. 10

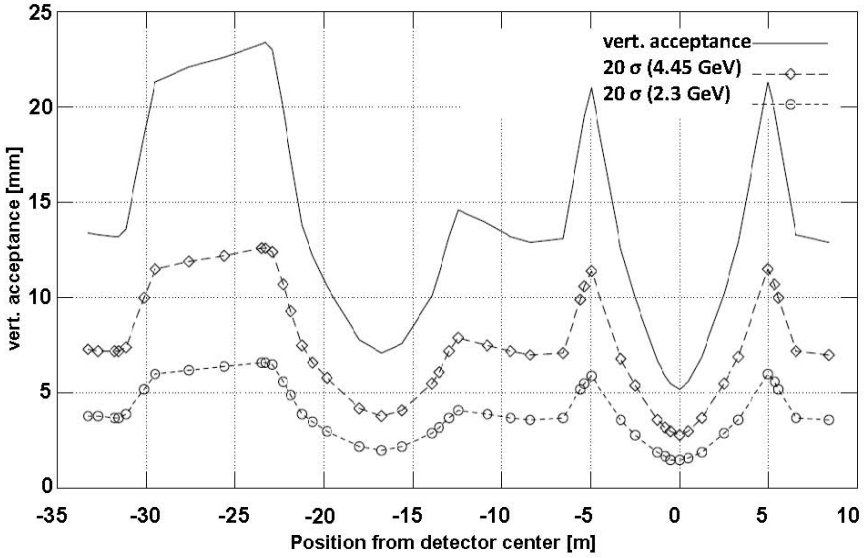

Figure 2.3: vertical acceptance scaled with beta functions and vertical 20 σ beam sizes

minutes. This is not the case for the extraction from DESY synchrotron to DORIS, the transport line and the DORIS ring itself.

- The high voltage pulse forming power supplies for the DESY extraction and the DORIS injection kicker have to be rebuild. A modification is not possible here. The design for these is available in house.
- The septa magnets for the DESY extraction and DORIS injection can be modified to serve as bipolar devices.
- There are 46 main magnet power supplies for the transport line and DORIS. Twelve of those are already bipolar devices. The 10 devices which provide up to 270 A, will be equipped with polarity switches which are still available from HERA. The remaining 24 devices need new switches, 14 switches for 400 A and 10 switches for up to 800 A.

2.2.3 RF-Cavities

The place in the storage ring is now occupied by two cavities, which can be moved upstream to 26 m before the IP, where 2 identical cavities have been removed some years ago.

The space for the cavities, the openings to the cellar for the RF-wave guides and partly the water cooling installation are still available.

2.2.4 Vacuum system

The vacuum system within the detector region is described elsewhere. On each side of the detector a vacuum valve will separate the IP-region from the rest of the ring. One adapter

Beam Energy [GeV]	2.0	2.3	4.5
Max Beam Current [mA]	140		
total charge [nC]	135		
No. of particles	8.4 x 10^{11}		
circumference [m]	289		
Beta-x IP	$<$ 2.7 m		
Beta-z IP	$<$ 1.5 m		
hor. Dispersion at IP [m]	-0.5		
acceptance projected to target	25 mm x 6 mm		
Target cell	27 mm x 8 mm		
Energy acceptance	$>$ 0.8%		
hor. Emittance [nm]	91	119	440
hor. beam size (1σ) at Target[mm]	0.55	0.63	1.2
vert. Emittance (5% coupl.) [nm]	4.5	6.0	22
vert. beam size (1σ) at Target[mm]	0.09	0.11	0.21
cavity voltage [MV]	3.6	3.6	7.2
energy spread (1σ) [%]	0.049	0.056	0.11
bunch length (1σ) [mm]	7.4	9.2	18
hor. damping time [ms]	29.0	19.1	2.6
vert. damping time [ms]	27.6	18.1	2.5
long. damping time [ms]	13.5	8.8	1.2

Table 2.2: Main Parameter

chamber on each side has to be constructed to connect the ring and the detector vacuum system.

Two scraper section are already installed at 9.5 m and 16.7 m before the IP, which can be used to reduce the particle background.

2.3 Hardware modifications for the OLYMPUS detector

2.3.1 Toroid

For powering the toroid of Olympus a power supply is needed with 7000 A DC current output. There is a power supply available at DESY for this current which was used for the PETRA storage ring. A 10 kV connection is also available outside the DORIS hall. To power the toroid magnet the following work has to be done:

- A 10 kV to 480 V transformer has to be installed. The transformer is available but the foundation for it has to be prepared.
- The power supply has to be moved and installed at the DORIS hall.
- A polarity switch for 7000 A (from HERA) has to be installed.

- The cabling from the transformer to the power supply and to the toroid has to done.
- The power supply will get a water cooling.
- Cabling work and software changes to control the power supply have to be done.
- The toroid has to be connected to the water cooling circuit.

For the cooling of the toroid a water flow of about 45 m^3 per hour at about 4 bar differential pressure is needed. Two water pipes with 200 mm diameter to the detector pit are still available and are ready to be used. The water pump presently connected to these tubes delivers a lower water flow with a pressure of 12 bar. For the toroid operation it's either necessary to buy and install a new pump or to use a second pump in parallel, which is presently used as spare. The high pressure must be reduced before the toroid. Some 20 m tubes in this circuit have to be replaced, since they are of a minor cross section.

The former Argus IP region fits perfectly for the Olympus detector. The massive concrete walls of the DORIS tunnel start at 3.6 m from the IP on each side which leaves enough space for Olympus. The rails of Argus are narrower and lower than needed for Olympus - therefore the support for the Olympus detector will be changed to fit the rails.

Modifications are necessary on the outside of the DORIS tunnel where the space is presently used for a workshop. This has to be modified to obtain the space needed for the detector.

Around the detector a new shielding will be build with blocks of concrete 1m thick. This shielding is sufficient to allow free access to the DORIS hall.

2.4 Operational issues

2.4.1 Test phase

During the first test phase the detector will be checked outside the DORIS Tunnel. The detector is free accessible at any time and the DORIS operation for synchrotron radiation is not affected at all.

During the second phase the detector is installed in its final position in the DORIS tunnel. Most of the time there will be synchrotron radiation runs, which must not be disturbed by detector tests. Therefore the energy is fixed at 4.5 GeV and it's not possible to fill the target cell with gas. However there will be about 4 full days during service weeks, where operation of the detector under nominal conditions can be tested.

2.4.2 Data taking

In the year 2012 there will be two periods for Olympus running. One period of 4 weeks after the winter shutdown and 9 weeks at the end of the year.

Due to the frequent switching between electrons and positrons a parallel operation with the PETRA storage ring, which uses the same pre accelerators, is more or less excluded.

According to the present planning, PETRA will run in Top-Up operation all the time. Since the polarity change at LINAC, PIA and DESY takes about 5 minutes, the injection into DORIS with different particles than at PETRA would interfere with the PETRA operation.

At the end of the year 2012 there will be a longer PETRA shutdown to install additional beam lines. The long Olympus run will be scheduled during this time.

2.4.3 Top up option

Since the injection happens at full energy, one could inject new particles frequently to keep the beam current nearly constant. This would increase the mean current and one could accept an even shorter lifetime than the assumed 0.7 hours.

Presently it's assumed that the unavoidable particle losses at injection would damage the drift chambers thus prohibiting this mode of operation. This will be tested during the commissioning phase. If the detector can accept the higher trigger rate and the background, one could increase the target density and luminosity.

2.5 Radiation protection

Running DORIS at full current with a lifetime of 0.4 to 0.7 hours will increase the particle losses by a factor 30 compared to normal synchrotron radiation runs. Similar low lifetime has been seen during bake out periods after the installation of new vacuum components. The main loss mechanism is via the loss of energy by beam gas scattering. Therefore most of the particles will be lost after the first bending magnets and at the most stringent aperture limitations. The present shielding of DORIS is sufficient for these conditions.

2.5.1 Protection of the permanent magnet material

A significant part of the particles will be lost at the entrance of the wiggler chambers, namely the Harwi and the BW1 wigglers since these are the tightest vertical aperture limitations. To protect these devices they should be moved away from the beam pipe, which is possible without hardware modifications. The devices have a build in air cushion system for easier retraction. An alternative is the installation of a lead shielding of about 10cm, which corresponds to about 20 radiation lengths.

2.6 Synchrotron radiation and the OLYMPUS collimation system

2.6.1 Introduction

Synchrotron radiation can pose several problems for experiments at electron storage rings, and care must be taken in OLYMPUS to ensure that synchrotron photons are absorbed or

deflected away from the detectors and that the synchrotron power is effectively dissipated. all without reducing the lifetime of the ring. Two upstream scrapers can be used to block some synchrotron radiation, while the fized collimator in front of the target cell will shield the target cell

Two calculations have been made in order to gauge how much synchrotron radiation will be produced by the last upstream dipole of DORIS. A computer lattice calculation was performed by Boris Nagorny [43, 44], while an analytic calculation was performed by Axel Schmidt [45]. The two calculations show close agreement and so the latter was further used to gauge the design of the fixed collimator and the positioning of upstream scrapers.

The results of these calculations show that synchrotron radiation will be rather insignificant when DORIS is operated at 2 GeV. However, significant radiation will be produced if the ring is operated at 4.5 GeV. Without the upstream scrapers, the collimator will see on the order of 120 W of synchrotron power from the last dipole (not including the upstream quadrupoles in the final straight section). Using the upstream scrapers to intercept some of this radiation can reduce the power on the collimator by as much as a factor of six.

2.6.2 Calculations

Lattice Calculation

The computer calculation from [43, 44] models the emittance and optices of the DORIS ring on a lattice. The results are shown in figures 2.5 and 2.6. Notice that the synchrotron fan is wider vertically at 4.45 GeV than at 2 Gev. One would intuitively expect a narrower fan at higher energy. The wider fan at 4.45 GeV is likely because of the higher vertical spread of the electron beam at higher energy.

Analytic Calculation

This calculation [45] assumes a zero-emittance beam travelling along an ideal circular orbit, emitting radiation only in the forward direction. The final dipole has a constant radius of curvature R, and has no fringe field. A distance L downstream from the dipole is an aperture with half-width W. In the limit $W \ll L$, then the total power through the aperture can be given by:

$$P = \frac{Ie\gamma^4 W}{6\pi\epsilon_0 RL} \tag{2.1}$$

One can also calculate the photon rate through the aperture, using this equation taken from [46]:

$$N = \frac{15\sqrt{3}P}{8E_c} \tag{2.2}$$

where E_c is the critical energy given by [46]:

$$E_c = \frac{3c\gamma^3\hbar}{2R} \tag{2.3}$$

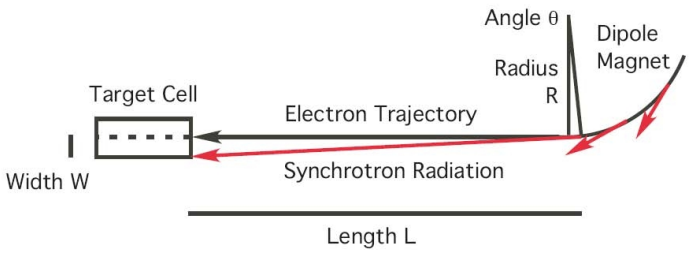

Figure 2.4: Electrons moving from right to left produce synchrotron radiation (red). Inside angle θ the radiation will hit the cell at the far right.

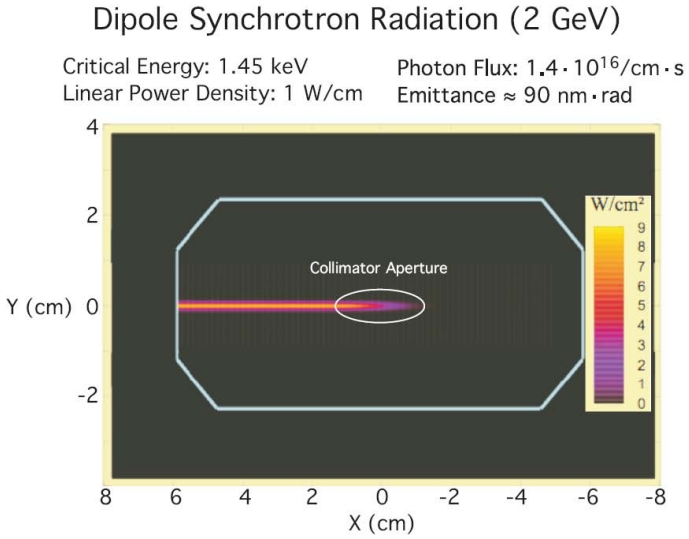

Figure 2.5: The results of Nagorny's calculation at 2 GeV modified from [44]

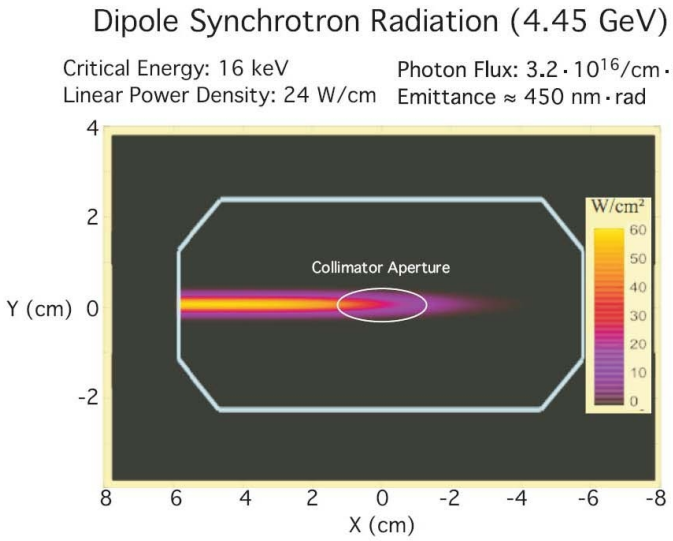

Figure 2.6: The results of Nagorny's calculation at 4.45 GeV modified from [43]

Comparison

To compare the results of equations 2.1, 2.2, and 2.3, the following numbers were used: $R = 12.18$ m [47], $I = 140$ mA [43], $\gamma \approx 3914$ at 2 GeV, and ≈ 8708 at 4.45 GeV. The distance from the last dipole to the front of the target cell is 32.7 m, and the half-width of the target cell is 12.5 mm [48], making the angular opening of the target cell 0.38 mrad.

At both energies there is reasonable agreement, justifying the use of the hand calculation for making other estimates of synchrotron radiation.

2 GeV

At 2 GeV, the computer calculation resulted in linear power density of 1 W/cm, and a photon rate of $1.4 \cdot 10^{16}$ Hz passing through the target, while by hand, the linear power density was 0.79 W/cm, with 0.99 W and $1.38 \cdot 10^{16}$ Hz passing through the target.

4.45 GeV

At 4.45 GeV, the computer calculation resulted in a linear power density of 24 W/cm, with 23 W of power and a photon rate of $3.2 \cdot 10^{16}$ Hz passing through the target. The hand calculation resulted in a linear power density of 19.4 W/cm, with 24.2 W and $3.07 \cdot 10^{16}$ Hz passing through the target.

Critical Energy

The energy spectrum of synchrotron radiation is peaked near a critical energy. Both the calculations confirm that the critical energy will be 1.6 keV at 2 GeV and 16 keV and 4.45 GeV [43, 44, 45]. This means that at both energies the synchrotron radiation produced by DORIS will fall largely in the soft X-ray range.

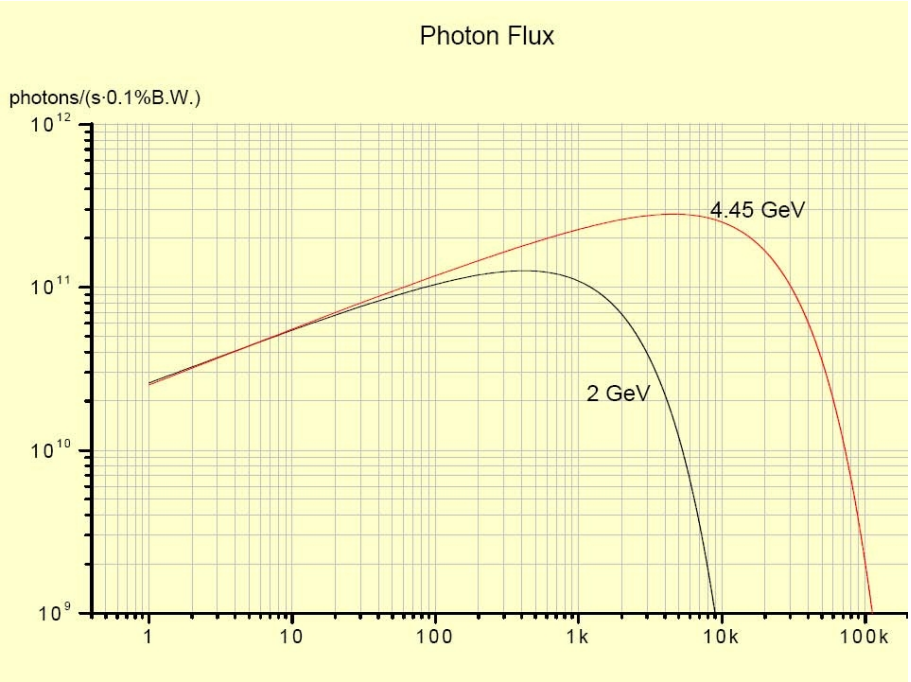

Figure 2.7: the synchrotron radiation spectra at 2 GeV and 4.45 GeV taken from [44]

2.6.3 The Collimator and Scrapers

Estimate of the Incident Power

The fixed collimator will shield the target cell from synchrotron radiation, but in doing so must be designed to dissipate the incident synchrotron power. Using the hand calculation, a quick estimate of the incident power can be made. Assuming a half-width of 7.5 cm for the collimator, at a length 32.7 m from the last dipole, and remembering to subtract the power through the aperture, one finds:

$$\begin{aligned} P &= 4.94\,W\ (E = 2\,GeV) \\ P &= 121.2\,W\ (E = 4.45\,GeV) \end{aligned}$$

It is important to note that this power estimate only takes into account the upstream dipole magnet. The upstream quadrupoles will also produce synchrotron radiation, though most of it will pass directly through the collimator aperture. It is also important to note that this estimate is extremely conservative because the collimator was assumed to be very wide.

Immediately one notices that at 2 GeV, power dissipation from the collimator is not much of a concern at all. However, at 4.45 GeV, a more significant problem is faced.

Positioning of the Upstream Scrapers

There are two upstream scrapers, positioned 16.2 m and 23.5 m from the final dipole. The scrapers consist of water-cooled copper rods, each with a 30 mm diameter. Either scraper

can be turned to scrape the beam vertically or horizontally. Currently, the downstream scraper is designated as the vertical scraper.

The farther the scrapers are pulled in, the more they will intercept synchrotron radiation and reduce the power incident on the collimator. However, if they are pulled in too far, they will begin to hit the beam and cause significant attenuation of the lifetime of the ring. Ideally, the scrapers will be pulled in as far as possible without attenuation of the lifetime, and this positioning must be determined experimentally. For the purposes of making a calculation, pulling the scrapers into the 6σ beam width is a reasonable assumption of the final scraper position. The beam widths were taken from [48].

2 GeV

The horizontal upstream scraper can be pulled in to the beam's 6σ half-width of 7.2 mm. In this position, 1.15 W will pass through the aperture. Since 0.99 W pass through the target cell, that leaves 0.16 W incident on the collimator. A vertical downstream collimator can be pulled all the way in to 1.1 mm half-width but will not greatly reduce any synchrotron power.

4.45 GeV

The horizontal upstream scraper can be pulled in to the beam's 6σ half-width of 16 mm. In this position, 62.6 W will pass through the aperture. Since 24.2 W pass through the cell, that leaves 38.4 W incident on the collimator. The vertical downstream scraper can be pulled in to 2.4 mm half-width but will not greatly reduce any synchrotron power. Still, this is a much more manageable amount of power and could be easily cooled away by water cooling.

Alternatively, the downstream scraper could be turned horizontally and pulled in to a half-width of 17 mm. In this position, the downstream scraper will intercept 16.7 W, leaving just 21.7 W on the collimator. This power reduction may be worth the loss in vertical scraping.

Design of the Fixed Collimator

The proposed target cell will be an eliptic cylinder, 600 mm long, 9 mm high, 27 mm wide. The collimator should therefore have an aperture 7 mm high, and 25 mm wide. It should be made of a heavy metal with desirable properties under vacuum, like Tungsten. The radiation length of Tungsten is 3.5 mm, so 10 cm ($\approx$ 29 radiation lenghts) will be a more than sufficient thickness.

2.6.4 Conclusion

The synchrotron radiation generated by DORIS will only be of consequence during runs at 4.5 GeV. At 2 GeV, a few watts of power will be generated, but it will be easily intercepted and dissipated. In order to run OLYMPUS at a higher beam energy, there are measures that need to be taken: the scrapers must be pulled in tightly, the collimator must be properly designed and cooled.

2.7 Lifetime of the stored beam

We can estimate the beam lifetime in DORIS based on a simple model for losses accounting for bremsstrahlung, Moller and Rutherford scattering [49]. The current aperture at DORIS is limited by an undulator with an 11 mm gap, allowing only for a vertical emittance of about 7 mm-mrad. The momentum acceptance of DORIS (or bucket size) is estimated with 0.8%. The lifetime without any target in the current operation mode as a light source is on the order of 20 h. Figure 2.8 shows the expected partial lifetimes due to the various above

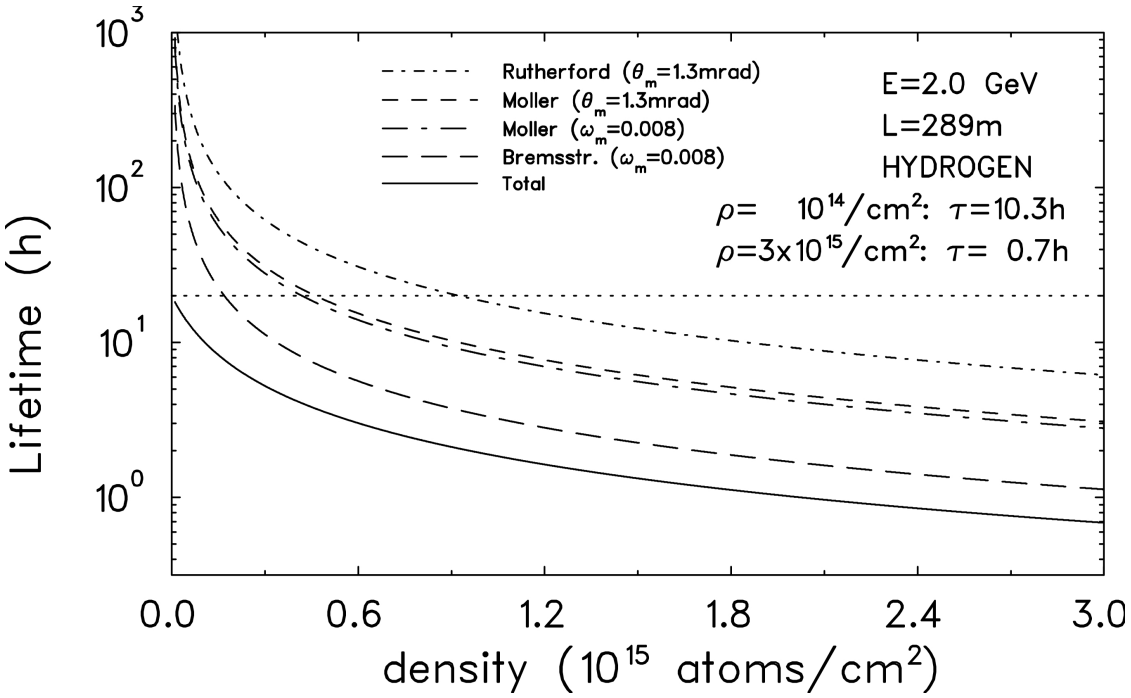

Figure 2.8: Expected beam lifetime in DORIS as a function of the target thickness. Based on a lifetime of 20 h without target (dotted line), the lifetime is reduced by Rutherford and Moller scattering and bremsstrahlung due to the given aperture limits (angle acceptance θ_m and momentum acceptance ω_m).

mentioned processes that are causing losses, along with the resulting lifetime. It is assumed that the insertion of a target cell does not further limit the aperture. With a beta function sufficiently small at the location of the target, which can be achieved with a set of quadrupole magnets upstream and downstream of the internal target, this is a realistic assumption. The expected lifetime at a beam energy of 2.0 GeV amounts to 10.3 h for a target thickness of 10^{14} atoms/cm^2 and 41 min for the required thickness of $3 \cdot 10^{15}$ atoms/cm^2. The momentum acceptance is still the dominant limitation. In comparison, the lifetime at MIT-Bates with a target thickness of $5 \cdot 10^{13}$ atoms/cm^2 was about 30 minutes.

Chapter 3

The OLYMPUS Spectrometer

The OLYMPUS experiment will take advantage of the existing BLAST detector which was successfully operated at the MIT-Bates Linear Accelerator Center. The BLAST detector as it was configured at MIT-Bates is shown in Figure 3.1. It was situated on the South Hall

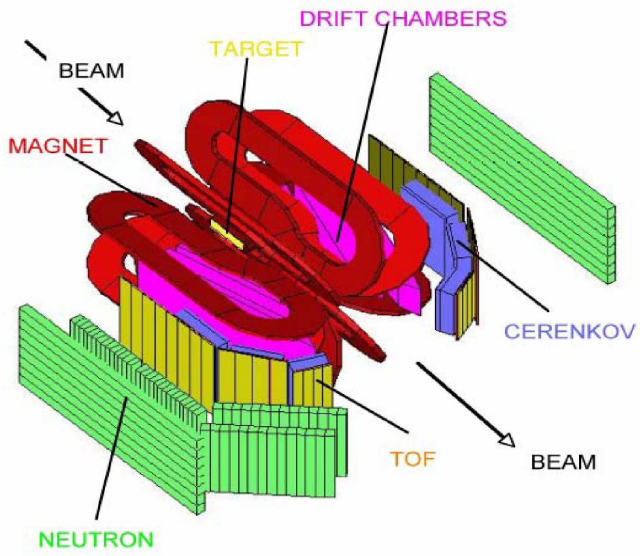

Figure 3.1: Schematic of the BLAST detector showing the main detector elements.

storage ring just downstream of the injection point. The detector was based upon an eight sector, toroidal, magnetic field. The two horizontal sectors were instrumented with detector components while the two vertical sectors were used by the internal targets and the vacuum system for the beamline.

The detector configuration we propose for OLYMPUS will use the BLAST toroidal magnet and instrument the horizontal sectors with the BLAST wire chambers and time of flight scintillators. As such the detector will be left/right symmetric. The drift chambers will provide charge particle tracking to determine the charge, momentum, scattering angles, and

vertex for the charged particles produced. The time of flight scintillators will determine the relative timing of the reaction products and provide the trigger timing for the detector system.

In addition to the toroid magnet, wire chambers, and time of flight scintillators from the BLAST detector some new detector components and upgrades are planned to improve performance and address the requirements of the OLYMPUS experiment. Specifically we propose adding a GEM detector between the target cell and wire chamber in each sector to provide an additional space point for track reconstruction. We also envisage a set of three small detectors at forward angles to monitor the luminosity of the experiment during running. This will be important for normalising the statistics obtained for the different combinatin of electron/positron and magnet polarity. A simple schematic of the OLYMPUS detector configureation is shown in figure 3.2.

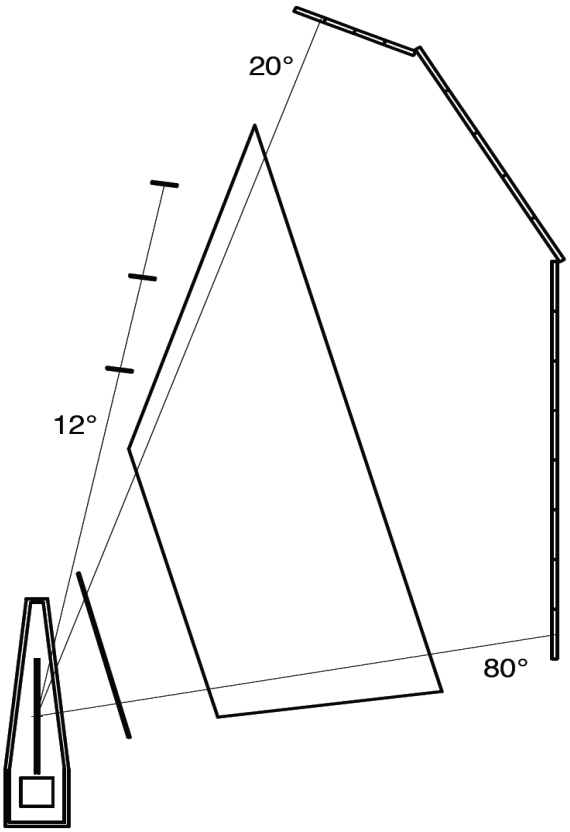

Figure 3.2: Schematic top view of the OLYMPUS experiment showing the scattering chamber with collimator and target cell and the detector components for a single sector.

The BLAST detector is particularly well suited to the proposed measurements of the OLYMPUS experiment. The angular coverage of the BLAST tracking detectors, 20°–80° in polar angle and ±15° in azimuthal angle is well matched to the kinematics for elastic *ep* scattering at 2 GeV as proposed for OLYMPUS. This can be seen in Figure **??**. showing the proton polar scattering angle as a function of the electron scattering angle for elastic *ep* scattering (red curve). The angular acceptance of the detector shown by the green lines

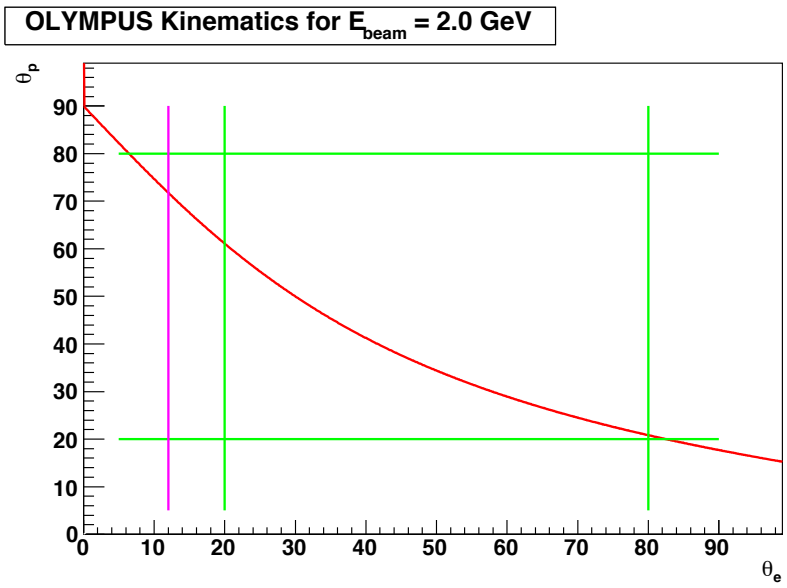

Figure 3.3: Polar scattering for the proton, θ_p versus that of the electron, θ_e for elastic ep scatering (red curve). Green lines represent the acceptance of the BLAST detector and the magenta line represents the angle for the luminosity detector.

nicely matches the elastic ep scattering angles. Furthermore, for electrons scattered into the luminosity detectors at 12° the corresponding protons are also in the detector acceptance.

For reference the momentum for both electron and proton, Q^2, and ϵ ranges as a function of the electron polar scattering angle are given for elastic ep scattering at 2.0 GeV in Figures 3.4, 3.5, and 3.6. The acceptance of the detector is again represented by the green lines and the magenta line represents the angle for the luminosity monitor.

The following sections describe the BLAST detector and proposed detetcor upgrades in greater detail.

3.1 Toroidal Magnet

The toroidal magnet shown in Fig. 3.7 was designed and assembled at MIT-Bates. A toroidal configuration was chosen to ensure a small field along the beamline to minimize effects on the beam transport and also to have small gradients in the region of the target cell. The magnetic field in the region of the drift chambers was used to momentum analyze the charged particles produced during the experiment. It also minimized the number of low energy charged particles reaching the detectors.

The toroid consists of eight copper coils placed symmetrically about the beamline. Each coil consists of 26 turns of hollow, 1.5 inch square copper tube organized into two layers of 13 turns. The copper tubes are wrapped with a fiberglass tape and then potted with epoxy resin. The coils are cooled by flowing water through the hollow conductors. During the BLAST experiment the normal operating current was 6730 A resulting in a maximum field around 3.8 kG.

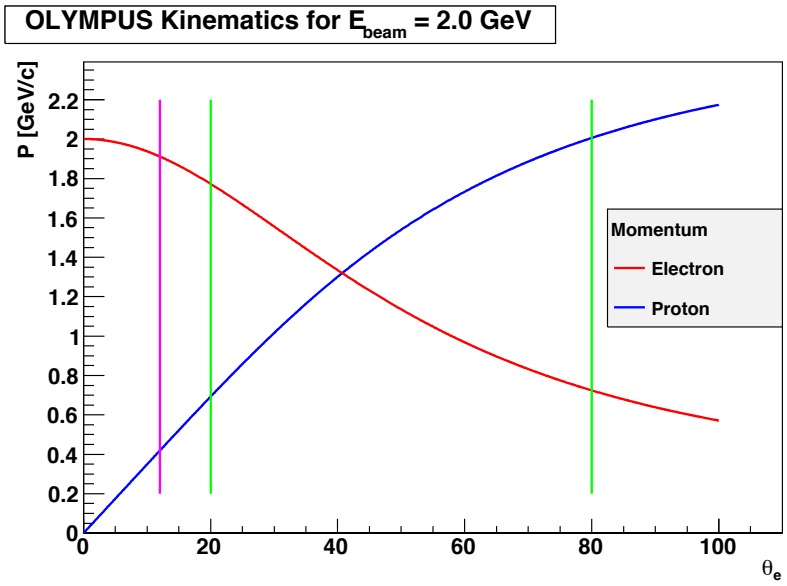

Figure 3.4: Momentum for the electron and proton as a function of the electron polar scattering angle.

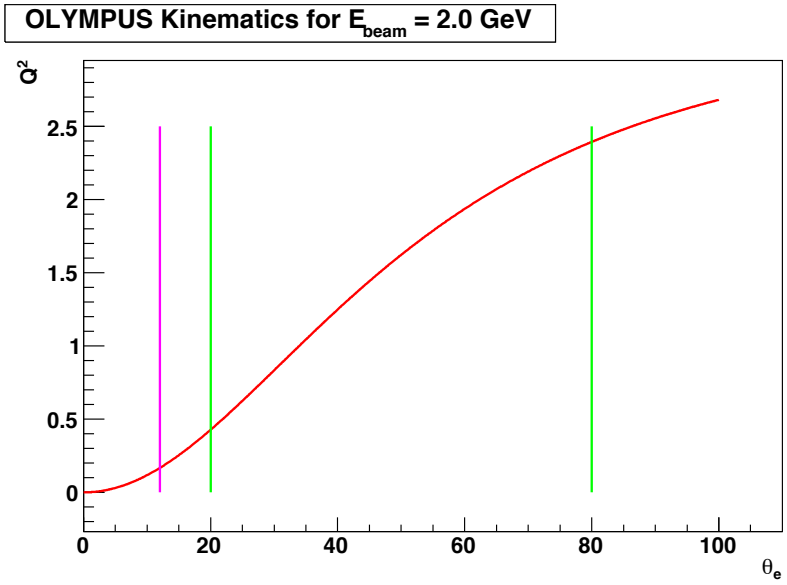

Figure 3.5: Q^2 as a function of the electron polar scattering angle.

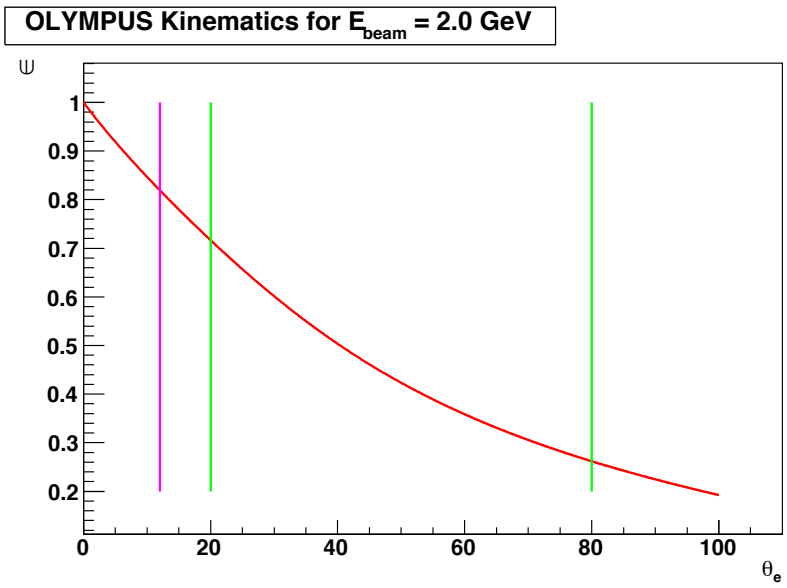

Figure 3.6: ϵ as a function of the electron polar scattering angle.

Before the detectors were installed, the magnetic field was carefully measured particularly along the beam axis and in the target region [53]. The coil positions were adjusted to minimize the field along the beamline and gradients at the target. After this was done a systematic mapping was performed of the magnetic field in each of the horizontal sectors throughout the volume which would be occupied by the tracking detector. The results of this mapping were compared with results from a simple calculation based on the Biot-Savart law as well as a Vector Fields TOSCA simulation. The agreement was reasonable. Discrepancies between the measured and calculated field values could be explained by the uncertainty in the precise conductor positions and by the deflection of the coils under gravity or when energized. The Biot-Savart calculations were redone allowing the coil positions to move radially, along Z, and in azimuthal position to obtain good agreement with the measured values. These calculated values were then used to extend the mapping to regions where it was impossible to make a direct measurement. This extended mapping was used in the reconstruction of events.

Note: for the proposed OLYMPUS measurement precise knowledge of the magnetic field is not necessary as the measurement will be based on ratios of rates as discussed in section 4.3. Nevertheless, the initial alignment of the toroid to minimize the effect on the DORIS beams will be done. Also the field in the tracking volume will be measured at a number of points before the drift chambers are installed and the coil positions measured to provide data for comparison with Biot-Savard calculations which will be used to generate the magnetic field mapping using in tracking and momentum analysis.

3.2 Drift Chambers

The drift chambers shown in Figure 3.8 measured the momenta, charge, scattering angles, and vertices for the particles produced in the reactions studied with BLAST. This was done

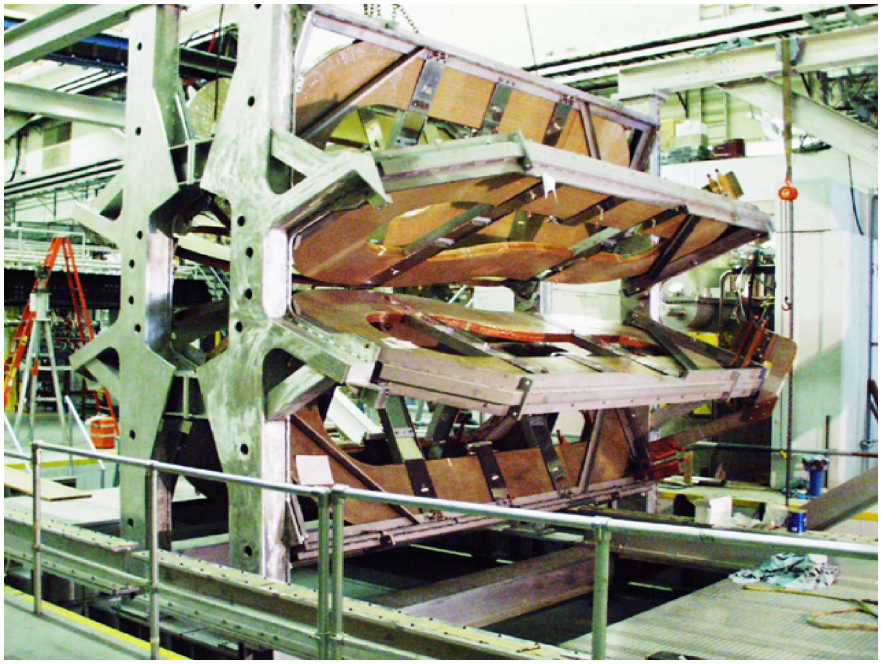

Figure 3.7: The eight coil BLAST toroid without its detectors.

by tracking the charged particles in three dimensions through the toroidal magnetic field and reconstructing the trajectories. Measuring the curvature of the tracks yielded the particles' momenta, and the directions of curvature determined their charge. Tracing the particles' trajectories back to the target region allowed the scattering angles, polar and azimuthal, to be determined and the position of closest approach to the beam axis was taken as the vertex position for the event.

To maximize the active area, the drift chambers were designed to fit between the coils of the toroidal magnet such that the top and bottom plates of the drift chamber frame were in the shadow of the coils as viewed from the target. The drift chambers had a large acceptance and nominally subtended the polar angular range 20°–80° and ±15° in azimuth with respect to the horizontal and were positioned and orientated such that 73.54° with respect to the beam from the target center was perpendicular to the face of the chambers. Because of these choices the chambers were trapezoidal in shape (see Figure 3.9).

Each sector in BLAST contained three drift chambers (inner, middle, and outer) joined together by two interconnecting sections to form a single gas volume (see Figure 3.10). This was done so that only a single entrance and exit window was required for the combined drift chambers thus minimizing energy loss and multiple scattering.

Figure 3.11 shows a cross sectional view of the assembled top plates for the drift chamber. The top plates for the three chambers are shown in brown. The lighter brown illustrates the recesses, from both sides, which were machined in each plate to produce a 7 mm thick plate to accommodate the feed-throughs for the wires which formed the drift chamber cells. The thick portions of each plate were needed to resist the combined wire tensions over the length of the drift chamber. Recall that the top and bottom plates of the frame are in the shadow of the coil as viewed from the interaction area so the thicknesses shown here did

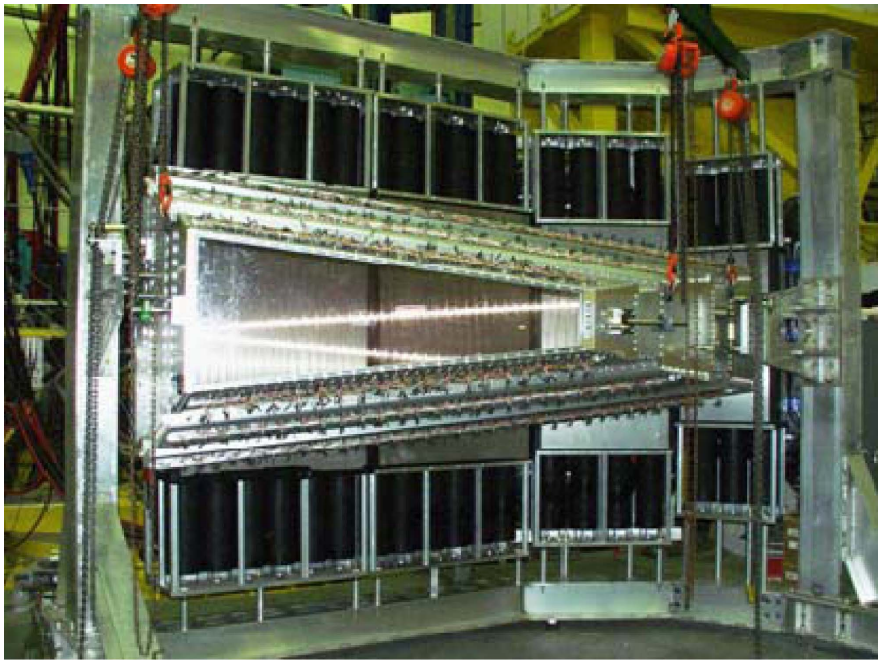

Figure 3.8: Photo of the BLAST drift chambers.

not impact on the detector acceptance. The frame dimensions were adjusted so that each bowed by approximately the same amount (on the order of 1 mm) due to the wire tension. This was necessary to simplify connecting the chambers into a single gas volume. The thin aluminum profile which formed the top plate of the interconnecting section between pairs of chambers is shown in purple and is visible along the bottom edge. The empty region above the interconnecting plate was used to hold the amplifier/discriminator electronics, HV distribution, and for the HV and signal cable runs. The blue line running along the top of the whole assembly represents a $\frac{1}{8}$ inch copper sheet which was used to protect the feed-throughs, wires, and electronics. The bottom plates for the chambers and interconnecting sectors were similar and also had a protective copper plate.

Each chamber consisted of two superlayers (or rows) of drift cells. The drift cells were "jet" style formed by wires. Figure 3.12 shows the wire pattern for a portion of one chamber. The wires in each supperlayer were inclined at $\pm 5^\circ$ to the vertical. This 10° stereo angle allowed reconstruction in three dimensions. Each drift cell had 3 sense wires staggered ± 0.5 mm from the center line of each cell to help resolve the left/right ambiguity in determining position from the drift time. This pattern of wires was realized by stringing wires between the top and bottom plates of each chamber. Holes for each wire were machined in the thin plate of the recessed areas of the top and bottom plates to accept Delrin feed-throughs. The feed-through had a gold plated copper tube insert through which the wire was strung and crimped. The pin provided a convenient connector for the HV.

The three drift chambers for a sector combined into a single unit were then mounted in the sub-detector frame and its position and orientation adjusted until it was in its nominal position. This position was checked by an optical survey and this data was used together with a previous survey and the data from the CMM data on the hole positions to determine

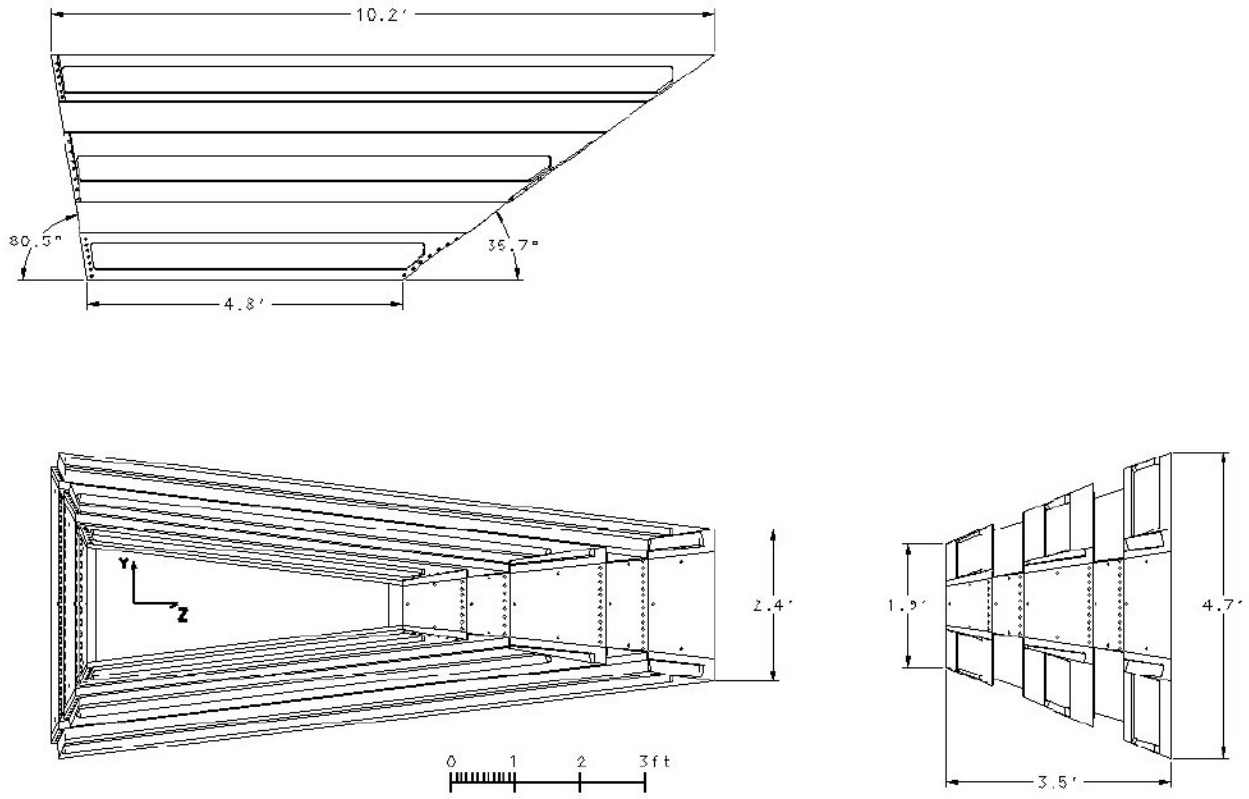

Figure 3.9: Top, bottom, and side views of the assembled drift chamber for a sector giving overall dimensions.

the position of each sense wire in the BLAST coordinate system

With all three drift chambers assembled and positioned in each sector there were 18 planes of sense wires with which to track the charged particles produced at BLAST. In total there was approximately 10,000 wires with 954 sense wires for both sectors in BLAST.

A helium:iso-butane gas mixture (82.3:17.7) was chosen for the drift chambers. The chambers were maintained at a pressure of approximately 1 inch of water above atmospheric pressure with a flow rate of around 3 l/min. The primarily helium mixture has a relatively low density to reduce multiple scattering and energy loss. Also, because the BLAST toroidal field is inhomogeneous over the tracking volume, a small Lorentz angle is desirable so that corrections are small even in regions with high magnetic fields. The helium gas mixture chosen satisfies this as well with $\approx 7^\circ$ Lorentz angle in a 3.8 kG field. Figure 3.13 shows the distinctive lines of electron drift, "jets", for this cell design at 3.8 kG. Using a single gas volume minimizes the number of entrance and exit windows for the same reason. Two layers of 25 micron mylar were used for the entrance and exit windows.

3.3 Tracking Upgrade

Even with 18 planes of sense wires the track reconstruction was not straight forward. This was because the 6 sense wire planes in each of the three chambers in a sector were relatively

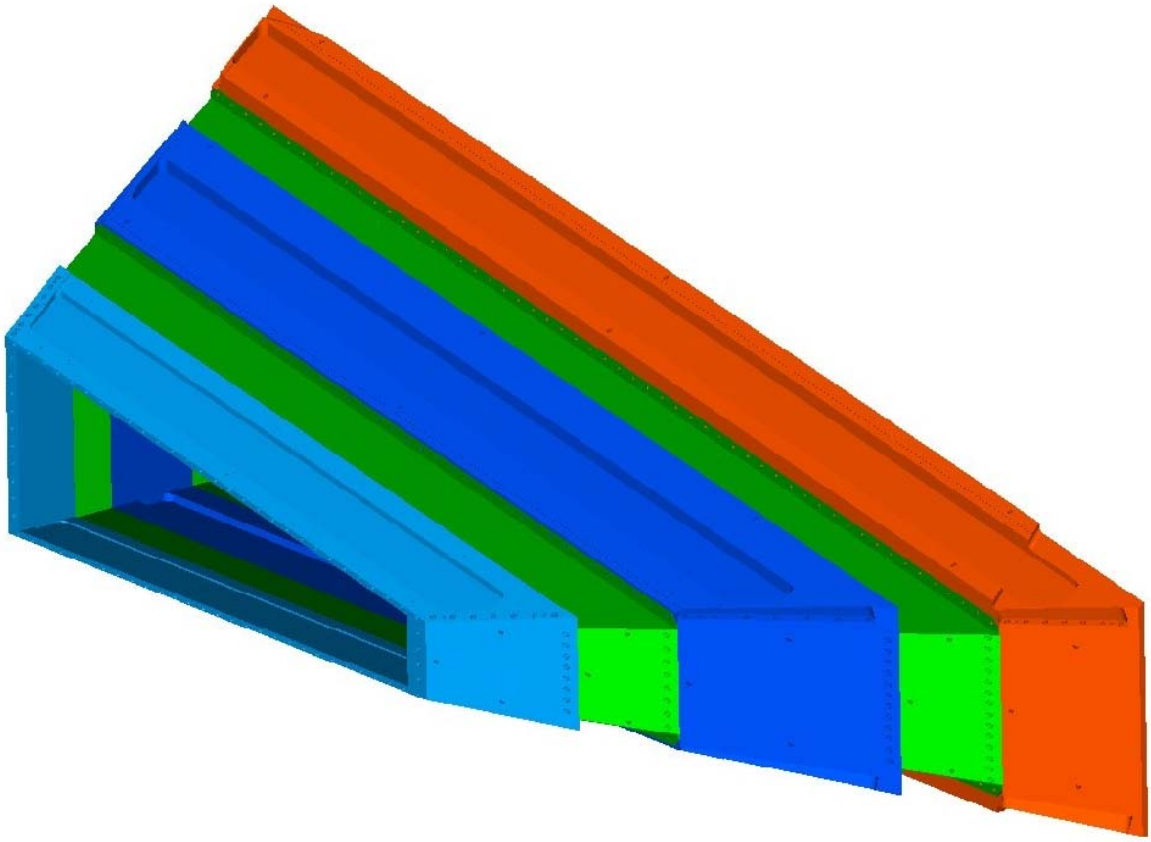

Figure 3.10: Isometric view of all three drift chambers assembled into a single gas volume.

close together and thus tended to yield a single point in space. Thus the track reconstruction had three space points with which to fit the momenta, scattering angles, charge, and vertex. And while this was possible there was no redundancy with which to measure of the accuracy of the reconstruction or to use the data to improve the track fitting parameters. Furthermore, if there was any additional hits in a chamber due to other tracks or noise these extra points could yield tracks that were not easily distinguished from the true tracks. Because of this we would like to add a triple GEM detector approximately 40 cm from the target in both sectors.

This detector would be 90 cm long and trapezoidal in shape varying from 18 to 36 cm in height. The frames of these triple GEM detectors would be in front of the toroid coils so would not reduce the active area. A conservative 2D readout design with 1 mm line pitch should give position resolutions on the order of 150 microns comparable to that of the wire chambers and require less than 1280 channels of readout.

The choice of GEM technology is based on the fact that GEM's are:

- thin - $< 0.7\%$ radiation length
- fast - can handle rates up to 500 kHz/cm^2

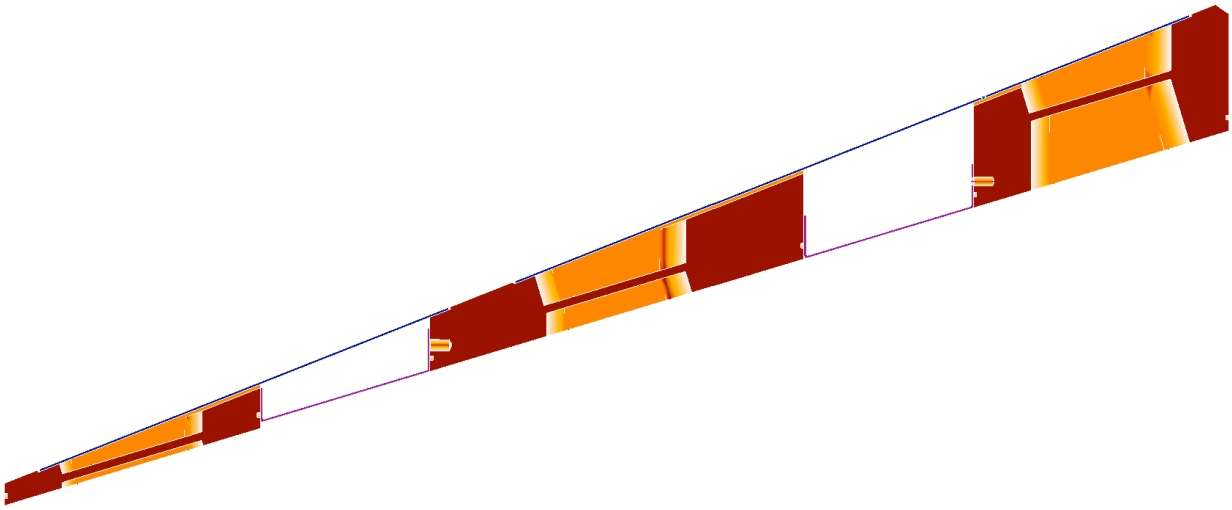

Figure 3.11: Cross sectional view of the top plates of the three drift chambers and interconnecting sections when assembled into a single gas volume.

- 2D - readout can provide both X and Y information
- compact - approximately 10 mm thick
- accurate - resolutions better than 50 microns are possible
- radiation tolerant
- insensitive to magnetic fields

In addition we can benefit from existing programs at MIT which is producing triple GEM detectors for an upgrade to the STAR forward tracking region and at INFN/Rome which is producing 2 triple GEM based trackers for a new spectrometer at JLAB.

Based on the FGT experience in producing the triple GEM detectors the cost for the OLYMPUS tracking upgrade is estimated in Table 3.1.

Also listed in Table 3.1 is a small improvement to the existing wire chamber front end electronics. Specifically we will redesign the high voltage distribution to reduce heating in the region of the wire chamber amplifier/discriminator cards and simplify the access and cabling for the HV system.

GEM Technology

A single Gas-Electron Multiplier (GEM) consists of a thin metal-clad insulation foil perforated by a regular dense hole pattern [54]. The holes in the foils typically have a double conical shape with an inner diameter of $\sim$50 μm, an outer diameter of $\sim$70 μm and a pitch of 140 μm. Figure 3.14 shows an electron microscope picture of a GEM foil and a cross section view of one hole. A voltage difference between the two metal-clad sides of the foils leads to high electric fields in the holes, as illustrated in Figure 3.15. This is used to achieve

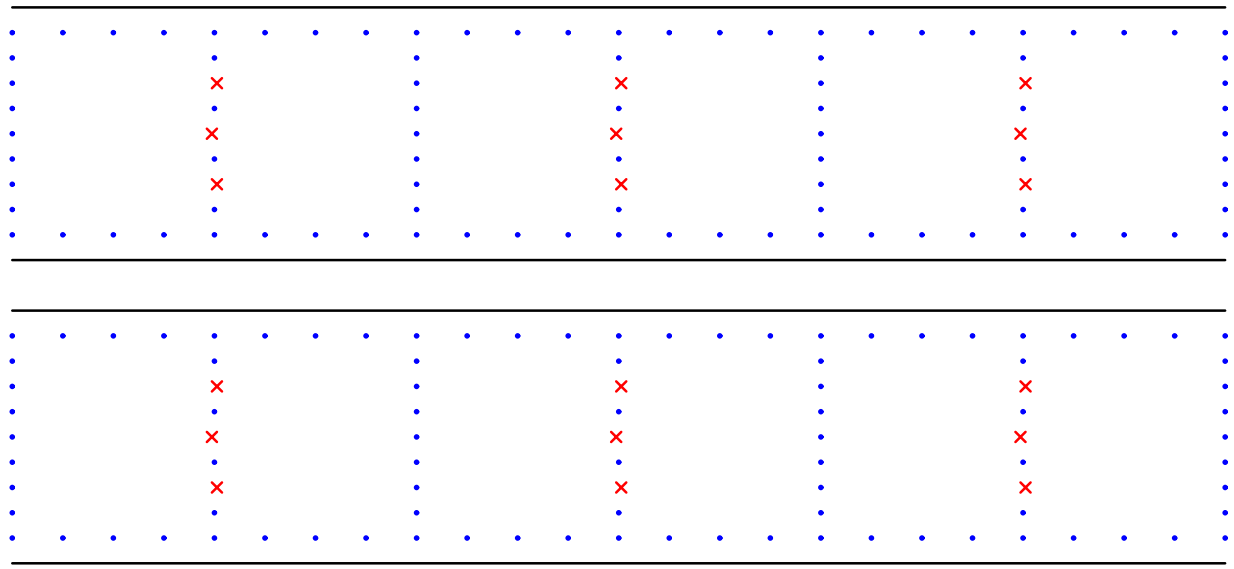

Figure 3.12: Schematic of wire layout in one chamber showing the drift cell pattern for both super-layers.

electron multiplication in the detector gas.

A triple GEM detector configuration is shown in Figure 3.16 A charged particle ionizes the gas in the drift region above the first GEM foil. The applied electric field accelerates the electrons to the GEM foil and a significant fraction ($\sim 60\%$) enter the holes in the GEM foil where, due to the high electric fields, ionize the gas further resulting in a gas gain of ~ 100. This process is repeated with the second and third GEM foils until finally the avalanche of electrons is detected on the readout plane. Gains up to 10^6 have been achieved though typically gains of 6–8 $\times 10^5$ are sufficient for detection with current electronics.

In practice the top GEM foil is operated at higher gain and the last GEM foil at a lower gain to avoid breakdown because of the abundant charge in the region. The readout can be a single layer with pads or strips but a two dimensional readout is also possible by producing lines on both top and bottom surfaces of a thin foil and exposing the bottom lines by carefully removing the insulating material between the lines on the top surface either through etching or laser ablation. Other 2D readout schemes are under investigation.

The Rome group is actively developing GEM tracking for the experimental program at Jefferson Lab. The present design of the APV25 based electronics for the JLab GEM tracker, is a simplified version of the COMPASS layout; it is intended to split the Electronics DAQ System into a front-end card and a collector board.

The Front-End Card hosts the APV25, and is connected to the GEM 2D readout foil by Panasonic YF31 33 channels connectors. During the prototyping phase, several alternatives are considered:

- power on board and external (from connectors);
- analog buffer selectable

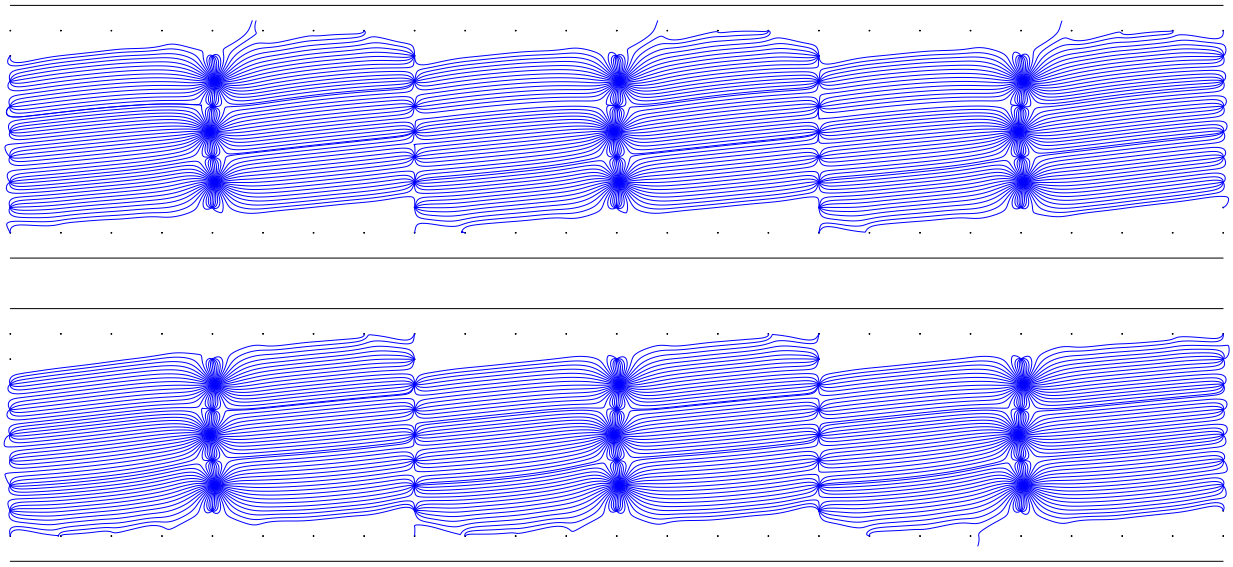

Figure 3.13: Lines of electron drift in the drift cells assuming the maximum BLAST field of 3.8 kG.

- internal or external IREF
- GND from diodes or by a resistance
- I^2C level adapter in case of USB external interface
- 1-wire temperature monitor
- one rotary switch for the I^2C addressing (only 16 chips addressable instead of 32); only even number are selectable in order to get not-delayed output.

The APV25 die will be bonded to the PCB directly, avoiding the ceramic pitch adapter used in COMPASS version. At the moment, a standard flat cable connector with 20 pins

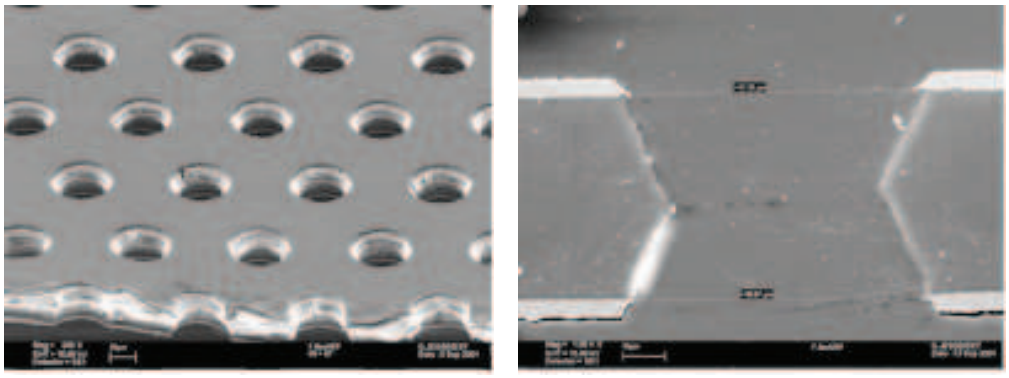

Figure 3.14: Electron microscope picture of a GEM foil and cross section view through one hole. [55].

Item	Base Cost	Quantity	Cost
Triple GEM Detector			
GEM foils	\$350	20	\$7,000
GEM foil NRE	\$3,000	1	\$3,000
2D Readout Layer	\$6,000	2	\$12,000
2D Readout Layer NRE	\$3,000	1	\$3,000
Detector frames and support	\$7,500	1	\$7,500
Gas system	\$3,000	1	\$3,000
Front end electronics	\$1,500	3	\$4,500
Readout system	\$5,000	1	\$5,000
Mechanical engineer	\$20,000	1	\$20,000
Electrical engineer	\$20,000	1	\$20,000
Sub Total			\$85,000
WC FEE Upgrade			
New HV distribution	\$10,000	1	\$10,000
Sub Total			\$10,000
Total			\$95,000

Table 3.1: Wire chamber upgrade costs.

has been adopted with the analog output between the grounded twisted pairs; the signals and voltage levels from/to the front-end are:

- 3 LVDS: trigger (in), clock (in) and analog data (out).
- 2 I2C lines.
- 3 voltage lines, one line maybe optional if the voltage regulator on board can be used.
- 1 temperature monitor line (optional).

In total, a minimum of 12 pins are used. The power supply may be doubled for a total of 15 pins. The optimal size of the front-end card is expected to be smaller than 60×50 mm^2 The collector board is foreseen to be based on VME64x standard. This module hosts the signals transmitters and receivers to/from the APV25 Front-End cards, 40 MHz ADCs (one for each front-end), the control logic, the pedestal compensation and zero suppression logic (using a FPGA). In addition, during the prototyping, the VME64x collector module will possibly host a fast serial link (optical fiber or Copper Wired Ethernet) which will be used for testing purpose and could be important in the case the ADC must be moved close to the front-end cards.

The collector board should be located in a radiation safe area at a distance from the front-end card smaller than 10 m. This will be tested. In case this will be not possible, it is expected to host the ADC on a intermediate module between the Front-End and the VME64x.

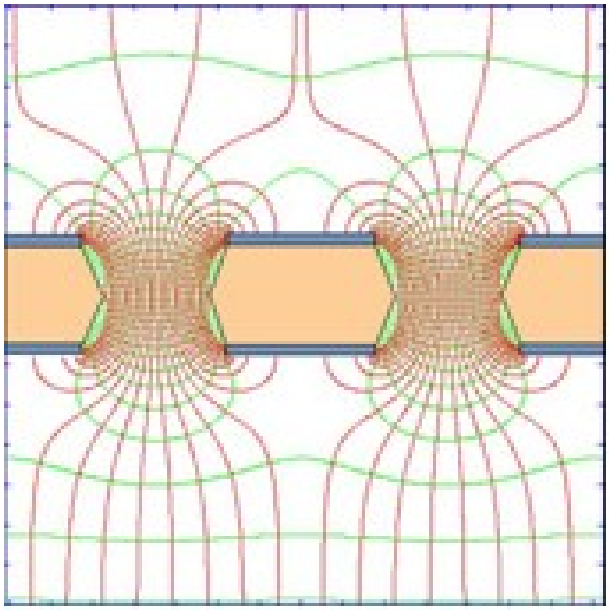

Figure 3.15: Simulated electrical field inside a GEM hole. Electrons released in the upper gas volume drift into the holes, multiply and get transferred to the lower side.

3.4 Time of Flight Scintillators

In each sector of BLAST 16 vertical scintillator bars formed the time of flight (TOF) detector. The TOF detector was designed and produced at the University of New Hampshire to provide a fast, stable timing signal correlated with the time of each event at the target independent of which scintillator bar was struck. This signal was used to trigger the readout and data acquisition system for all other components and particularly provided the COMMON STOP signal for the drift chambers. This permitted relative timings among all components to be measured. The TOF detector also provided a measure of energy deposition to aid particle identification. Approximate position information was also possible from the timing difference between the top and bottom photomultiplier tubes.

In BLAST the TOF detector curved behind (see Figure 3.17) the wire chambers and Čerenkov detectors in each sector roughly matching the angular coverage of the tracking detector in both polar ($\sim 20^\circ < \theta <\sim 80^\circ$) and azimuthal ($\pm \sim 15^\circ$) projections. The forward four bars at $\theta < 40^\circ$ were 119.4 cm high, 15.2 cm wide, and 2.54 cm thick. The remaining 12 bars at $\theta > 40^\circ$ were 180.0 cm high, 26.2 cm wide, and 2.54 cm thick.

Bicron BC-408 plastic scintillator was chosen for its fast response time (0.9 ns rise time) and long attenuation length (210 cm). Each TOF scintillator bar was read out at both ends via Lucite light guides coupled to 3 inch diameter, Electron Tubes[1] model 9822B02 photomultiplier tubes, PMTs, equipped with Electron Tubes EBA-01 bases. The light guides were bent to point away from the interaction region so the PMT's would be roughly perpendicular to the toroidal magnetic field. Mu-metal shielding was used around all PMT's. The bases have actively stabilized voltage dividers so that the timing is independent of the gain.

[1]Ltd, Bury Street, Ruislip, Middlesex, HA4 7TA, England

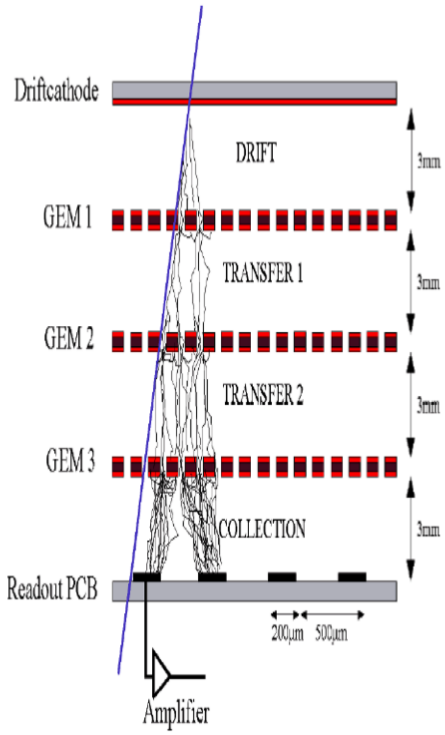

Figure 3.16: Schematic to illustrate the concept for a triple GEM detector.

With readout from both ends of a TOF scintillator bar, the time difference provided coarse position information. To provide a timing signal independent of position along the TOF, the signals from each PMT were split, with one part from each pair of tubes going to a meantimer. This meantime signal was used to provide the event timing signal. Because each TOF was at a different distance from the target center, a delay was added to the closer detectors corresponding to the time for a relativistic particle to travel the difference in distance. These time differences were measured for each sector by inserting a thin plastic scintillator paddle near the target chamber and measuring the TOF detector timing relative to the common start from this paddle. These delayed, meantimed signals were thus correlated with the time of the event at the target. The signals from each PMT were also distributed to TDC's and ADC's.

A 2 mm thick lead foil was placed in front of each TOF bar to attenuate X-rays from the target region. It also prevented back-scattered radiation from firing the Čerenkov detector and being mis-identified as electrons. However, the lead foil was removed from the rear-most four TOF scintillator bars to improve the sensitivity to low energy deuterons.

Gains for the PMT's were set by requiring the ADC signal for minimum ionizing particles from cosmic rays to peak in channel 1250. A time resolution of 320 ± 44 ps was measured for the 32 TOF detectors which was significantly better than the 500 ps required by the experiment. Timing offsets between pairs of scintillator bars were determined using cosmic rays periodically during the experiment. The efficiency was determined to be better than 99%.

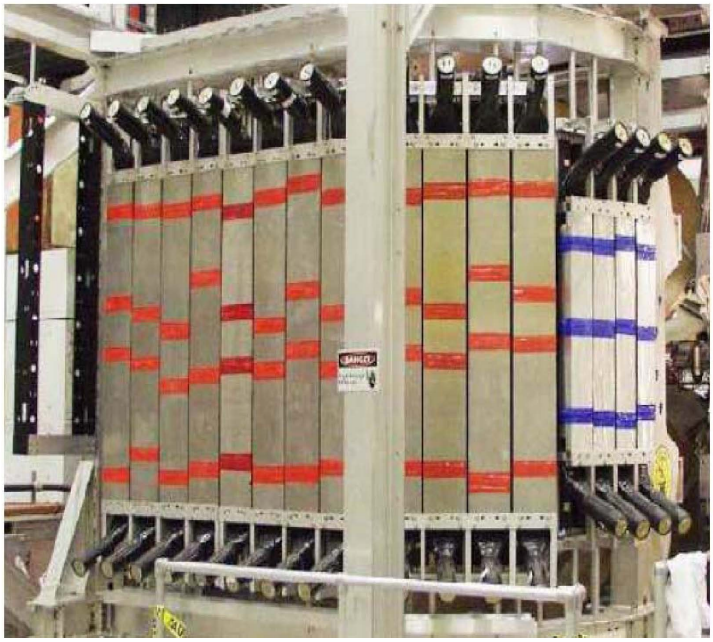

Figure 3.17: TOF detector mounted in sub-detector support during assembly.

Figure 3.18 illustrates the performance of the TOF detector using elastic *ep* scattering. The large figure shows the coincidence between hits in a TOF detector in one sector versus the other. The line of peaks corresponds to elastic scattering kinematics. The empty plots illustrate how rare random coincidences were and how clean event selection was using just TOF timing information. The insets show the timing resolution and coplanarity for *ep* elastic scattering. The TOF timing resolution was typically around 400 ps. The vertical position of the TOF hit could be determined from the time difference between the top and bottom PMTs. Comparing the vertical position of TOF hits in left and right sectors for *ep* elastic scattering and requiring that the event originated in the target yielded a coplanarity better than 2°. Thus TOF timing information was very important in event selection and significantly reduced the background.

3.5 Trigger and Data Acquisition System

3.5.1 Detector Overview

This section gives a short overview for the readout of the detector components of the OLYMPUS experiment. Figure 3.19 shows a typical event. The innermost detector, close to the interaction point, will be the GEM detector (red) followed by the drift chambers (green). Together they provide tracking in the magnetic field of the toroid. The outermost detector components are TOF walls (yellow) composed of plastic scintillators which are read out on both ends by photomultipliers. These will provide the trigger information for the experiment (see below). Also in red is the planned luminosity monitor, a stack of three GEM detectors, mounted along the beampipe in downstream direction. This detector will mainly be used

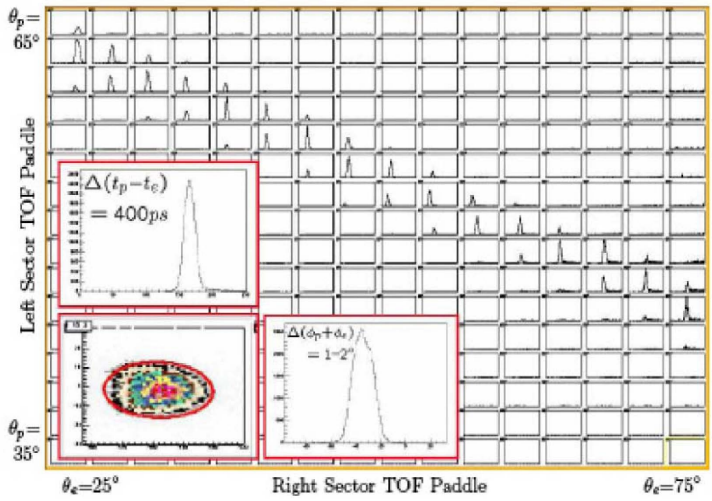

Figure 3.18: TOF timing results using *ep* elastic scattering. The large figure shows the coincidence between TOF counters in left sector versus those in the right sector for events where the trigger was generated by a hit in the right sector. The insets show the timing resolution and coplanarity of elastic *ep* scattering.

for normalization of the taken data, as well as for triggering.

3.5.2 Subdetectors and Readout

The current drift chambers front-end electronics provide one ECL signal per wire, which is read out (after discrimination) by LeCroy LRS1877S Fastbus TDCs to provide time information. The same model is used for the TOF scintillators with the addition of LeCroy LRS1881 ADCs to digitize the summed signal from the PMTs. The readout of the Fastbus systems is realized via Struck 2-Slot VME-Fastbus SFIs which provides VME access to the Fastbus crates. The actual readout is performed by VME-CPUs located in the Struck modules. Additional scaler information is obtained by SIS36xx VME-Scalers hosted in a standard 6U VME crate. The readout electronics is available and can be completely reused. The only new components required are VME-CPUs for the new readout which will be discussed below.

The planned GEM-based detectors will be read out by dedicated APV25 frontend chips. Each APV chip handles 128 GEM channels and transmits data as a serialized stream to dedicated VME-digitizer boards (ELB APV-DIG) which are standard 6U VME units housed in a dedicated crate. Additionally these modules provide an I^2C interface to configure the APV directly. Here the data is again read out out by VME-CPUs.

Additionally various VME-scalers will be implemented to monitor rates in the different detector system.

Table 3.2 gives an overview of the number of digital channels to be read out by the

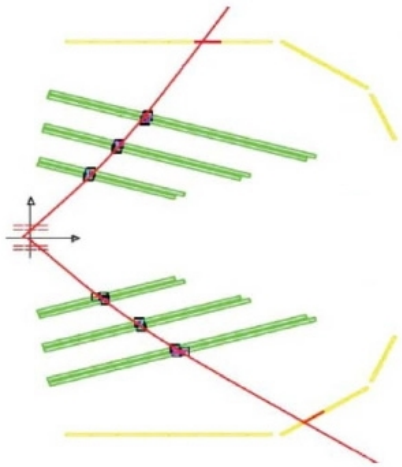

Figure 3.19: A typical $ep \rightarrow ep$ event detected by BLAST.

Subdetector	# of channels	Readoutsystem	Availability
Drift chambers	$\approx 1000 \times 2$	Fastbus	available
ToF scintillators	≈ 200	Fastbus	available
Inner GEM tracker	≈ 800	APV/VME	to be purchased
Luminosity monitor	≈ 1200	APV/VME	to be purchased

Table 3.2: Overview of the Olympus channel count

OLYMPUS data acquisition system. Details on the needed CPUs will be given in the next section.

3.5.3 Data Acquisition

The planned data acquisition system (DAQ) utilizes the DAQ-framework developed for the Crystal Barrel experiment at the ELSA accelerator in Bonn, where it is successfully used for the current measurements.

This framework consists of both a hardware and a software part. It is a synchronous system meaning that each detector is read out at a common *Event* signal, so that the coherence of the taken data is ensured during acquisition. This approach has the drawback of increased complexity compared to to a free-running acquisition system but ensures concurrent data at runtime increasing the reliability of the system since faulty subdetectors will immediately be noticed during data taking.

To achieve synchronous operation a hardware synchronization system, the *Syncsystem*, is implemented. This system works in master/slave mode, which is reflected in its hardware components (see Fig. 3.20). The *Sync-Master* is responsible for generating the *Event* signal

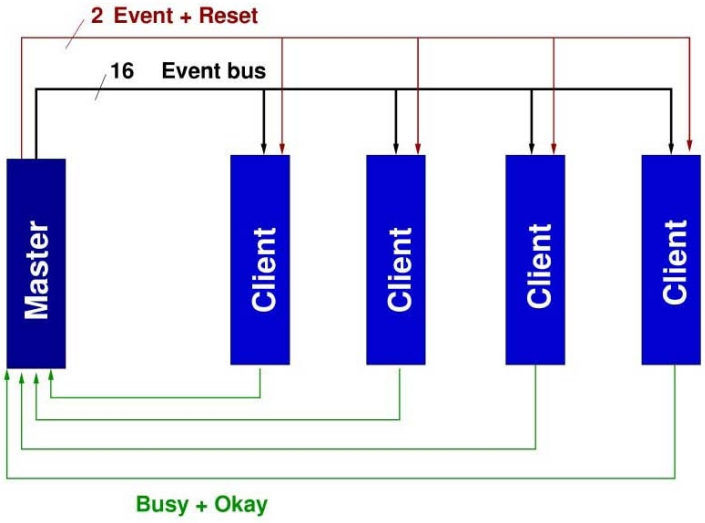

Figure 3.20: Setup for synchronization.

which is then distributed to all clients. This system is implemented as 6U VME-Modules for both the *Sync-Master* as well as the *Sync-Clients*. Each of the modules is matched by a VME-CPU to perform the actual readout. Each *Sync-Client* can signal its state to the *Sync-Master* via its busy/okay lines, so that the master will only generate an event if all clients are in a working state. Figure 3.21 gives a detailed overview of such an synchronous event sequence.

The software side of this DAQ-framework is developed using the Linux operating system on x86-based VME-CPUs. It follows the concept of local eventbuilders (LEVB) for each subdetector (one CPU per subdetector but there can be more if required) and a global event builder which collects the data of each of the subsystems and checks it for completeness before committing the data to disk. For this it uses two dedicated 1 GBit TCP/IP networks, one for control, the other for data transfer, minimizing bandwidth contention. Each LEVB is paired with a *Sync-Client* and interacts with it during readout. It provides all necessary building blocks to implement the sync scheme described above as well as the data transport via TCP/IP to the global event builder. As a consequence only the readout functions for the TDC, ADC, and scaler modules have to implemented, significantly lowering development time and required manpower. The global event builder features a pluggable output system enabling a wide variety of data formats (the current version uses CERN ZEBRA) and can therefore easily be adapted to analysis needs of OLYMPUS. The achievable event rate of this system is about 30 kHz which is well above the limits imposed by the Fastbus modules, which have a maximum of about 1.5 kHz, making it perfectly suitable for OLYMPUS.

This system has proven its reliability at the Crystal Barrel experiment over the last 6 years and is still being actively improved. All hardware used in this system is either developed in Bonn by members of the OLYMPUS collaboration or readily commercially

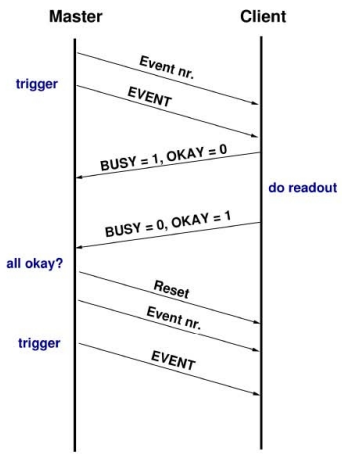

Figure 3.21: Flow chart for synchronization.

available making it future proof for the upcoming experiment. To implement this system a number of purchases have to be made especially for the CPUs and Sync-system. The existing BLAST CPUs cannot be reused since they have a different architecture making it unfeasible to port the software stack described above. Table 3.3 gives an overview of the

#	Component	Cost estimate
6	x86 VME CPU	$\approx 6 \times 3,000$ EUR
7	VME Syncmodules	$\approx 7 \times 2,000$ EUR
2	Storage Server	$\approx 2 \times 2,000$ EUR
1	Database Server	$\approx 1 \times 2,000$ EUR
	Total (excl. taxes)	$\approx 38,000$ EUR

Table 3.3: Required equipment and cost estimate for the DAQ system including spares

required components and a cost estimate.

Graphical user interface

Using this existing system also provides additional benefits like a graphical runcontrol system (see. Fig 3.22) featuring an integrated run database which is accessible via webinterface (see. Fig 3.23). This database tracks all relevant run parameters. Also included is an online shift log which allows to store e.g. comments of the shift crew correlated with the current run.

These components can be adapted to the OLYMPUS setup with minimal effort further lowering the implementation time.

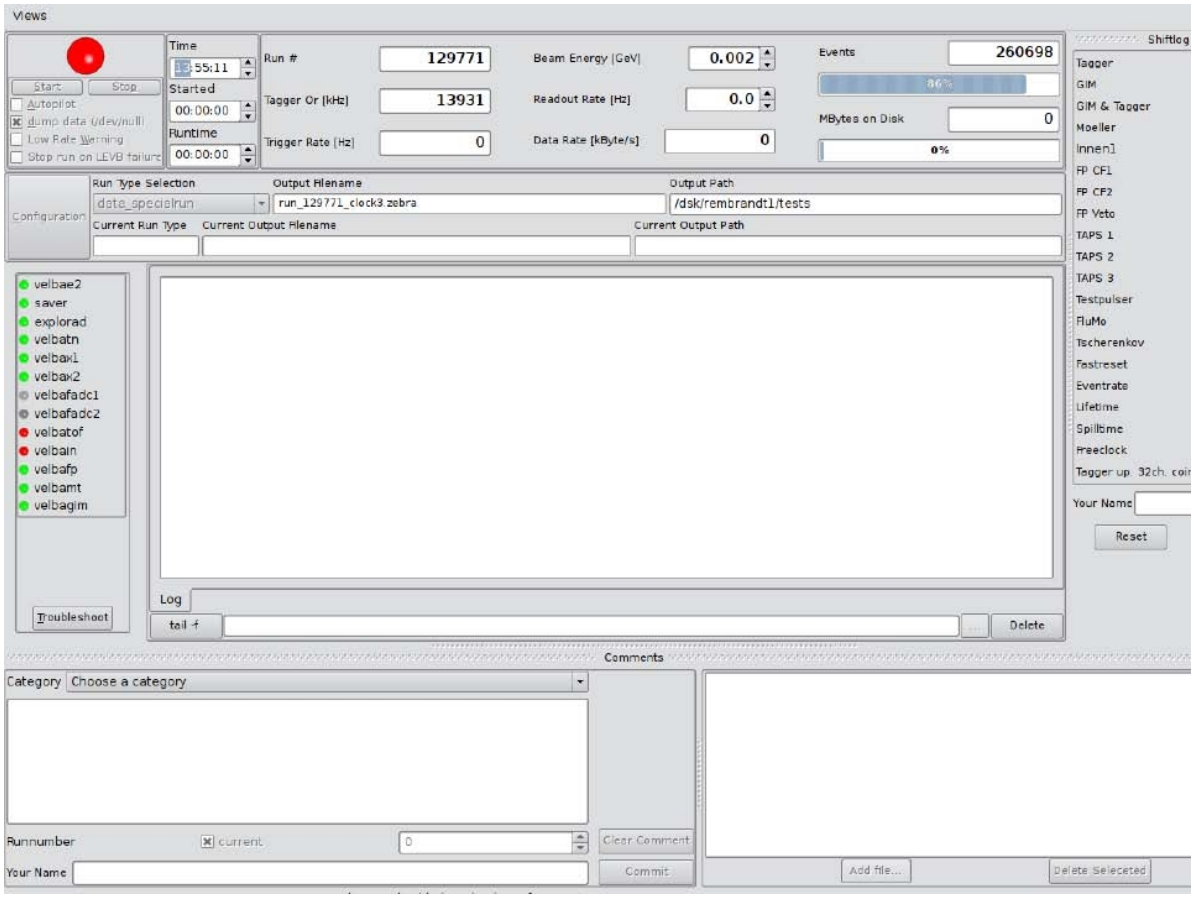

Figure 3.22: Graphical run control system

3.5.4 Trigger System

The trigger system is responsible for selecting relevant events by combining the information of the trigger capable (fast) subdetectors and consequently starting the data acquisition. The OLYMPUS experiment will have two trigger sources available namely the TOF scintillators and the Luminosity Monitor (LuMi). The TOF will be used to detect the elastic $e^{\pm}p \to e^{\pm}p$ events. The typical signature of such an event as shown in Fig. 3.19 is two charged particles, one in each part of the symmetric detector. To achieve sensitivity on this type of events the coincident PM signals for each scintillator bar of one detector side are combined by a lifetime optimized logical OR. These signals are called ToF^L and ToF^R respectively. The luminosity monitor generates a trigger signal out of the triple coincidence of the sum signals of each GEM stack. Analogous to the ToF these signals are called $LuMi^L$ and $LuMi^R$.

These signals can be combined to form the trigger conditions for the actual datataking. The planned conditions are given in Tab. 3.4. Additionally all of these signals will be gated by the DORIS bunch clock to suppress uncorrelated background. All of these trigger conditions can run simultanously (meaning the actual trigger is an logical OR of the given conditions), though the last three triggers will most likely have to be downscaled due to their expected high rates.

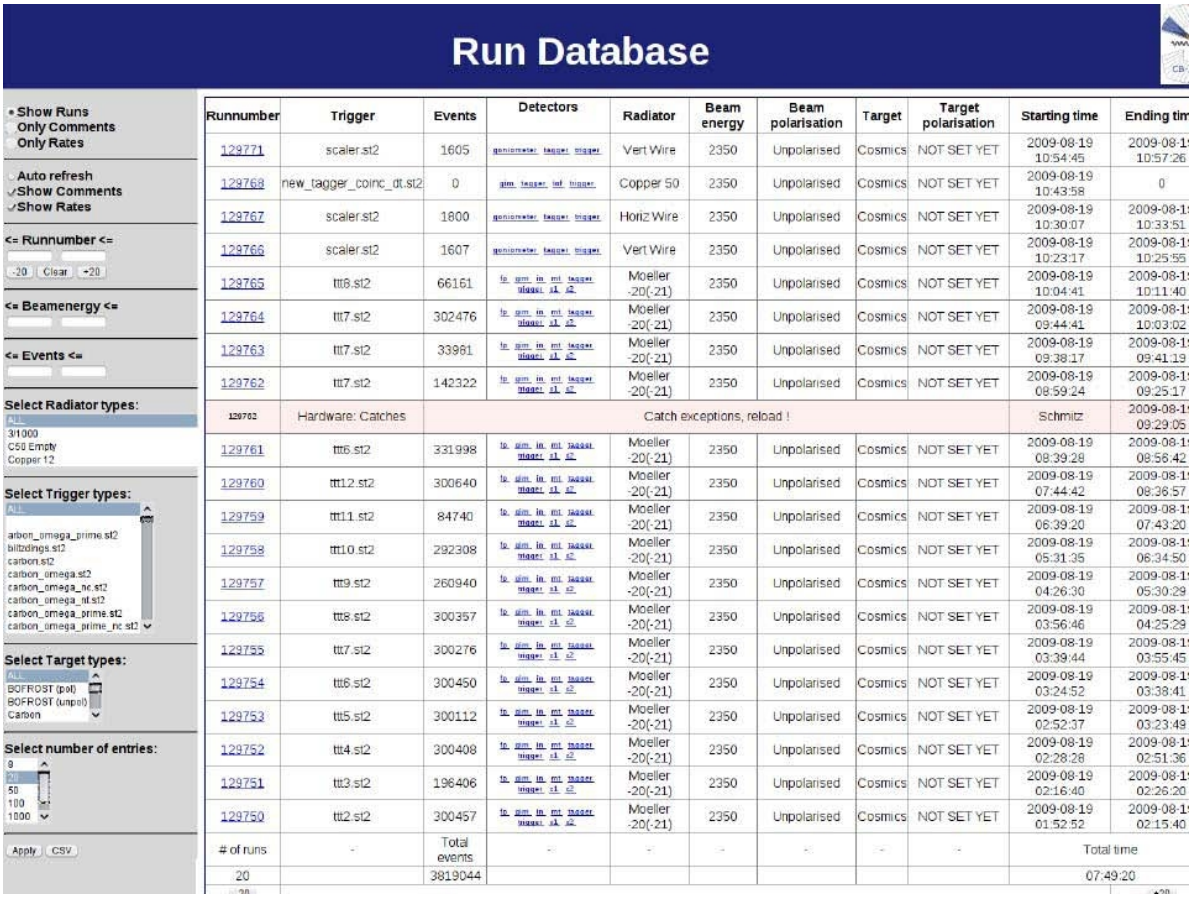

Runnumber	Trigger	Events	Detectors	Radiator	Beam energy	Beam polarisation	Target	Target polarisation	Starting time	Ending tim
129771	scaler.st2	1605	goniometer, tagger, trigger	Vert.Wire	2350	Unpolarised	Cosmics	NOT SET YET	2009-08-19 10:54:45	2009-08-1 10:57:26
129768	new_tagger_coinc_dt.st2	0	gim, tagger, inf, trigger,	Copper 50	2350	Unpolarised	Cosmics	NOT SET YET	2009-08-19 10:43:58	0
129767	scaler.st2	1800	goniometer, tagger, trigger	Horiz.Wire	2350	Unpolarised	Cosmics	NOT SET YET	2009-08-19 10:30:07	2009-08-1 10:33:51
129766	scaler.st2	1607	goniometer, tagger, trigger,	Vert.Wire	2350	Unpolarised	Cosmics	NOT SET YET	2009-08-19 10:23:17	2009-08-1 10:25:55
129765	ttt8.st2	66161	fp, gim, in, mt, tagger, trigger, s1, s2,	Moeller -20(-21)	2350	Unpolarised	Cosmics	NOT SET YET	2009-08-19 10:04:41	2009-08-1 10:11:40
129764	ttt7.st2	302476	fp, gim, in, mt, tagger, trigger, s1, s2,	Moeller -20(-21)	2350	Unpolarised	Cosmics	NOT SET YET	2009-08-19 09:44:41	2009-08-1 10:03:02
129763	ttt7.st2	33981	fp, gim, in, mt, tagger, trigger, s1, s2,	Moeller -20(-21)	2350	Unpolarised	Cosmics	NOT SET YET	2009-08-19 09:38:17	2009-08-1 09:41:19
129762	ttt7.st2	142322	fp, gim, in, mt, tagger, trigger, s1, s2,	Moeller -20(-21)	2350	Unpolarised	Cosmics	NOT SET YET	2009-08-19 08:59:24	2009-08-1 09:25:17
129702	Hardware: Catches	Catch exceptions, reload !							Schmitz	2009-08-1 09:29:05
129761	ttt6.st2	331998	fp, gim, in, mt, tagger, trigger, s1, s2,	Moeller -20(-21)	2350	Unpolarised	Cosmics	NOT SET YET	2009-08-19 08:39:28	2009-08-1 08:56:42
129760	ttt12.st2	300640	fp, gim, in, mt, tagger, trigger, s1, s2,	Moeller -20(-21)	2350	Unpolarised	Cosmics	NOT SET YET	2009-08-19 07:44:42	2009-08-1 08:26:57
129759	ttt11.st2	84740	fp, gim, in, mt, tagger, trigger, s1, s2,	Moeller -20(-21)	2350	Unpolarised	Cosmics	NOT SET YET	2009-08-19 06:39:20	2009-08-1 07:43:20
129758	ttt10.st2	292308	fp, gim, in, mt, tagger, trigger, s1, s2,	Moeller -20(-21)	2350	Unpolarised	Cosmics	NOT SET YET	2009-08-19 05:31:35	2009-08-1 06:34:50
129757	ttt9.st2	260940	fp, gim, in, mt, tagger, trigger, s1, s2,	Moeller -20(-21)	2350	Unpolarised	Cosmics	NOT SET YET	2009-08-19 04:26:30	2009-08-1 05:30:29
129756	ttt8.st2	300357	fp, gim, in, mt, tagger, trigger, s1, s2,	Moeller -20(-21)	2350	Unpolarised	Cosmics	NOT SET YET	2009-08-19 03:56:46	2009-08-1 04:25:29
129755	ttt7.st2	300276	fp, gim, in, mt, tagger, trigger, s1, s2,	Moeller -20(-21)	2350	Unpolarised	Cosmics	NOT SET YET	2009-08-19 03:39:44	2009-08-1 03:55:45
129754	ttt6.st2	300450	fp, gim, in, mt, tagger, trigger, s1, s2,	Moeller -20(-21)	2350	Unpolarised	Cosmics	NOT SET YET	2009-08-19 03:24:52	2009-08-1 03:38:41
129753	ttt5.st2	300112	fp, gim, in, mt, tagger, trigger, s1, s2,	Moeller -20(-21)	2350	Unpolarised	Cosmics	NOT SET YET	2009-08-19 02:52:37	2009-08-1 03:23:49
129752	ttt4.st2	300408	fp, gim, in, mt, tagger, trigger, s1, s2,	Moeller -20(-21)	2350	Unpolarised	Cosmics	NOT SET YET	2009-08-19 02:28:28	2009-08-1 02:51:36
129751	ttt3.st2	196406	fp, gim, in, mt, tagger, trigger, s1, s2,	Moeller -20(-21)	2350	Unpolarised	Cosmics	NOT SET YET	2009-08-19 02:16:40	2009-08-1 02:26:20
129750	ttt2.st2	300457	fp, gim, in, mt, tagger, trigger, s1, s2,	Moeller -20(-21)	2350	Unpolarised	Cosmics	NOT SET YET	2009-08-19 01:52:52	2009-08-1 02:15:40
# of runs	-	Total events	-	-	-	-	-	-	Total time	
20		3819044							07:49:20	

Figure 3.23: Graphical interface to the rundatabase

On the hardware side this multi-coincidence will be implemented in an FPGA based VME module (ELB VME-FPGA). This module provides selectable trigger conditions, meaning that each of the aforementioned conditions can be switched on and off by software, as well as scalers for each trigger signal and the combinations thereof. Again a similar module is already used in the Crystal Barrel Experiment considerably leveraging development time for this component. The generated trigger signal is the fed into the *Syncsystem* described in the previous section, starting the readout process.

3.5.5 Electronics overview

As a summary for this chapter the following figure (Fig. 3.24) gives a complete overview of the proposed system. It features all necessary hardware components as well as the corresponding interconnects, though for readability some simplifications had to be made.

Condition	Sensitivity/Purpose
ToF^L **AND** ToF^R	$e^{\pm}p \rightarrow e^{\pm}p$ trigger
$ToF^{L/R}$ **AND** $LuMi^{R/L}$	Trigger on small angle scattering
$LuMi^L$ **AND** $LuMi^R$	Trigger on forward elastic scattering (normalization)
ToF^L **OR** ToF^R	Debugging trigger
$LuMi^L$ **OR** $LuMi^R$	Debugging trigger

Table 3.4: Planned trigger conditions for OLYMPUS

3.6 Integration and Alignment of the Detector

3.6.1 Toroid Alignment

To align the OLYMPUS toroid, first the upstream and downstream base cross beams must be laid perpendicular to the beam centerline, at a known distance from the OLYMPUS target center. The beams (parallel to the centerline) which join the upstream and downstream base cross beams are then bolted in. The vertical K-beams (two beams at each end) which support the 8 coils are then mounted on the base cross beams. A theodolite on the beam centerline views the two flanges where the K-beam halves join to align the K-beams left/right and adjust the roll. A theodolite whose sightline is perpendicular to the beam centerline, a known distance upstream/downstream from the OLYMPUS target center, is used to set the K-beams the correct distance from the target center, and adjust the yaw and pitch. An optical level or theodolite at beam height is used to set the K-beams at the correct height. The K-beam bases are grouted in place.

The main frame is then assembled, in preparation for coil installation. The coils have survey target bushings epoxied to the coil surface, as well as bushings in the coil carrier. The locations of these bushings have been related to the copper windings and the coil water inlet stub in a separate survey. Ideal locations for these targets have been calculated relative to the beam centerline and the OLYMPUS target center. As each coil is set in the main frame, optical surveying techniques are used to align the coil, placing the survey targets in their ideal locations to better than 1 mm. Pusher screws in blocks on the K-beams are used to adjust the coil position.

3.6.2 Detector Alignment

The detector support frames for each sector ride on rails which mount on the main support frame in well-defined locations. The positions of the TOF scintillators are fixed by the rails and support frame. This is adequate for the TOFs. The critical detector components to align are the wire chambers. These are attached to the detector support frame by an adjustable six-strut system, which allows the wire chambers to be placed in a well-known and desirable position.

There are bushings on each of the 3 wire chambers, on the top, bottom, upstream and downstream sides. The location of these bushings with respect to the individual wire holes were measured by the chamber manufacturer with a Coordinate Measuring Machine, to an accuracy of approximately 0.1 mm. Because the chambers fit tightly into the coils and

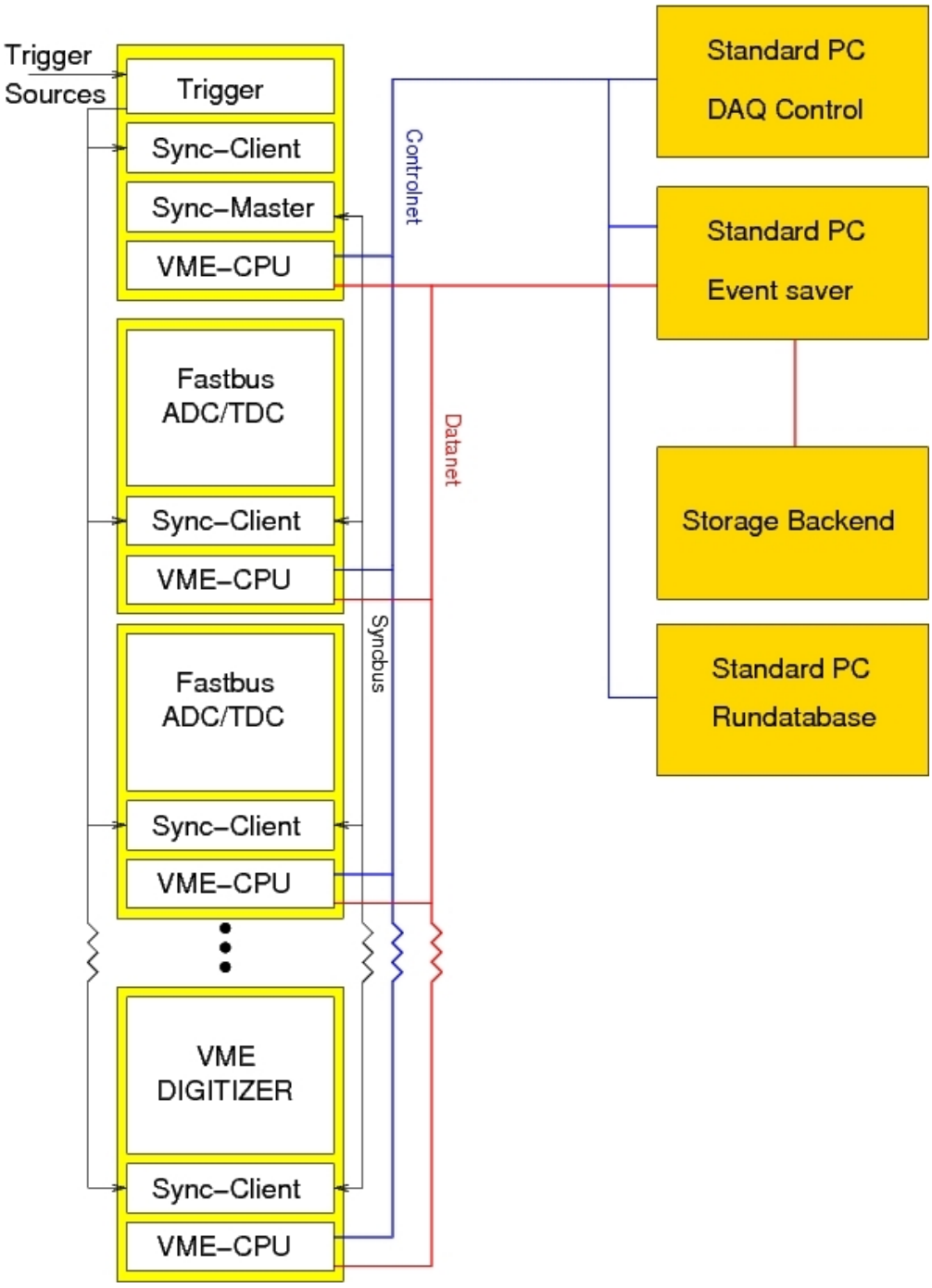

Figure 3.24: Overview of the Trigger/DAQ system

support structure, it is difficult to see many of the survey targets once the detectors are mounted and the support frame is closed. Therefore, after the 3 chambers were assembled into a unit at MIT-Bates, the chambers were mounted in the detector support frame, and adjusted to be in roughly the correct location. An optical survey was done with the detector support frame in the open position to measure the relative locations of the targets on the

3 chambers, as well as targets on the detector support frame, accurate to approximately 0.2 mm. Ideal coordinates for all the targets were then calculated, locating the chambers in the proper location with respect to the beam centerline and target. The targets on the support frame, and a few targets on the upstream and downstream faces of the wire chambers, are then used to survey the actual location of the wire chambers. The actual location is known to approximately 0.5 mm.

For OLYMPUS, it will be necessary to align the base cross beams and the K-beams, and then align each coil individually. Match marks made before disassembly at Bates will allow reassembly at DESY with minimal alignment. The optical survey of the wire chamber assembly in the support frame will have to be done for the two sectors, and then the survey for the actual location.

Chapter 4

The Luminosity Monitor

4.1 Requirements

The primary observable of this experiment is the ratio of differential cross sections for positron-proton and electron-proton elastic scattering. The redundant control measurements of the luminosity will allow the e^+p/e^-p cross section ratio to be determined with high precision. The experiment is based on measuring both the lepton and recoil proton in coincidence.

Measurement of absolute differential cross sections in a counting experiment requires knowledge of the luminosity (i.e. the product of beam current and target density), acceptance (i.e. in case of elastic scattering the accepted solid angle for each considered bin), the deadtime of the data acquisition system, and the local efficiencies to detect the proton and the lepton if they fall both into the acceptance. However, in measurements of differential cross section ratios, as is done with the OLYMPUS experiment, only ratios of the above quantities occur. In the way the OLYMPUS experiment is designed, some of these quantities will cancel out exacly such as the detection efficiencies for the proton and the lepton arm. Others, such as the ratio of luminosities need to be determined with high precision in dedicated efforts.

In addition to varying the beam species between electrons and positrons, OLYMPUS has the possibility to reverse the polarity of the toroidal magnetic field in a highly reproduceable way. As is shown below, this feature allows to cancel out all efficiency terms exactly, subsequently they don't need to be known, but should be as large or as close to 100% as possible for a meaningful experiment. The DAQ deadtime will be measured by counting the periods of ungated and gated clocks depending on the status of the data acquisition. For the cross section ratio, one is therefore still left with the unknown acceptance and luminosity ratios. The former must be precisely determined by a Montecarlo simulation of the acceptance, in order to integrate the accepted solid angle over the detector volume for any considered bin, separately for electron and positron scattering in both configurations for the magnet polarity. The latter unknown quantity, i.e. the ratio of luminosities, is subject to an additional dedicated measurement. Since only ratios occur, monitoring the luminosities relatively with a counting system is sufficient – no absolute calibration will be required.

The luminosity is expected to vary rapidly with time, as the beam current in the storage ring drops according to its lifetime and the ring will be refilled periodically. Measurement

with positron and electron beam happens sequentially, so the two beam currents are completely independent. Positron and electron beams can have different properties due to different interaction with restgas in the ring. Likewise, the target densities can fluctuate and it is possible that they are systematically different for electron and positron beams. Therefore, the ratio of luminosities is neither constrained to be constant nor to be unity. With the goal of 1% systematic uncertainty on the ratio of differential cross sections, the ratio of luminosities needs to be measured to significantly higher precision.

What matters for the experiment, however, is not the instantaneous but the integrated luminosity over periods of time, within which slowly varying parameters such as detection efficiencies are constant within 1%. It is envisioned to switch between positrons and electrons and between the toroidal magnet polarities about once per day. The cross section ratio can be inferred from such a cycle of four states (four combinations of beam species and magnet polarity), in which the efficiencies cancel out exactly. The cycle will be repeated to reduce remaining systematic uncertainties by the square root of the number of cycles.

If the count rate of the luminosity monitor is high enough, one can also look for the evolution of the instantaneous luminosity over short periods of time, although this is not strictly required. In that case, one can verify the constancy of relative efficiencies between the main detector and the luminosity monitor within time intervalls of a single state of the cycle. The main detector count rates normalized to the time-differential luminosity should not vary with time other than statistically. Subsequently, one would like to have a luminosity "monitor" in counting mode that provides better than one percent statistical error in one hour. The typical cycle length is one day per state (beam species and magnet polarity combination).

4.2 Monitoring the Luminosity

There are several ways of monitoring the luminosity:

- Pressure and temperature measurements for monitoring of the target density
- Beam current measurements
- Bremsstrahlung emitted downstream
- Moller and Bhabha scattering
- Forward-angle elastic scattering

The target thickness will be monitored over time by continuously measuring the pressure and temperature of the reservoir and by an additional flow meter to measure the flux from the buffer. From these parameters and the given geometry and measured temperature of the target tube, the target density along the extension of the tube and the resulting target thickness can be inferred based on a simple gas flow model. The stored current of positrons and electrons in the ring will be measured with an absolute precision of 1% with a parametric current transformer as was done for the BLAST experiment at MIT-Bates [1], providing a

precise monitor of the luminosity when combined with the gas flow information from the buffer system.

Besides measuring the target thickness and beam current separately, it is also possible to measure and to monitor the luminosity with counting methods based on well-known processes of beam-target interaction such as bremsstrahlung or elastic scattering from atomic electrons (Moller scattering) or from target protons at forward angles.

For monitoring the luminosity at OLYMPUS, we choose the latter method of forward-angle elastic lepton-proton scattering. Naively, one could think of a single-channel counter near the beam axis, e.g. a scintillator hodoscope, without identifying the process that leads to an event in that counter. Subsequently, such a simple system would be prone to backgrounds not originating from the target but from regions upstream or downstream, from the collimator exit cone, or from the target tube walls. Such backgrounds would be strongly dependent on the beam quality and could systematically depend on the beam species. Similarly, bremsstrahlung radiation detected downstream near zero degrees could originate from any materials in addition to the target gas such as rest gas in the ring. Also this method may depend on the beam species due to the nature of the beam interaction with the restgas.

Therefore, a method is needed which identifies the actual process that is proportional to number of beam and target particles and is independent of the beam species, i.e. electrons or positrons. Only two choices come into question:

- Moller and Bhabha scattering:
  Moller scattering denotes the process of elastic scattering of electrons, Bhabha scattering that of positrons from electrons of the target atoms. This elastic lepton-lepton scattering process is in leading order independent of the beam charge. The kinematics for Moller scattering is focused at very small angles for both the scattered and the recoiling lepton. A Moller measurement would involve a coincidence of two very-small angle lepton detectors, ususally placed symmetrically about the beam axis. The elastic kinematics of the Moller scattering process would be overdetermined with measurement of two lepton tracks, allowing to suppress backgrounds and to cleanly identify the Moller/Bhabha scattering process.

- Elastic e-p scattering:
  At forward angles and given beam energy, the elastic e-p scattering cross section is well known. The virtual photon polarization ϵ is large and close to 1, and the four-momentum transfer is low, $Q^2 < 1$ (GeV/c)^2. In this kinematic region, single-photon exchange is valid, i.e. it describes the elastic cross section to within 1%. Two-photon exchange effects are expected to be negligible, i.e. their effects would be smaller than the design goal for the systematic uncertainty of OLYMPUS. Hence the forward-angle ratio of rates for both e^+p and e^-p elastic scattering presents a precise measurement of the ratios of luminosities.

In order to employ forward-angle elastic e-p scattering for luminosity monitoring, we will use a set of position-sensitive counters at a forward angle of about 12° to detect electrons or positrons in coincidence with the recoiling proton at large angle covered by the acceptance of the OLYMPUS detector in the opposite sector. The forward-angle detector will have to

be radiation-hard, capable of handling high rates in the MHz region and has to provide good angular ($< 0.5^\circ$) and vertex resolution (< 1 cm) for the forward tracks. It was therefore proposed to construct tracking telescopes with three tracking planes at forward angles based on GEM technology. Two telescopes will measure lepton tracks at a forward angle of approx. 12 degrees, one in each of the two horizontal sectors set up symmetrically. Each telescope will consist of three tracking planes, each tracking plane provided by a triple GEM detector.

The telescopes will be used to fully reconstruct the tracks of the lepton, i.e. the polar and azimuthal angles θ and ϕ, and the vertex coordinate along the target extension z, in coincidence with the proton track reconstructed from the wire chamber information of the OLYMPUS main detector. The coincidence requirement between the forward and the main detector, as well as further kinematic correlations between the lepton and proton track, will suppress backgrounds from any source including random coincidences. For a clean event selection of elastic scattering, the polar and azimuthal angles of the lepton track will be correlated with those of the recoiling proton and with the proton's measured momentum. Additional event selection redundancy is achieved by correlating the recorded times of the lepton and proton events and by correlating the reconstructed vertices of both the lepton and proton track.

At forward angles, the field integral of the OLYMPUS toroid is quite small, resulting in almost straight tracks for elastically scattered electrons or positrons. Nevertheless, the curvature of the track will be observed and used to reconstruct the track parameters at the target by using three tracking planes. As in the case of the wire chamber analysis of the main detector, a "swimming technique" will be used in the analysis to determine the trajectory through the toroidal magnetic field map. For the assumed elastic process, the momentum of the lepton required for the swimming procedure can be inferred from the obtained results of the proton track.

The angular resolution of the track should be better than 0.5°, which corresponds to a spatial resolution requirement at the location of the detector of about 2 cm. If the target was pointlike, this modest requirement could already be achieved with several crossed layers of thin scintillator hodoscopes. However, the OLYMPUS target tube has a length of 60 cm. The resolution of the reconstructed vertex needs to be better than 1 cm in order to match the vertex resolution for the proton track obtained from the wire chamber information. Such a vertex resolution can only be achieved with spatial resolutions of the telescope planes of order 0.1 mm. Therefore, the conceptual design of the forward telescope calls for a package of three planar triple-GEM detectors, similar to the COMPASS-GEM [56] and the MIT prototype [57], allowing the lepton tracks to be measured with high resolution. The distances between the three tracking planes and intrinsic resolution can be optimized for a suitable vertex resolution. Detailed Montecarlo simulations are underway for the best choice of intrinsic resolutions and positions of the tracking planes to optimize the vertex resolution while maintaining a large enough solid angle for a given active area of the telescope.

In the current design, the three tracking planes will be located at distances of 187, 227, and 287 cm from the target, respectively, centered at 12° facing the target for perpendicular impact angle. The positions of the three planes approximately correspond to the positions of the wire chamber planes whose acceptance starts adjacent to the telescope at about 22°.

For beam energies between 2.0 and 4.5 GeV, the four-momentum transfer at $\theta_e = 12^\circ$ varies between 0.17 and 0.80 $(\mathrm{GeV/c})^2$, and the virtual photon polarization parameter ϵ is

E_0 [GeV]	Q^2 [(GeV/c)^2]	$p_{e'}$ [GeV/c]	ϵ	θ_p	p_p [MeV/c]	Rate [h^{-1}]
4.5	0.801	4.073	0.9736	58.7°	992	1846
2.0	0.167	1.911	0.9774	71.8°	418	49792

Table 4.1: Kinematics and count rates of the luminosity control measurement for beam energies of 2.0 and 4.5 GeV at $\theta_e = 12°$. The assumed solid angle is 1.2 msr determined by the area of rearmost tracking plane farthest from the target.

above 0.97. Here the single photon approximation is good to better than 1%. The proton is recoiling with momenta of 400-900 MeV/c at angles of 59°–72°, well within the rear-angle acceptance of the OLYMPUS detector. The tracking telescopes will not require any collimation to define the solid angle; instead, all tracks will be reconstructed and the solid angle be defined by software cuts.

The cross section at low Q^2 and $\epsilon > 0.97$ is large enough to provide $< 1\%$ statistical error for the above configuration in less than 15 minutes for 2.0 GeV beam energy, indicating the suitability of this setup as a luminosity monitor. The expected count rate for this luminosity monitor is listed for two beam energies of 2.0 and 4.5 GeV in Table 4.1.

4.3 Control of Systematics

The primary observable of this experiment is the ratio of the electron-proton and positron-proton elastic cross sections. The redundant control measurements of the luminosity will allow the e^+p/e^-p cross section ratio to be determined with high precision.

As shown below, the individual proton and lepton detection efficiencies and the systematic errors associated with them will cancel to first order. However, acceptance effects need to be taken into account. In the OLYMPUS proposal [2], the effects on the cross section ratio due to slightly different acceptances for coincident detection of leptons and protons in the four beam species/magnet polarity combinations had been neglected. Below is laid out a scheme, how such acceptance effects can be accounted for explicitly.

The differential number of counts dN between times t and $t + dt$ and in the detector volume element $d^n x$, using generalized detector coordinates x_k, is a function of efficiencies for proton and lepton detection, luminosity, differential cross section and acceptance and is given by

$$dN = \kappa^p(t)\kappa^l(t)\dot{L}(t)dt \, \frac{d\sigma}{d\Omega}(\theta_e)a(x_k)d^n x, \tag{4.1}$$

where κ^p and κ^l denote the proton and lepton detection efficiencies, which could generally vary with time, and $\dot{L}(t)$ is the instantaneous luminosity. The elastic differential cross section is denoted by $d\sigma/d\Omega$ and is only a function of one variable, e.g. the lepton scattering angle. The acceptance function $a(x_k)$ depends on all detector-related coordinates x_k, which can be lepton and proton angles and momenta, or reconstructed vertices, etc., i.e. all degrees of freedom of a coincident lepton-proton event. For any given event, $a(x_k)$ describes whether or not it would be accepted by the detector, i.e. the acceptance function's value is either 0

or 1. It is the task of a Montecarlo simulation to determine the bin-averaged acceptance or phasespace integral.

To obtain the number of counts, Equation (4.1) needs to be integrated over the time $\Delta T = \int dt$ during which the data acquisition is alive, and over the detector volume $\Delta V = \int d^n x$. The elastic cross section $d\sigma/d\Omega$ is differential only in terms of the solid angle of the lepton. For integration over the detector volume, the acceptance function $a(x_k)$ describes the phasespace covered by the detection volume. As such the acceptance function also accounts for any kinematic correlations that are typical for elastic scattering events. Not the acceptance function itself, but only its integral over the detection volume (phasespace integral) is of interest for the analysis. The integration is carried out numerically by means of a Montecarlo simulation. Note that in addition to acceptance, the detection efficiencies are in the following accounted for explicitly.

Subsequently, the bin-averaged differential cross section equates to

$$\left\langle \frac{d\sigma}{d\Omega} \right\rangle = \frac{N}{\int_{\Delta T} \kappa^p(t)\kappa^l(t)\dot{L}(t)dt \int_{\Delta V} a(x_k)d^n x} \ . \tag{4.2}$$

In the denominator of Eq. (4.2) the bin-averaged differential cross section involves the integral of the acceptance function over the detector volume, which is commonly known as the phasespace integral

$$A = \Delta\Omega = \int_{\Delta V} a(x_k)d^n x. \tag{4.3}$$

For elastic scattering, the acceptance is identical with the solid angle $\Delta\Omega$ accepted in the considered bin.

If the period ΔT is short compared to the time scale within which the efficiencies vary, they can be considered constant in the integral of Eq. (4.2), and the time integral in the denominator results in the product of the time-averaged detection efficiencies $\kappa^p \cdot \kappa^l$ and the integrated luminosity

$$L = \int_{\Delta T} \dot{L}(t)dt \tag{4.4}$$

over the measured period ΔT.

In order to reduce the systematic errors of the cross section ratio due to uncertainties in relative luminosity, acceptance and efficiency with individual electron and positron beams, we require that the beam in DORIS be alternated between electrons and positrons, and that the OLYMPUS magnet polarity be reversed with the same frequency.

For a given bin, the number of events is hence given by

$$N_{ij} = L_{ij}\sigma_i\kappa^p_{ij}\kappa^l_{ij}A_{ij} \ , \tag{4.5}$$

where $i = e^+(e^-)$ for positrons (electrons) and $j = +(-)$ for positive (negative) OLYMPUS magnetic field polarity. The integrated luminosity L is defined in Eq. (4.4), the bin-averaged lepton-nucleon elastic cross section is abbreviated as $\sigma = \langle d\sigma/d\Omega \rangle$, the average efficiencies during the measurement period ΔT are κ^p for detecting the recoil protons and κ^l for the scattered leptons. The acceptance or phasespace integral is given by A as defined in Eq. (4.3).

With a given polarity of the OLYMPUS magnetic field, the efficiency for detecting the recoil protons in the same kinematics will be identical for both electron and positron scattering, namely: $\kappa^p_{e^+ +} = \kappa^p_{e^- +}$ and $\kappa^p_{e^+ -} = \kappa^p_{e^- -}$. Hence, for a given field polarity, j, the proton efficiencies κ^p_{ij} cancel in the ratio

$$\frac{N_{\mathrm{e}^+ j}/L_{\mathrm{e}^+ j}}{N_{\mathrm{e}^- j}/L_{\mathrm{e}^- j}} = \frac{\sigma_{\mathrm{e}^+}}{\sigma_{\mathrm{e}^-}} \cdot \frac{\kappa^l_{\mathrm{e}^+ j}}{\kappa^l_{\mathrm{e}^- j}} \cdot \frac{A_{\mathrm{e}^+ j}}{A_{\mathrm{e}^- j}} \,. \tag{4.6}$$

However, the efficiencies for detecting the scattered electron or positron may differ for a given OLYMPUS magnet polarity but will be the same for opposite polarities, namely: $\kappa^l_{e^+ +} = \kappa^l_{e^- -}$ and $\kappa^l_{e^+ -} = \kappa^l_{e^- +}$. By taking the product of the above ratio for opposite magnetic field polarities yields

$$\frac{\sigma_{\mathrm{e}^+}}{\sigma_{\mathrm{e}^-}} = \left[\frac{N_{\mathrm{e}^+ +}\, N_{\mathrm{e}^+ -}}{N_{\mathrm{e}^- +}\, N_{\mathrm{e}^- -}} \Big/ \left(\frac{L_{\mathrm{e}^+ +}\, L_{\mathrm{e}^+ -}}{L_{\mathrm{e}^- +}\, L_{\mathrm{e}^- -}} \cdot \frac{A_{\mathrm{e}^+ +}\, A_{\mathrm{e}^+ -}}{A_{\mathrm{e}^- +}\, A_{\mathrm{e}^- -}} \right) \right]^{\frac{1}{2}} \,, \tag{4.7}$$

which measures the cross section ratio directly, where all lepton and proton efficiencies cancel out if they do not change during the length of the cycle of four combined states and if the reversal of the magnet polarity exactly reproduces the field amplitude. Equation (4.7) also contains the super ratio of the four phasespace integrals A_{ij}, which has to be determined with Montecarlo simulations. In the central parts of the acceptance it is expected that the phasespace super ratio is close to unity. As Eq. (4.7) indicates, the relative luminosities in the form of ratios need to be known precisely for an accurate determination of the cross section ratio $\sigma_{\mathrm{e}^+}/\sigma_{\mathrm{e}^-}$. Only the combination of count rate super ratios, luminosity super ratios, and super ratio of phasespace integrals yields the final result. In the analysis of OLYMPUS each of the three super ratios in Eq. (4.7) will be determined individually, thereby "blinding" the result for the final cross section ratio until finally put together.

A similar consideration as in Eq. (4.5) also holds for the measurement and combination of the four luminosities, L_{ij}, where the respective efficiencies cancel. In order to measure the relative luminosity, we propose to use elastic scattering at forward angle corresponding to small Q^2 and large ϵ where the effects of two-photon exchange are negligible. Subsequently, the cross section ratio $\sigma_{\mathrm{e}^+}/\sigma_{\mathrm{e}^-}$ becomes unity, and hence the forward-angle coincident elastic rates N^{fwd}_{ij} are directly proportional to the luminosities in each of the four states {ij}

$$\frac{N^{fwd}_{\mathrm{e}^+ +}}{N^{fwd}_{\mathrm{e}^- +}} \cdot \frac{N^{fwd}_{\mathrm{e}^+ -}}{N^{fwd}_{\mathrm{e}^- -}} \;=\; \frac{L_{\mathrm{e}^+ +}\, L_{\mathrm{e}^+ -}}{L_{\mathrm{e}^- +}\, L_{\mathrm{e}^- -}} \cdot \frac{A^{fwd}_{\mathrm{e}^+ +}\, A^{fwd}_{\mathrm{e}^+ -}}{A^{fwd}_{\mathrm{e}^- +}\, A^{fwd}_{\mathrm{e}^- -}} \,, \tag{4.8}$$

which involves another super ratio of acceptances or phasespace integrals A^{fwd}_{ij} to be determined with Montecarlo simulations, now for the combination of the forward lepton detector in coincidence with proton in the OLYMPUS main detector. However, any dependence on the detection efficiencies for the forward lepton and recoil proton cancels out again. The final expression for the measured differential cross section ratio becomes

$$\frac{\sigma_{\mathrm{e}^+}}{\sigma_{\mathrm{e}^-}} \;=\; \left[\left(\frac{N_{\mathrm{e}^+ +}\, N_{\mathrm{e}^+ -}}{N_{\mathrm{e}^- +}\, N_{\mathrm{e}^- -}} \Big/ \frac{A_{\mathrm{e}^+ +}\, A_{\mathrm{e}^+ -}}{A_{\mathrm{e}^- +}\, A_{\mathrm{e}^- -}} \right) \Big/ \left(\frac{N^{fwd}_{\mathrm{e}^+ +}\, N^{fwd}_{\mathrm{e}^+ -}}{N^{fwd}_{\mathrm{e}^- +}\, N^{fwd}_{\mathrm{e}^- -}} \Big/ \frac{A^{fwd}_{\mathrm{e}^+ +}\, A^{fwd}_{\mathrm{e}^+ -}}{A^{fwd}_{\mathrm{e}^- +}\, A^{fwd}_{\mathrm{e}^- -}} \right) \right]^{\frac{1}{2}} \,. \tag{4.9}$$

The ratio of relative luminosities in Eq. (4.8) can be measured at sub-percent statistical errors in less than one hour. Thus, frequent and random filling with both e^+ and e^- beams and reversal of the OLYMPUS field direction will minimize systematic uncertainties in the ratio from acceptance and efficiency differences as statistics are accumulated. The period for alternating beams and magnet polarities has to be short compared to the time over which effects due to detector performance, such as detection efficiencies, are likely to change. Within that time frame, target density and beam current fluctuations, however, are appropriately accounted for and will have no systematic effect. Some period on the order of one day would likely be sufficient. The systematic error of each super ratio measurement according to Eq. (4.9) can thus be reduced by the square root of the number of cycles through the four states $\{ij\}$.

Note the above derivation applies to the lepton detected in one sector of the OLYMPUS detector and the proton detected in the opposite sector. During the experiment, data will be collected simultaneously for leptons and protons detected in both sectors yielding another level of redundancy and cancellation of systematic effects.

The above scheme makes use of measurements of the proton and lepton tracks in coincidence. Further information and additional checks of systematics will be obtained from proton or lepton single-arm events for which the high and low ϵ limits of the OLYMPUS acceptance are extended. Provided that backgrounds in single-arm elastic events can be kept at a minimum, proton single-arm ratios for electron and positron beams with the same polarity of OLYMPUS, as well as lepton single-arm ratios with reversed field polarity also probe the e^+/e^- cross section ratio independently.

4.4 Luminosity Monitor System

The proposed solution for the forward detector will be a package of three planar triple-GEM detectors with 2D strip readout built as a tracking telescope, similar to the MIT prototype, allowing the lepton tracks to be measured with high angular and spatial resolution. Two such telescopes will be used symmetrically centered about 12° left and right of the beam axis. Figure 4.1 shows the MIT prototype prepared for a test experiment at Fermilab [57]. The GEM foils used for this prototype were produced by TechEtch, Inc, a US domestic company in Plymouth, Massachusetts. TechEtch, Inc, can now routinely supply GEM foils with high quality. The required parts for the GEM telescopes can readily be purchased and need to be assembled and tested. The three triple-GEM detectors in each sector for the luminosity monitor and the possible GEM upgrade for the wire chambers can share a common gas system. For the BLAST wire chambers, a helium-isobutane gas mixture was chosen to minimize multiple scattering. However, at the energies proposed for operating OLYMPUS at DORIS this is not necessary and a non-flammable gas mixture like argon:carbon dioxide can be used.

In the current design, the three tracking planes will be located at distances of 187, 227, and 287 cm from the target, respectively, centered at 12° facing the target for perpendicular impact angle. Each telescope will cover a solid angle of 1.2 msr, determined by the active area of 10×10 cm^2 and the distance of the farthest element of the telescope from the target. Adopting the readout pattern of the MIT prototype [57] with strips along the x and

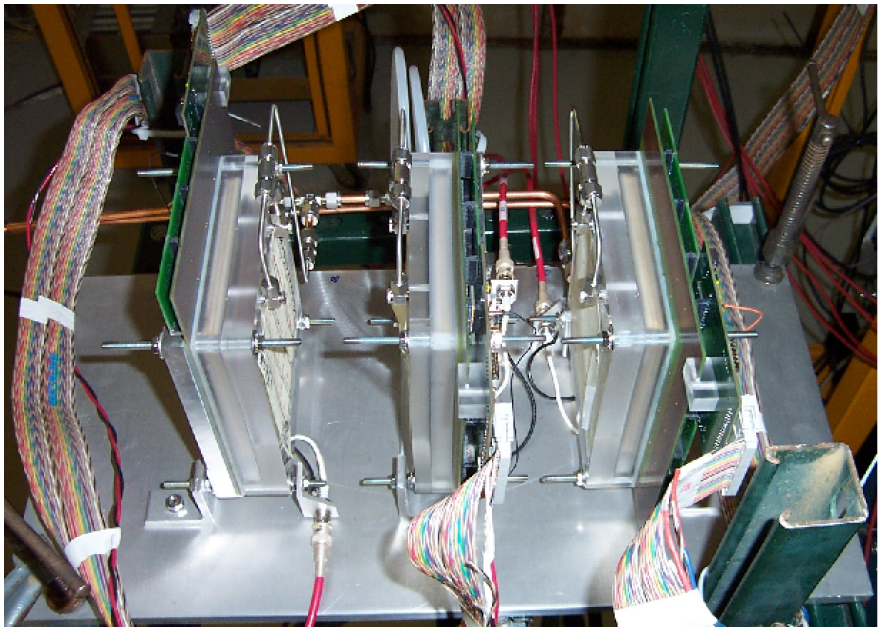

Figure 4.1: Triple-GEM tracking telescope for the test beam experiment at Fermilab.

y directions and a pitch of 635 μm, each plane will consist of $\approx 2 \times 160$ strips in x and y, a total of 3×320 channels per telescope. The MIT prototype telescope [57] has a proven resolution around 70 μm.

For the front-end electronics, the APV-25 chip will be used which can process up to 128 channels, however only 64 channels were used in the prototype (chosen to simplify manufacturing). The three tracking planes per telescope will require 2×3 APV chips per tracking plane or 18 APV chips per telescope. The APV chips are hosted on a hybrid board which, combined with the GEM control unit, is used to digitize the charge information and provide a buffered readout using FPGA technology.

Using the existing design for GEM detectors already developed at MIT including readout and control electronics greatly facilitates the production of the luminosity monitors. It also has the advantage that production costs are lower and implementation of a working design would be simpler. Figure 4.2 shows an example of a system developed at MIT with a GEM control unit providing an FPGA based readout of the APV frontend chip and offering an interface to PCI and/or USB to connect a computer running Labview software for readout. It is envisioned to acquire such a simple system for testing purpose of the individual GEM detector, and of the final telescopes. Upon implementation of the telescopes in the final OLYMPUS setup, the readout of the luminosity monitors will be integrated in the overall trigger and data acquisition system of OLYMPUS.

4.5 Work Plan and Costs

A work plan and timeline for the construction and commissioning activities of the GEM based luminosity monitors at Hampton University and at DESY is shown in Table 4.2. While assembly and testing with cosmic rays and a radioactive source will be a summer

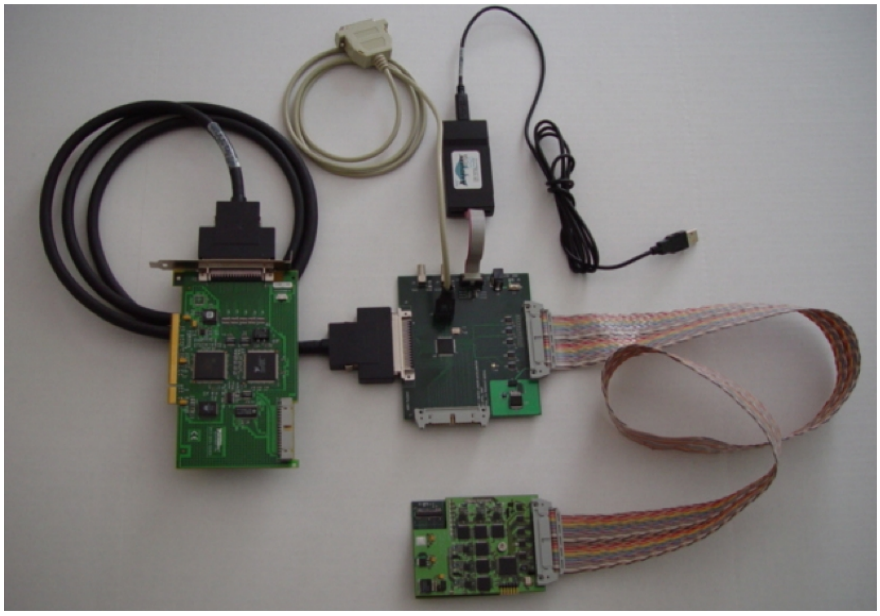

Figure 4.2: Readout and interface boards between APV board and computer.

project at Hampton University involving two undergraduate and one graduate student and one postdoc, the testing of the telescopes with beam will be done in fall 2010 at the Hampton University Proton Therapy Institute (HUPTI), a new cancer treatment facility at Hampton University, which starts operation in summer 2010. Alternatively, the telescopes can be tested at Jefferson Lab in a parasitic setting in Hall C during the scheduled running period of the Qweak experiment.

The cost of the GEM telescopes has been estimated with $125,000 and has been broken down in Table 4.3. Funding for construction and commissioning of the device has been requested from the US National Science Foundation (NSF) within the MRI-R^2 program (Major Research Instrumentation) under the American Recovery and Reinvestment Act of 2009 (ARRA). The luminosity monitor system will be constructed at Hampton University under the direction of M. Kohl.

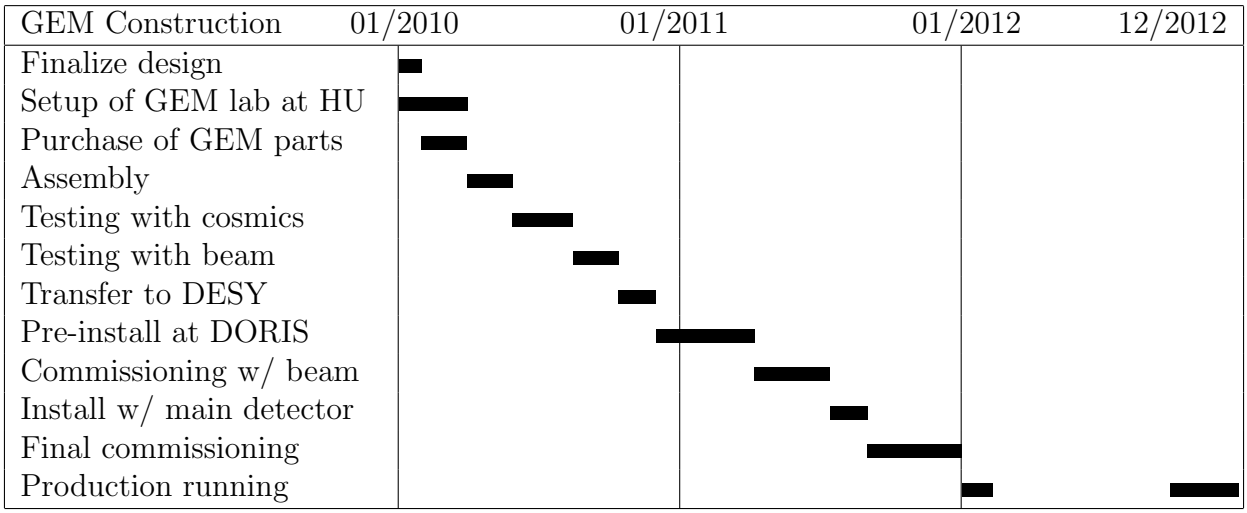

Table 4.2: Work plan for GEM luminosity monitor construction activities.

Item	Amount	Cont.(%)	Total/k$	Remarks
Support frame	3	20	1.8	$500/frame (2+1 spare)
GEM chamber mechanics	9	20	10.8	$1000/chamber (6+3)
GEM foils 10×10 cm^2	40	20	9.6	$200/GEM foil (27+13)
Readout layer	9	20	21.6	$2000/board (6+3)
Hybrids	80	20	19.2	$200/hybrid (54+26)
APV25 chips	80	20	2.4	$25/chip (54+26)
Cables	18	20	2.2	Signal and HV (6+3)
FEE	2880	20	34.6	$10/channel (6+3)x320
Readout system	1		5.0	
HV distribution	9	20	0.5	$50/chamber
Power Supply		20	5.0	HV pods
Gas system	9	20	3.2	$300/line (6+3)
Misc. items			9.1	
Total			125.0	

Table 4.3: Cost estimate for the OLYMPUS luminosity monitors based on two plus one spare forward-angle GEM telescopes, each based on three triple-GEM detectors.

Chapter 5

The OLYMPUS Internal Gas Target

5.1 OLYMPUS target specifications

The OLYMPUS internal hydrogen gas target will be of the type used in the HERMES [58] and BLAST [59] experiments. It will consist of a thin-walled (100 μm) aluminum storage cell with tubes of cylindrical cross section for the circulating DORIS beam, fed by an unpolarized gas feed system. The optics of the stored beam in DORIS determine the transverse dimensions of the cross section of the storage cell to be 9 mm vertically and 27 mm horizontally. The hydrogen gas diffuses slowly out of the cell and is pumped away by a large system of vacuum pumps at each end of the target. The cell wall will be cryogenically cooled to 25 K to increase the thickness of the target. The target will have a thickness of 3×10^{15} atoms cm $^{-2}$.

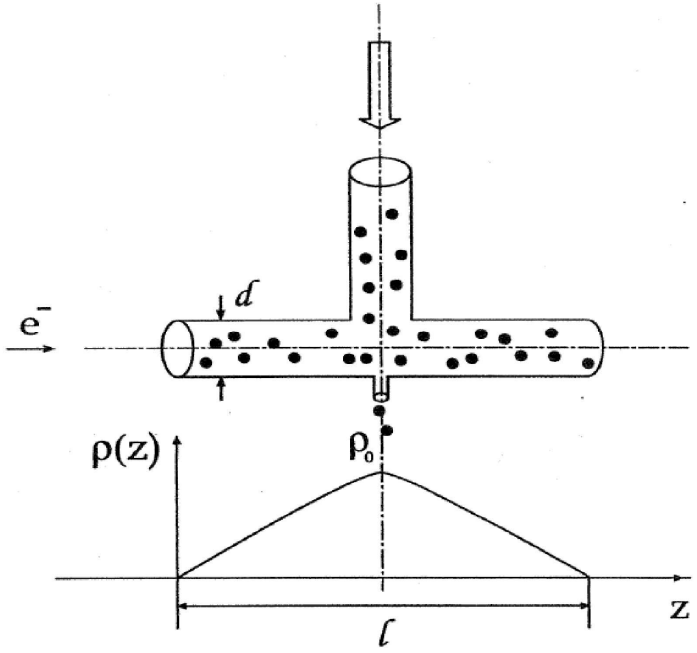

Figure 5.1: The principle of the internal gas target. The density profile along the target cell is approximately triangular.

The hydrogen gas will be fed to the storage cell using a system of valves and mass flow controllers. The feed system is shown schematically in figure 5.2.

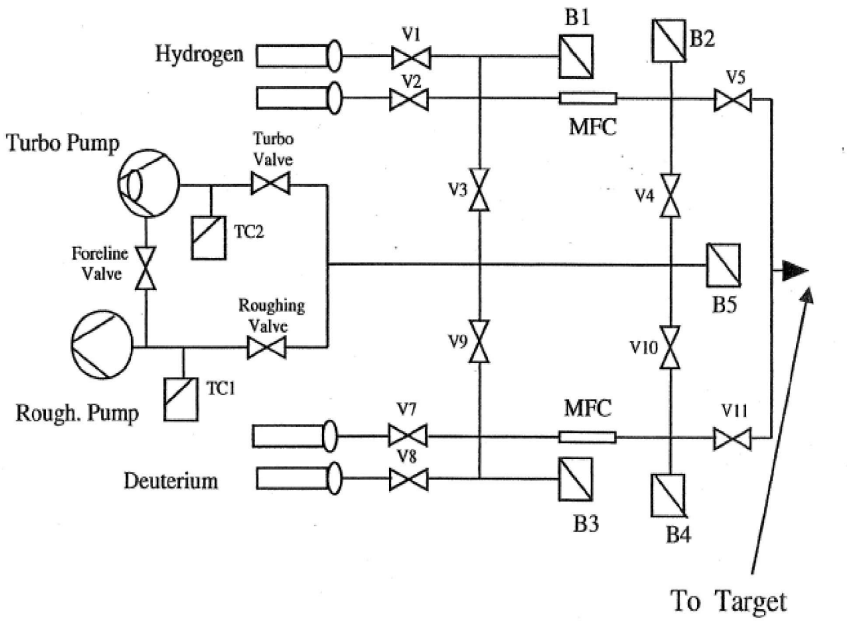

Figure 5.2: Schematic of the BLAST unpolarized gas feed system which can low both hydrogen and deuterium gas. MFC denotes a mass flow controller.

5.2 Target chamber

A new target chamber will be constructed for the OLYMPUS target. This is motivated by the desire to detect forward elastically scattered electrons in the luminosity monitor. Thus, the forward section of the target chamber will be tapered to allow the OLYMPUS detector to accept electrons (or positrons) scattered forward to 10° at the center of the target. Fig. 5.3 shows a schematic layout of the OLYMPUS target chamber. The chamber is 1.5 meters in length and will be machined from a single block of aluminum. The aluminum will be coated with titanium nitride and aluminum flanges will be directly adaptable to stainless steel flanges using copper gaskets. A chamber of this type [60] was built at MIT-Bates and operated for the polarized ^{3}He internal gas target used by experiment CE-25 at the IUCF Cooler, Bloomington, Indiana in the early 1990's.

Fig. 5.3 also shows the fixed collimator in front of the target cell. The collimator will be elliptical with dimensions of 7 mm vertically X 25 mm horizontally. The transverse dimensions of the fixed collimator are chosen to be slightly smaller than those of the storage cell to minimize scattering into the detector. The beam scrapers will be adjusted after injection to minimize halo scattering near the experiment. The target will include wakefield suppressors to minimize heating due to wakefields created by the circulating pulsed beam.

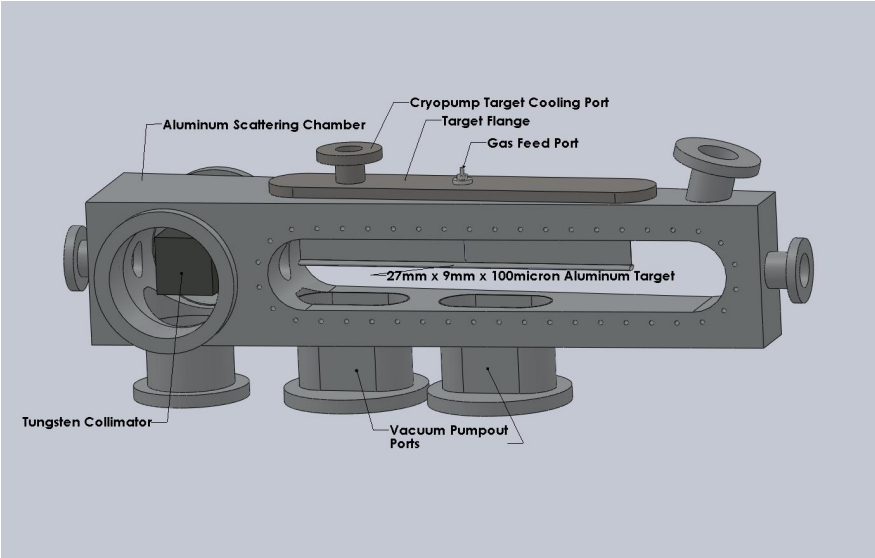

Figure 5.3: Schematic layout of the OLYMPUS scattering chamber showing the fixed collimator and target cell.

5.3 Vacuum system

In BLAST, a large three-stage turbomolecular vacuum pumping system on each side of the target was installed to reduce the vacuum pressure in the beamline. The pumps are Osaka TG 1100M turbomolecular pumps were routinely operated in BLAST from 2002 through 2005 and are maintained at MIT-Bates. Figs 5.4 and 5.5 show this vacuum system in the OLYMPUS experiment. A flow rate of 1.5×10^{17} H_2 per second is required to produce a target thickness of 3×10^{15} hydrogen cm^{-2}. A vacuum calculation has been carried out for this configuration. The central density in the target cell is $\rho_0 = 10^{14}$cm^{-3} and the pressure after the first pumping stage is estimated at 7×10^{-6} torr. The pressure after the third stage is estimated at 5×10^{-8} torr. The addition of a fourth pumping stage to reduce the pressure downstream of the experiment by about another order of magnitude is under consideration. If necessary, this can be implemented straightforwardly.

5.4 Work Plan and Costs

The OLYMPUS internal hydrogen gas target is being designed and constructed by the Erlangen, Ferrara, and MIT groups in close collaboration with the DESY/DORIS machine group. It is being coordinated by the Bates R&E Center staff under the direction of R. Milner and will utilize many of the elements of the BLAST and HERMES internal targets. Existing equipment from the BLAST target with a replacement cost of more than $420k will be used. The Ferrara group is responsible for the target cell design and construction.

The costs required to realize the OLYMPUS target are summarized in Table 5.1.

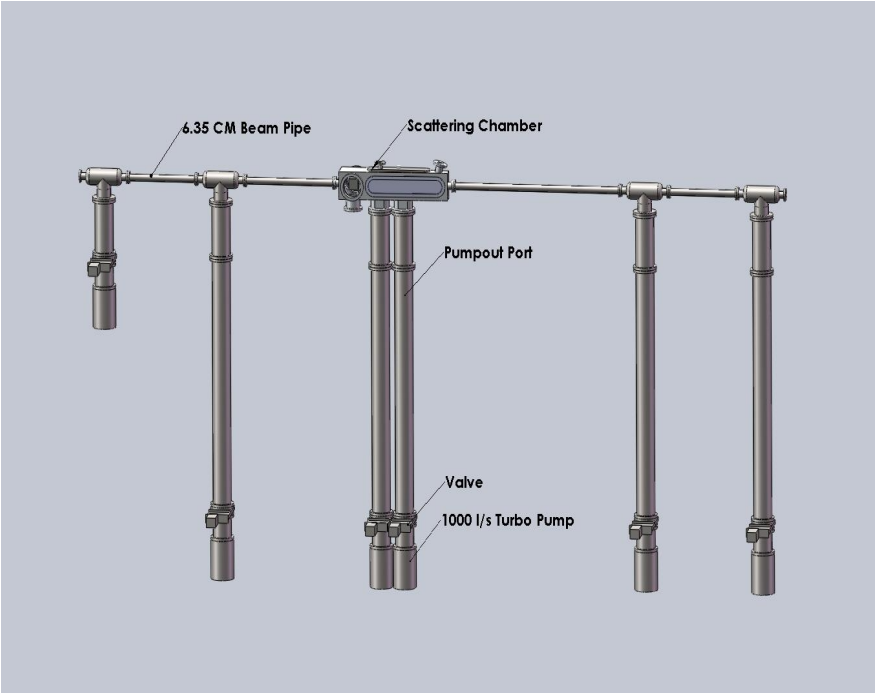

Figure 5.4: Schematic overview of the OLYMPUS target vacuum system.

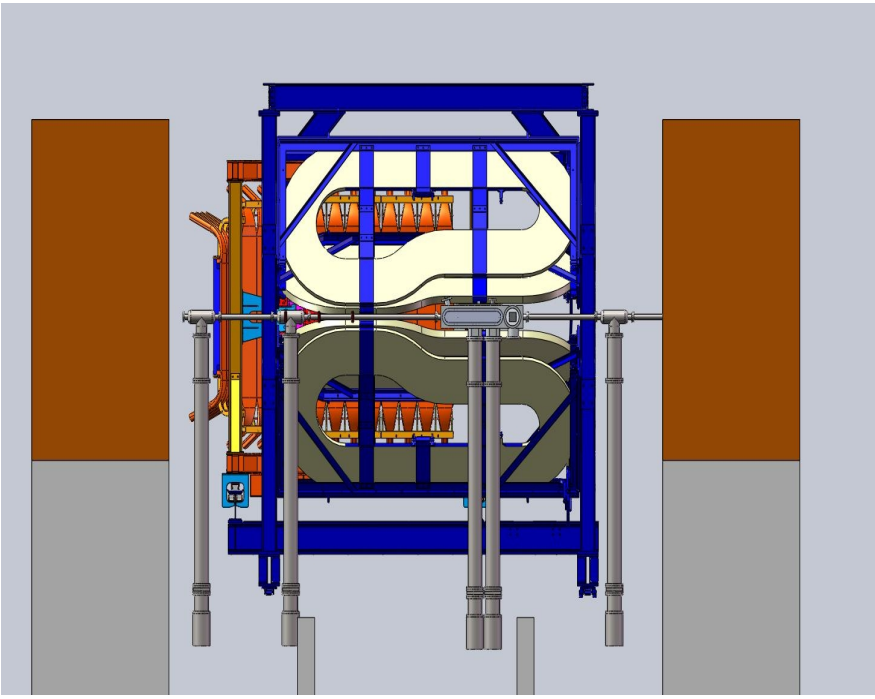

Figure 5.5: Schematic side view of the OLYMPUS target vacuum system.

	k$
gas feed system	30
target cell cooling	30
target chamber	50
wakefield suppressors	10
fixed collimator	8
control system	20
vacuum pumping	75
support structure	50
manpower	227
Total	**500**

Table 5.1: Summary table of funds required to realize the OLYMPUS target

Chapter 6

Installation and Operation

In this chapter the following aspects are discussed: the transportation from MIT-Bates to DESY, Hamburg of the BLAST spectrometer, the detectors, and target; the installation of the experiment; the commissioning of the experiment, and the operation of the experiment.

6.1 Shipping the BLAST Detector and Target to DESY

BLAST consists of 8 coils (plus one spare), a support frame, several types of detectors, and an internal target system. BLAST will be disassembled at Bates, packaged, loaded into appropriate containers and shipped to the DORIS ring at DESY. The re-assembly at DESY will also require supervisory assistance from Bates staff. Due to the complexity and delicacy of the equipment we will require an engineer/supervisor, several technicians and a physicist from the Bates staff to do this work. We will also require an outside company to perform the packaging and container loading. The equipment will be shipped by two methods. The Drift Chambers are wire chambers that are extremely delicate and so they will require shipment by air freight with special packaging. The support structures, magnetic coils, time of flight detectors, and the internal target are more robust and can be packaged and shipped in regular containers by ocean freight. To provide realistic estimates of the shipping costs the MIT-Bates engineering staff worked with the packaging and shipping company Wetmore[1].

6.1.1 Wire Chambers

The wire chambers were not initially designed to be shipped a significant distance. They were wired on the MIT campus as individual chambers and then carefully transported by truck to MIT-Bates ($\approx$ 25 miles) where the three chambers in a sector were assembled together. It is desirable to ship them as they are assembled now but there is a risk of breaking a significant number of the wires. A small number of wires can be replaced easily at DESY. However, if a large number of wires break then the pre-stressing in the frames may cause all the wires to break which would be much more difficult to repair.

To address these concerns initial studies for a support frame have been made. The support frame would consist of a strong bottom frame and individual frames for each of the

[1]Wetmore Company, Inc. 326 Ballardvale St. Wilmington, MA 01887

three chambers. Finite element calculations are being made to evaluate the range of motion which the chambers might experience during shipping. The bottom frame supports all the chambers and allows them to be handled as a whole. The frames for the individual chambers are mounted to the end flanges of each chamber which are quite rigid. Between these, two box beams run along the length of the each wire chamber. Shock absorbers connect to these box beams and limit the motion of the plates to which the wires are attached, thus protecting the wires from excursions beyond their elastic limit.

Two such systems are required: one for each assembled drift chamber. Each would be mounted through the bottom frame to a shock absorbing and damping system and the entire assembly enclosed inside a crate. The crates would be shipped via air freight to minimize shocks. Filtered inlet/outlets will allow the inside of the drift chambers to equalize any pressure changes without allowing dust into the chambers.

The cost for shipping the two assembled wire chambers by air freight was discussed with the company Wetmore and is estimated to be $48k.

6.1.2 BLAST Toroid Magnet and Support Frame

The BLAST toroid magnet and the support frame for the magnet and detector systems are quite robust and do not need overly special handling. Some care in packing is required to avoid stacking heavy items on elements which could be bent or damaged. Also the various parts should not shift or bump together during transport. This can be accomplished with standard shipping containers and wooden framing between the various items within each container.

To estimate the number of containers required and the layout of each item within each container the CAD drawing of the BLAST detector was “dis-assembled” and reorganized as it would be in standard shipping containers. It was decided that the safest and most space efficient way to pack the coils for the toroid would be to leave them in their holding frames and to build “T-frames” to hold them on edge inside the container.

A total of six (6) standard shipping containers will be needed for the BLAST toroid magnet, the support frames, other detector components (next section), and miscellaneous hardware. The cost for shipping to DESY is estimated at $34k.

6.1.3 Time of Flight and Other Detector Systems

The time of flight, TOF, and other OLYMPUS detector components are not so delicate that extra-ordinary steps are required in shipping them to DESY. Photomultiplier tubes will be dismounted from the light guides and packed in molded foam forms in cardboard boxes. Similarly the bases will be packed in cardboard boxes filled with Styrofoam “popcorn”. The scintillator bars and light guides will be packed in thick foam in wooden boxes.

Similar packing consideration will be made for the luminosity monitors, GEM detectors, target system, and other small, light components for which boxes of foam provide adequate shock protection. All these detector components will be included in the contents of one of the standard shipping containers described in the previous section.

6.1.4 Manpower and Professional Services

The main cost for shipping the OLYMPUS detector will be the engineering and technical manpower required to disassemble, pack, and reassemble. It is planned that DESY staff will come to Bates, be closely involved in the disassembly and packing, and will play the main role in the reassembly at DESY but some engineering and physicist involvement from MIT-Bates will be required for the reassembly and realignment of the toroid magnet and wire chambers. The effort required from Bates R&E Center manpower is estimated at approximately nine months total for two engineers and six months for a post-doc, and three months each for six technicians at MIT-Bates for a total cost of $478k.

The professional services of Wetmore Company for packing, consulting, and handling the shipping is estimated at $51k.

6.1.5 Cost

The costs for shipping as described above are detailed in Table 6.1

Item	Base Cost	Quantity	FoS*	Cost
Ocean Freight				
40′ container	$3,985	6	1.2	$28,700
Drop and pickup	$750	6	1.2	$5,400
Ocean Freight Total				$34,100
Air Freight				
Shipping cost (per kg)	$1.20	10,000	1.2	$14,400
Fuel Surcharge cost (per kg)	$1.05	10,000	3.0	$31,500
Security (per kg)	$0.15	10,000	1.2	$1,800
Air Freight Total				$47,700
Services				
Engineers	$263,470	0.75	1.0	$197,600
Post-doc	$121,800	0.5	1.0	$60,900
Travel	$15,000		1.0	$15,000
Technicians	$146,470	1.5	1.0	$219,700
Wetmore Company	$46,400	1.0	1.1	$51,000
Service Total				$544,200
Total				$626,000

Table 6.1: Costs for dis-assembly at MIT-Bates, packing, shipping, and reassembly and alignment at DESY. * 'FoS' denotes 'Factor of Safety'.

6.2 Installation

The installation of the OLYMPUS experiment has been planned to occur in several stages. The BLAST spectrometer and detectors and the internal gas target will be shipped to DESY in 2010. The OLYMPUS spectrometer will be assembled in the park position by September

2010 and the gas target will be installed in the modified DORIS ring by early March 2011. In summer 2011, the assembled detector will be moved into the final position in the interaction region of the DORIS ring. In fall 2011, the complete experiment will be commissioned in advance of three months of dedicated data taking at an energy of 2.0 GeV in 2012.

6.3 Commissioning of OLYMPUS

The OLYMPUS target will be operational for background studies from early March 2011 until early July 2011. It is planned to measure the beam lifetime and background using test detectors with 4.5 GeV beam at greatly reduced target thickness (so that it does not affect the DORIS stored beam lifetime) in parallel with light source operation.

The commissioning of the OLYMPUS detector in park position with cosmic rays, test pulses, and sources is scheduled to begin in September 2010 and continue until the end of June 2011. The commissioning of the complete OLYMPUS experiment with beam will begin in August 2011 and continue until early November 2011. During this time this will be carried out in parallel with DORIS light source operation and in a dedicated mode during the service weeks.

6.4 Operation of OLYMPUS

To obtain the proposed results in Figure 1.8 will require 500 hours of data taking for each lepton sign at 2.0 GeV incident energy. Thus, a total of 1,000 hours of 100% efficient data taking is required. Assuming an efficiency of 50% for data taking, 2,000 hours or 3 months of dedicated DORIS operation at 2.0 GeV are requested for the OLYMPUS experiment. Approximately one moth of data taking is scheduled to begin in late January 2012. These data will be used to understand the systematic uncertainties and should produce a significant preliminary result on the cross-section ratio. In fall 2012, a further two months of data taking are planned to complete the OLYMPUS experiment.

Chapter 7

Expected Performance

7.1 Detector Resolutions

In order to study the proposed OLYMPUS detector performance the detector has been simulated in a GEANT4 Monte Carlo code. An *ep* elastic scattering event generator was used to simulate the events of interest. In order to study the response in all parts of the detector an isotropic angular distribution was employed rather than the correct cross section weighted distribution which would favour the forward angles. Realistic resolutions for all detectors were included in the Monte Carlo simulation.

To test that the resolutions and detector responses were reasonable the Monte Carlo was first run at the BLAST beam energy of 850 MeV. The resolutions obtained for momentum, angle (both polar and azimuthal), and vertex were consistent with what was obtained during the actual BLAST experiment.

At the OLYMPUS beam energy of 2 Gev the resolutions obtained from the Monte Carlo are shown in Figures 7.1, 7.2, 7.3, and 7.4 for the two cases of with and without the

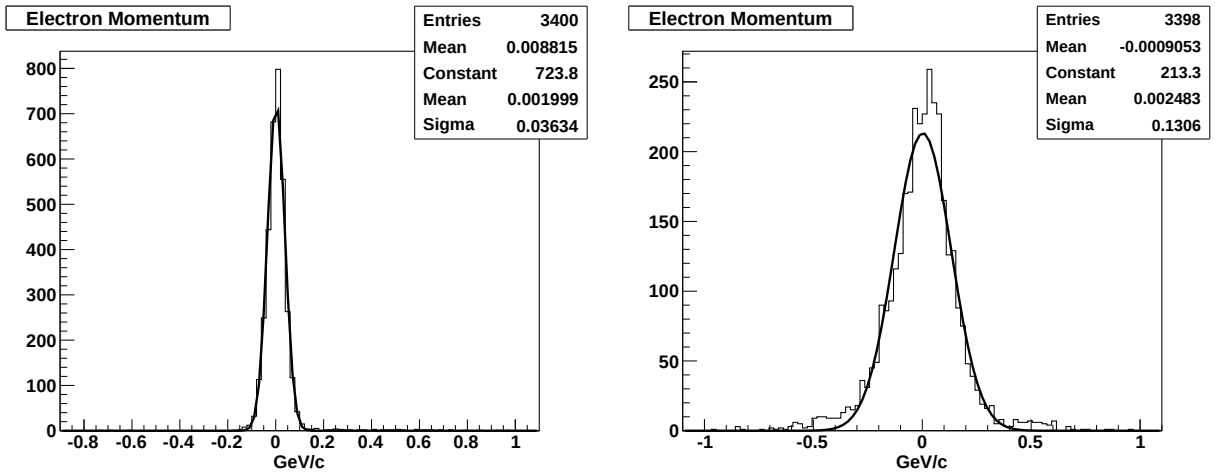

Figure 7.1: Deviation of the reconstructed electron momentum from the Monte Carlo generated momentum for the OLYMPUS detector with (left) and without (right) the proposed GEM tracking detector upgrade.

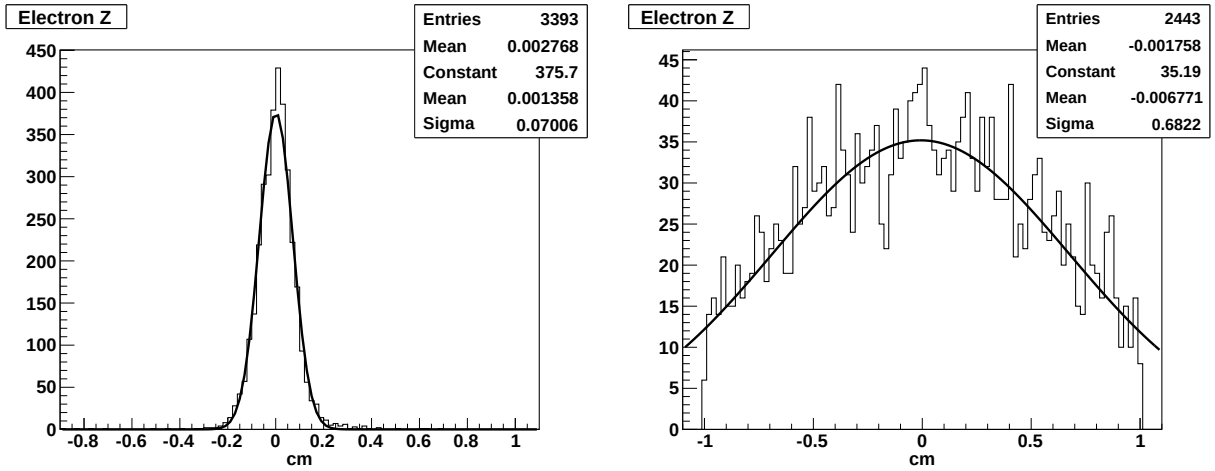

Figure 7.2: Deviation of the reconstructed electron vertex position from the Monte Carlo generated position for the OLYMPUS detector with (left) and without (right) the proposed GEM tracking detector upgrade.

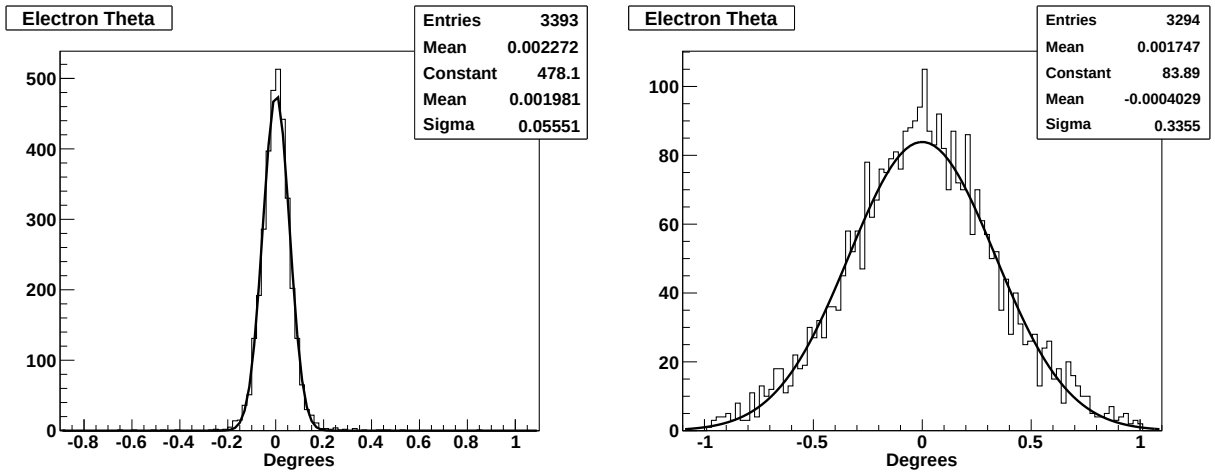

Figure 7.3: Deviation of the reconstructed electron polar scattering angle from the Monte Carlo generated angle for the OLYMPUS detector with (left) and without (right) the proposed GEM tracking detector upgrade.

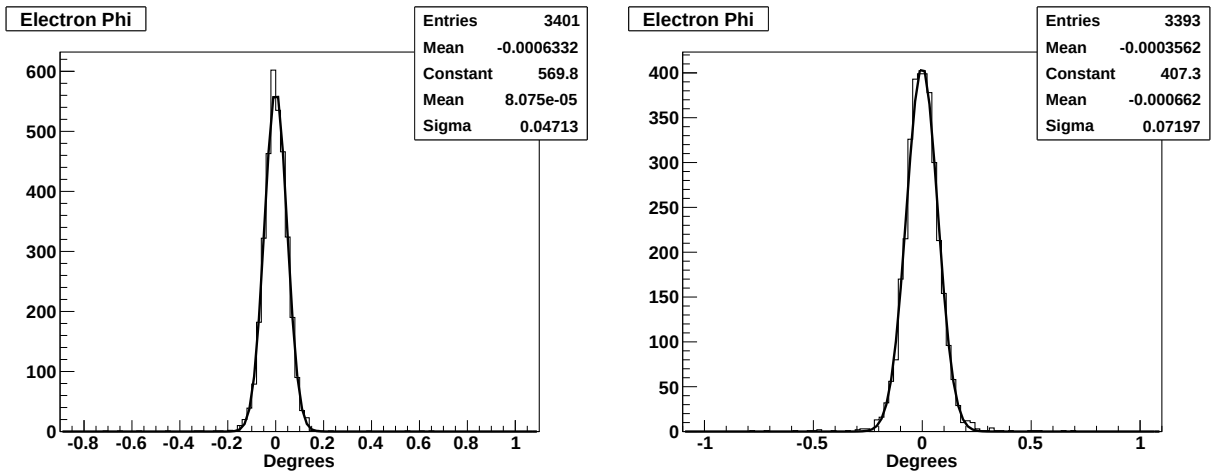

Figure 7.4: Deviation of the reconstructed electron azimuthal scattering angle from the Monte Carlo generated angle for the OLYMPUS detector with (left) and without (right) the proposed GEM tracking detector upgrade.

proposed GEM detector upgrade to the tracking. The resolutions shown are for reconstructing the scattered electron parameters but similar resolutions were obtained for the proton as well. The improvement with the GEM detector upgrade is significant.

The improvement in resolution for momenta, vertex position, and polar angle are important justifications for the GEM detector upgrade by themselves as they will permit tight cuts to be applied in the event selection to select only elastically scattered events and to reduce contributions from noise and backgrounds like pion production.

However, another very significant benefit from the GEM detector upgrade is in identifying tracks and determining initial parameters for the track reconstruction itself. As has been mentioned previously, the BLAST track reconstruction suffered from the limited number of space points (effectively only three) with which to fit the track paramters. With only three (effective) space points hits near the true hits from other tracks or noise could also reconstruct to false but reasonable tracks which contributed to backgrounds, poor resolutions, and misidentified kinematic events. The GEM detector upgrade helps solve this problem in two ways.

Firstly, with a fourth space point false tracks immediately have a large χ^2. (Note with only three effective space points any set of three reasonable points can be fit with a small χ^2.) This helps not only with the reconstruction but allows a measure of the reconstruction accuracy and can be used in calibrating such things as wire positions, time to drift distance, timing offsets, etc. using the experimental data.

Secondly, the addition of the GEM detector provides an immediate and surprisingly accurate set of starting values with which to perform the track fitting. Because there is relatively little magnetic field between the target, GEM detector, and first wire chamber this track segment is quite straight. Thus, fitting a straight line to the combinations of GEM hits and hits in the first wire chamber gives a good measure of the vertex position, and polar and azimuthal scattering angles. This is illustrated in figure 7.5 which shows the difference in scattering angles obtained from a simple straight line fit between the GEM

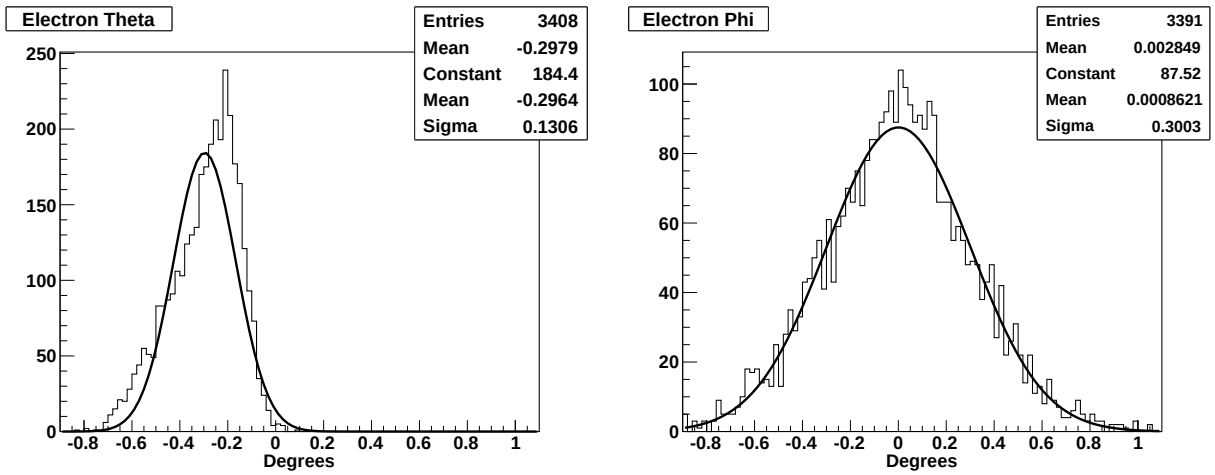

Figure 7.5: Deviation of the scattering angles, polar (left) and azimuthal (right), obtained from a straight line fit to the hits in the GEM detector and the first wire chamber from the Monte Carlo generated angles.

detector and the first wire chamber and the angles generated by the Monte Carlo. Note there is a small offset from zero for the polar angle because the magnetic field is not completely negligible but this can be paramterised and accounted for in the reconstruction. Similar results are obtained for the vertex position. With three of the four variables (p, z, θ, and ϕ) determined in this very simple and quick manner track reconstruction immediately gets very good starting values for the fitting procedure. If we add that elastic kinematics also fixes the momenta from the polar angle then excellent starting values for all four variables are provided and track fitting and selection even in a noisy environment is greatly simplified.

In addition to resolution studies the Monte Carlo will be used to study the statistics and systematics for the proposed OLYMPUS measurements. Using the realistic cross section weighted *ep* elastic event generator a realistic simulation of the experiment can be performed including event rates in the luminosity detector required for normalisation and the statistics in the main detector particularly at backward angles where the statistics will be limited by luminosity. This can be done for both electron and positron scattering and with opposite polarities for the toroidal magnetic exactly as will be done in the actual experiment.

The Monte Carlo will also be used to optimise the detector components and minimise background. For example, the showering of particles in the collimator, beampipe, or target cell walls can be simulated using a generator to simulate the beam halo and off-momentum particles striking the beamline elements. Moller and Bhabha event generators can also be used to study background produced from these reactions.

7.2 Backgrounds

The backgrounds in an internal gas target experiment at multi-GeV energies are well understood in experiments designed and successfully carried out by members of the collaboration. From both the BLAST (incident energy 0.85 GeV) and HERMES (incident energy 27 GeV) experiments, it is known that the backgrounds arise from the following sources:

1. showering of beam particles in the beam pipe, in the target cell, and in the vicinity of the experiment;

2. synchrotron radiation production in magnetic elements upstream of the experiment;

3. scattering from the atomic electrons in the target gas, *i.e.* Moller/Bhabha scattering;

4. electroproduction processes from the target.

Item 1 is suppressed by the presence of the fixed collimator directly in front of the target cell, the movable beam scrapers in the storage ring, and by careful tuning of the stored beam using scintillators and detectors near the internal target. Further, the toroidal magnetic field shields the detectors from electromagnetic shower products.

Item 2 produces low energy photons which are prevented from striking the target cell by means of the fixed collimator.

Item 3 produces a high rate of scattered leptons. At large angles, the Moller/Bhabha leptons have low energies and do not make it out of the target. At forward angles their energies approach half of the incident beam energy but are peaked within $\theta \approx 1/\gamma$. The toroidal magnetic field and tracking chamber system of BLAST has been carefully designed so that Moller/Bhabha events are not a problem. The OLYMPUS trigger will demand a coincidence between scattered lepton and recoil proton in elastic scattering. The momenta and angles of both particles will be measured. Together with the constraints of coplanarity and common vertex there is a five-fold redundancy.

The primary background from item 4 is the (e,e'π^0) process through the first resonance state of the proton. Estimates indicate that this background is $< 1\%$ of the elastic rate.

In summary, the proposed OLYMPUS experiment with optimally designed fixed shielding, movable collimators and carefully tuned, stored DORIS beam together with the toroidal BLAST spectrometer and detectors allowing clean coincidence detection of the scattered lepton and recoil proton, will not be affected by background.

Chapter 8

Collaboration, Costs, and Schedule

8.1 The OLYMPUS collaboration

The collaboration of physicists, engineers, and students working on the OLYMPUS experiment is listed as follows:

Arizona State University: R. Alarcon
DESY: F. Brinker, J. Hauschildt, Y. Holler, and U. Schneekloth
Hampton University: M. Kohl
INFN, Bari: R. De Leo and E. Nappi
INFN, Ferrara: P. Ferretti Dalpiaz, P. Lenisa
INFN, Rome: D.M. Castelluccio, E. Cisbani, S. Frullani, F. Garibaldi, and L. Manfre
MIT: J. Bessuille, K. Dow, D. Hasell, J. Hays-Wehle, E. Ihloff, J. Kelsey, J. Matthews, R. Milner, R. Redwine, A. Schmidt, and E. Tolley
St. Petersburg Nuclear Physics Institute: S. Belostotski, A. Kisselev, P. Kravchenko, O.Miklukho, Yu.Naryshkin, D.Veretennikov
Universität Bonn: R. Beck, C. Funke, Ph. Hoffmeister, F. Klein, H. Schmieden, A. Winnebeck and N.N. (1 post-doc)
University of Colorado: E. Kinney
Universität Erlangen-Nürnberg: E. Steffens
University of Glasgow: R. Kaiser, G. Rosner, and B. Seitz
University of Kentucky: C. Crawford
Universität Mainz: S. Baunack, A. Denig, D. von Harrach, F. Maas, M. Ostrick, N.N. (1 post-doc), and N.N. (Ph.D. students)
University of New Hampshire: J. Calarco
Yerevan Physics Institute: N. Akopov, A. Avetisyan, G. Elbakian, H. Marukyan, G. Karyan, A. Movsisyan

The personnel committed to undertake the OLYMPUS experiment by category (faculty, total physicist, Ph.D. students, and engineers) is detailed in Table 8.1. For the physicists, the effort is assumed to be constant effort over the three years 2010-2012. Note that the physicist column includes the effort of faculty listed in the first column. The constant effort over the years 2010-2012 of 13.6 FTEs of Ph.D. physicist and 14 graduate students together

with the 12 FTE's of engineering is comfortably adequate to construct, transport, install, commission and carry out the OLYMPUS experiment according to the schedule.

8.2 Institutional responsibilities

The responsibilities of each institution are listed as follows:

Arizona State University: TOF support, particle identification
DESY: Modifications to DORIS accelerator and beamline, installation
Hampton University: Luminosity monitor
INFN, Bari: GEM Electronics
INFN, Ferrara: Target
INFN, Rome: GEM electronics
MIT: BLAST spectrometer, wire chambers, tracking upgrade, target, transportation to DESY, simulations
St. Petersburg Nuclear Physics Institute: Removal of ARGUS, installation, commissioning, and analysis
Universität Bonn: Trigger and data acquisition
University of Colorado: Wire chambers
Universität Erlangen-Nürnberg: Target
University of Glasgow: Data acquisition, particle identification
University of Kentucky: Simulations
Universität Mainz: Trigger, data acquisition, GEM detectors
University of New Hampshire: TOF scintillators
Yerevan: Removal of ARGUS, installation, commissioning, and running

8.3 Costs

In converting from Euros to U.S. dollars, a conversion factor of 1.4 has been used.

8.3.1 Equipment costs

The equipment necessary to undertake the OLYMPUS experiment is costed in Table 8.2

8.3.2 Operating costs

The running costs for the OLYMPUS experiment are summarized in Table 8.3. With a total operating cost of about $ 900,000 over the lifetime of the experiment and approximately 50 Ph.D. physicist authors on papers, the total operating cost per physicist is estimated at $ 18,000. It is anticipated that these costs will be paid over three fiscal years.

To reduce the costs to DESY associated with the modifications to DORIS and the realization of the necessary infrastructure, the OLYMPUS collaboration is contributing to the following tasks:

Institute Faculty	Physicist FTE	Ph.D. Student	Engineer FTE	Fraction Requested FTE
ASU:				
Alarcon	0.3	1		
DESY:				
Brinker, Holler, Schneekloth	2		3	
Hampton:				
Kohl	1.5	1		
Italian Groups:				
Cisbani, DeLeo, Ferretti Dalpiaz				
Frullani, Garibaldi, Lenisa, Nappi	2	2	3	2 Ph.D. stud.
MIT:				
Matthews, Milner, Redwine	3	2	1.5	1.5 Engineers
St. Petersburg:				
Belostotski, Miklukho, Naryshkin	1	1	3	3 Engineers
U. Bonn:				
Beck, Klein, Schmieden	1	1	0.5	1 p.d.
U. Colorado:				
Kinney	0.2			
U. Erlangen-Nürnberg:				
Steffens	0.1			
U. Glasgow:				
Kaiser,Rosner	0.3	1	0.5	1 p.d., 1 Ph.D. stud.
U. Kentucky:				
Crawford		1		
U. Mainz:				
Denig, Maas, Von Harrach	0.9	1	0.5	1 p.d., 1 Ph.D. stud.
U. New Hampshire				
Calarco	0.5	1		
Yerevan				
Akopov, Avetisyan,				
Elbakian, Marukyan	0.8	2		
Total	13.6	14	12	

Table 8.1: Personnel committed to the OLYMPUS experiment by institution.

EQUIPMENT	COST k$	INSTITUTION
target	500	MIT/DOE
BLAST toroid shipping	626	MIT/DOE
GEM tracking upgrade	95	MIT/DOE
luminosity monitor	125	Hampton/NSF
trigger electronics and DAQ	330	Bonn+Mainz/BMBF
Total	1676	

Table 8.2: Equipment required for the OLYMPUS experiment with costs by institution/funding agency.

Item	COST k$
electrical power (2.2 MW)	736
water cooling (30 kW)	10
gases (130000 l/month)	48
computing	95
Total	889

Table 8.3: Total operating costs for the OLYMPUS experiment.

- Removal of ARGUS - St. Petersburg and Yerevan
- Toroid cooling system - Mainz and Bonn
- Toroid power and cabling - MIT
- Polarity switches - Bonn and Mainz
- Vacuum system - MIT

8.4 Schedule

A detailed schedule to prepare, install, commission, and carry out the OLYMPUS experiment has been developed by the collaboration and DESY. It is described in Figs. 8.1- 8.4 below. It is constrained by the availability and running schedule of DORIS and takes into account the availability of technical manpower within the collaboration to carry out the required tasks. The schedule is summarized as follows:

- Remove ARGUS experiment in fall 2009
- Disassemble and ship the OLYMPUS detector in spring 2010
- Ship the OLYMPUS target, beamline, and luminosity monitor in fall 2010

- Modify the DORIS beamline and install the OLYMPUS target and luminosity monitor in winter 2010/11
- Commission the luminosity monitor in spring 2011
- Assemble the OLYMPUS detector in park position in spring 2011
- Commission the OLYMPUS detector in park position in spring 2011
- Install the complete OLYMPUS experiment in summer 2011
- Commission the OLYMPUS experiment with beam in fall 2011
- Take data in 2012 in two separate running blocks

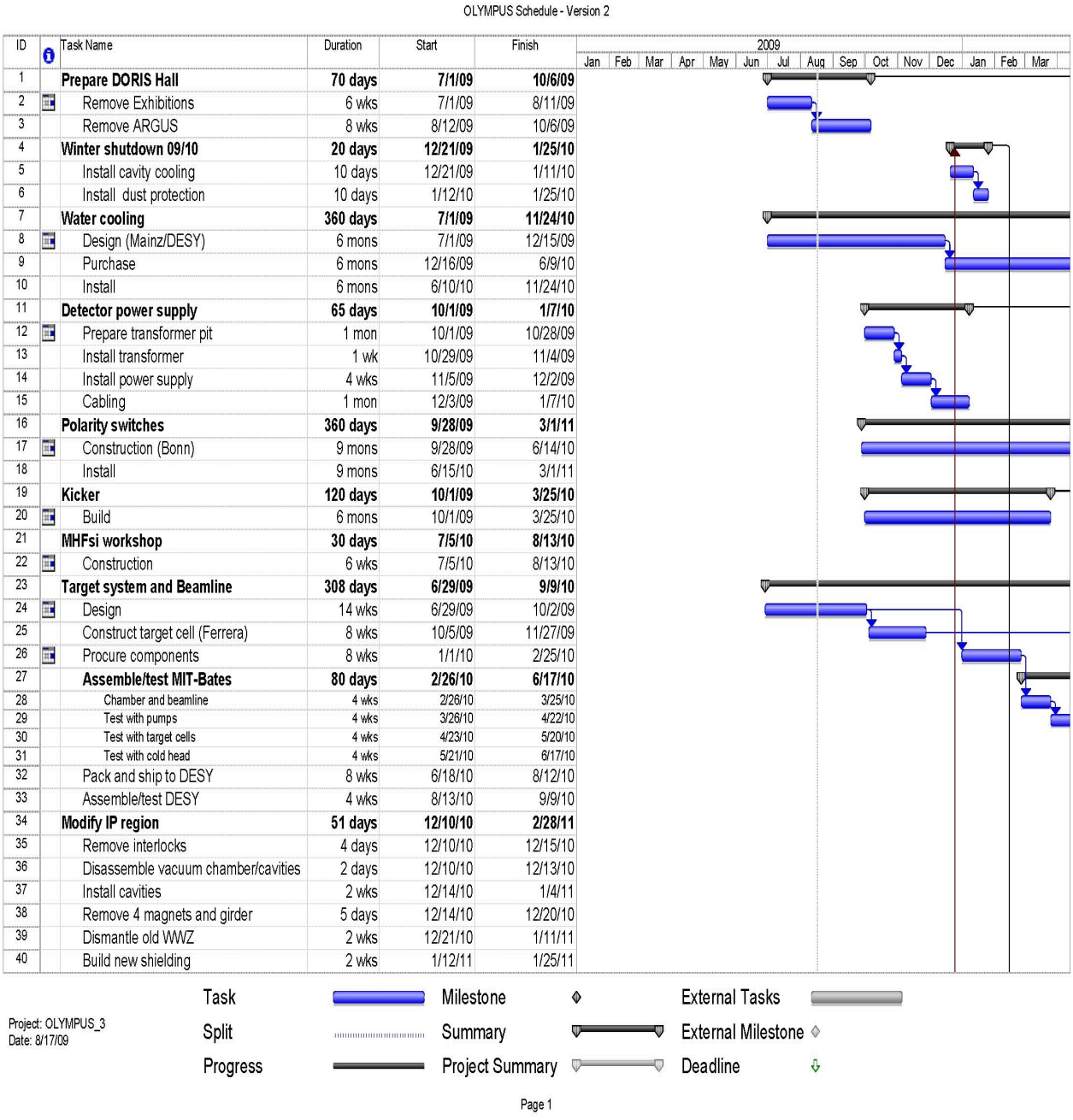

ID	Task Name	Duration	Start	Finish
1	**Prepare DORIS Hall**	**70 days**	**7/1/09**	**10/6/09**
2	Remove Exhibitions	6 wks	7/1/09	8/11/09
3	Remove ARGUS	8 wks	8/12/09	10/6/09
4	**Winter shutdown 09/10**	**20 days**	**12/21/09**	**1/25/10**
5	Install cavity cooling	10 days	12/21/09	1/11/10
6	Install dust protection	10 days	1/12/10	1/25/10
7	**Water cooling**	**360 days**	**7/1/09**	**11/24/10**
8	Design (Mainz/DESY)	6 mons	7/1/09	12/15/09
9	Purchase	6 mons	12/16/09	6/9/10
10	Install	6 mons	6/10/10	11/24/10
11	**Detector power supply**	**65 days**	**10/1/09**	**1/7/10**
12	Prepare transformer pit	1 mon	10/1/09	10/28/09
13	Install transformer	1 wk	10/29/09	11/4/09
14	Install power supply	4 wks	11/5/09	12/2/09
15	Cabling	1 mon	12/3/09	1/7/10
16	**Polarity switches**	**360 days**	**9/28/09**	**3/1/11**
17	Construction (Bonn)	9 mons	9/28/09	6/14/10
18	Install	9 mons	6/15/10	3/1/11
19	**Kicker**	**120 days**	**10/1/09**	**3/25/10**
20	Build	6 mons	10/1/09	3/25/10
21	**MHFsi workshop**	**30 days**	**7/5/10**	**8/13/10**
22	Construction	6 wks	7/5/10	8/13/10
23	**Target system and Beamline**	**308 days**	**6/29/09**	**9/9/10**
24	Design	14 wks	6/29/09	10/2/09
25	Construct target cell (Ferrera)	8 wks	10/5/09	11/27/09
26	Procure components	8 wks	1/1/10	2/25/10
27	**Assemble/test MIT-Bates**	**80 days**	**2/26/10**	**6/17/10**
28	Chamber and beamline	4 wks	2/26/10	3/25/10
29	Test with pumps	4 wks	3/26/10	4/22/10
30	Test with target cells	4 wks	4/23/10	5/20/10
31	Test with cold head	4 wks	5/21/10	6/17/10
32	Pack and ship to DESY	8 wks	6/18/10	8/12/10
33	Assemble/test DESY	4 wks	8/13/10	9/9/10
34	**Modify IP region**	**51 days**	**12/10/10**	**2/28/11**
35	Remove interlocks	4 days	12/10/10	12/15/10
36	Disassemble vacuum chamber/cavities	2 days	12/10/10	12/13/10
37	Install cavities	2 wks	12/14/10	1/4/11
38	Remove 4 magnets and girder	5 days	12/14/10	12/20/10
39	Dismantle old WWZ	2 wks	12/21/10	1/11/11
40	Build new shielding	2 wks	1/12/11	1/25/11

Figure 8.1: OLYMPUS schedule, page 1.

OLYMPUS Schedule - Version 2

ID	Task Name	Duration	Start	Finish
41	Install new girder	5 days	1/26/11	2/1/11
42	Install 6 magnets	2 days	2/2/11	2/3/11
43	Install vacuum chamber	3 days	2/4/11	2/8/11
44	Install collimator	1 day	2/9/11	2/9/11
45	Measure and align	3 days	2/10/11	2/14/11
46	Interlock, emergency off, test	5 days	2/15/11	2/21/11
47	Interface with DORIS	1 wk	2/22/11	2/28/11
48	**Move OLYMPUS detector**	**300 days**	**1/4/10**	**3/7/11**
49	Disassemble at MIT-Bates	16 wks	1/4/10	4/23/10
50	Ship to DESY	4 wks	4/26/10	5/21/10
51	Assemble in park position	16 wks	5/24/10	9/10/10
52	Test detector components	12 wks	9/13/10	12/3/10
53	Test with toroid	12 wks	12/6/10	3/7/11
54	**Install OLYMPUS**	**25 days**	**7/11/11**	**8/12/11**
55	Disassemble interlocks	3 days	7/11/11	7/13/11
56	Remove shielding	3 days	7/14/11	7/18/11
57	Remove beamline	2 days	7/19/11	7/20/11
58	Roll in detector	1 day	7/21/11	7/21/11
59	Install cooling	2 days	7/22/11	7/25/11
60	Connect power supply	2 days	7/26/11	7/27/11
61	Install target chamber and beamline	1 day	7/22/11	7/22/11
62	Survey	2 days	7/25/11	7/26/11
63	Build shielding	3 days	7/27/11	7/29/11
64	Install interlocks, etc.	3 days	8/1/11	8/3/11
65	Test interlocks, etc.	2 days	8/4/11	8/5/11
66	Setup with DORIS	5 days	8/8/11	8/12/11
67	**Detector commissioning**	**65 days**	**8/15/11**	**11/11/11**
68	Parasitic and during service periods	13 wks	8/15/11	11/11/11
69	First data period	4 wks	1/31/12	2/27/12
70	Repair, upgrade, test	15 wks	2/28/12	6/11/12
71	Second data period	9 wks	10/22/12	12/21/12
72	Maintenance	22 days	12/23/11	1/30/12
73	**Synchrotron radiation runs**	**948 days**	**2/9/09**	**10/22/12**
74	2009	315 edays	2/9/09	12/21/09
75	2010	298 edays	2/15/10	12/10/10
76	2011/1	132 edays	3/1/11	7/11/11
77	2011/2	130 edays	8/15/11	12/23/11
78	2012	238 edays	2/27/12	10/22/12

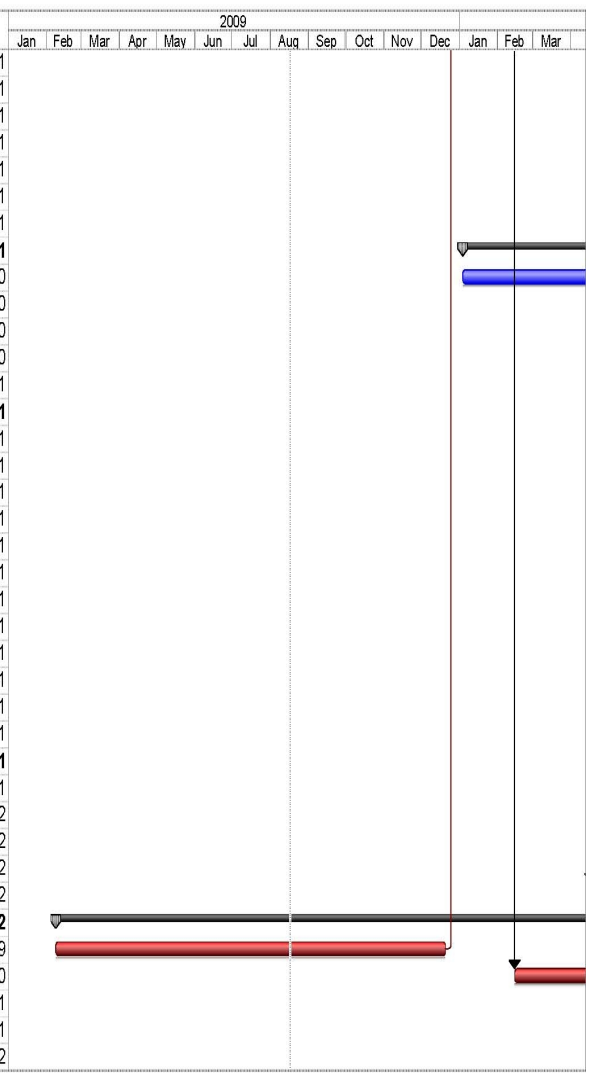

Project: OLYMPUS_3
Date: 8/17/09

Task
Split
Progress
Milestone
Summary
Project Summary
External Tasks
External Milestone
Deadline

Page 2

Figure 8.2: OLYMPUS schedule, page 2.

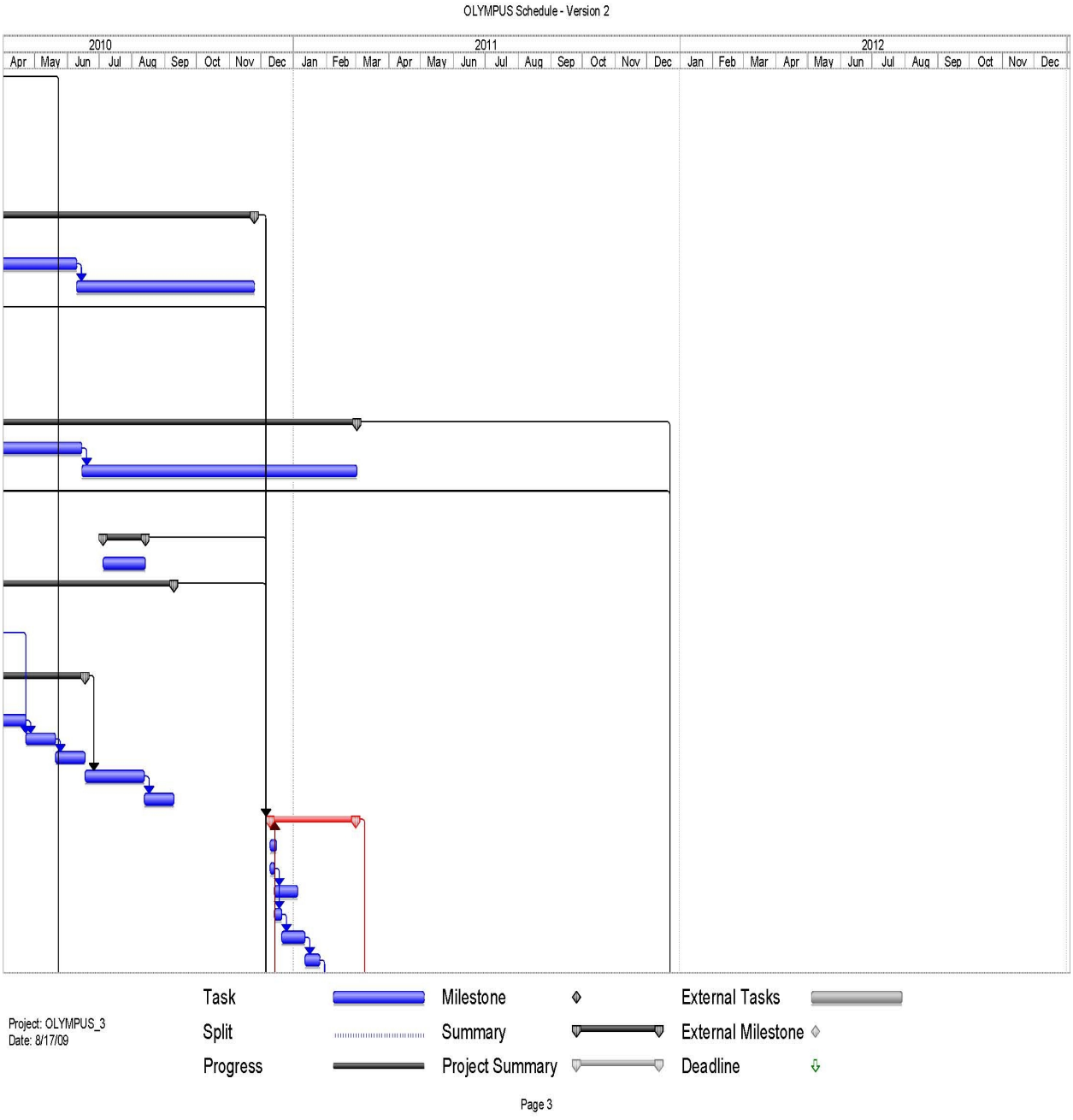

Figure 8.3: OLYMPUS schedule, page 3.

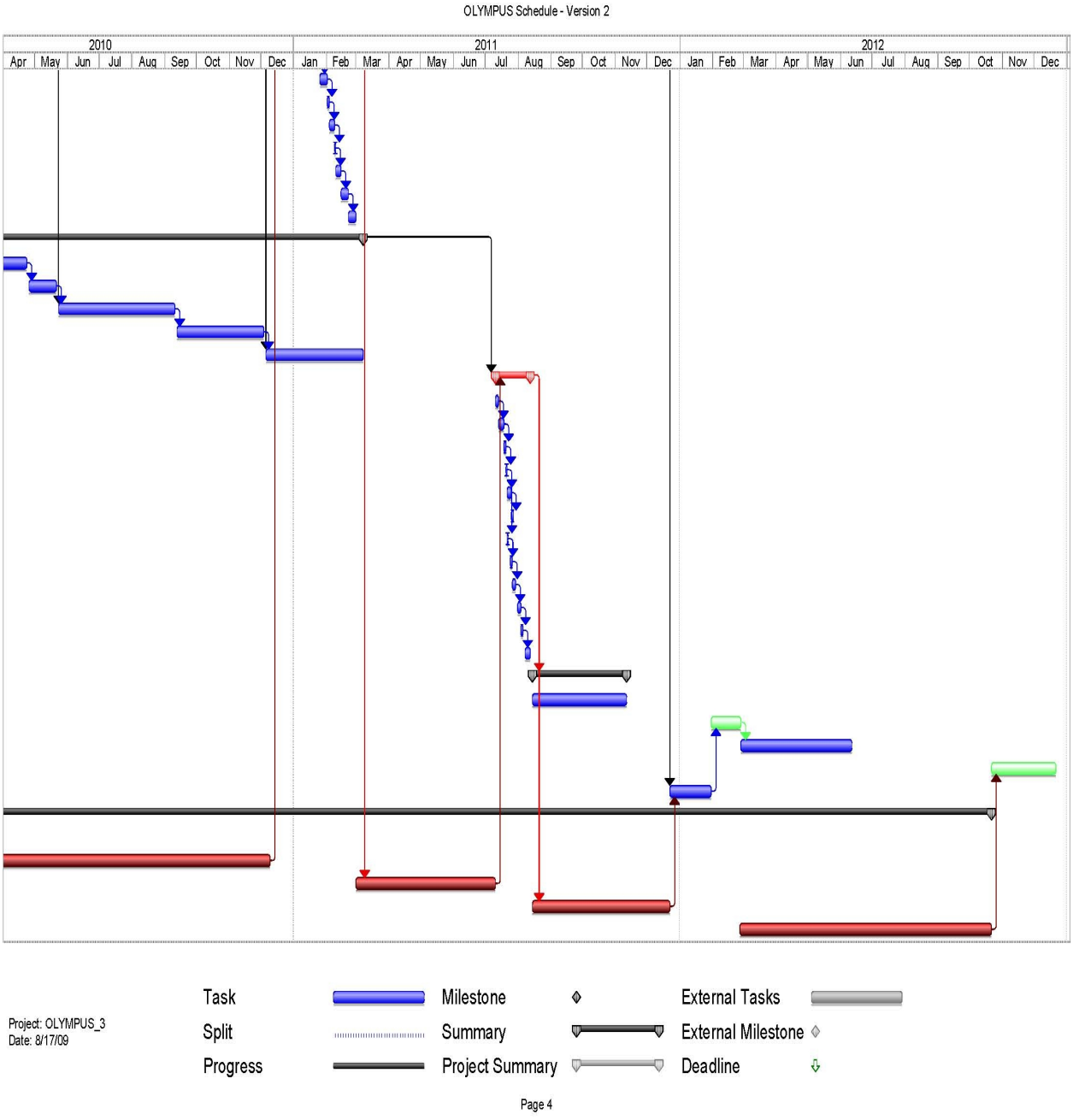

Figure 8.4: OLYMPUS schedule, page 4.

Bibliography

[1] D. Hasell *et al.*, Nucl. Instr. and Methods in Physics Research **A603**, 247 (2009).

[2] *A Proposal to Definitively Determine the Contribution of Multiple Photon Exchange in Elastic Lepton-Nucleon Scattering*, Proposal for the "OLYMPUS" experiment, submitted to DESY, Physics Research Committee, September 2008, `http://web.mit.edu/OLYMPUS`.

[3] R. Hofstadter, Rev. Mod. Phys. **28**, 214 (1956).

[4] M. Goeckeler *et al.*, Phys. Rev. **D71**, 034508 (2005); R.G. Edwards, Nucl. Phys. **B140**(Proc. Suppl.), 290 (2005); J.D. Ashley *et al.*, Eur. J. Phys. **A19**(Suppl. 1), 9 (2004); H.H. Matevosyan *et al.*, Phys. Rev. **C71**, 055204 (2005).

[5] M.N. Rosenbluth, Phys. Rev. **79**, 615 (1950).

[6] R.C. Walker *et al.*, Phys. Rev. D **49**, 5671 (1994); L. Andivahis *et al.*, Phys. Rev. D **50**, 5491 (1994); F. Borkowski *et al.*, Nucl. Phys. **A222**, 269 (1974); Nucl. Phys. **B93**, 461 (1975); W. Bartel *et al.*, Nucl. Phys. **B58**, 429 (1973); C. Berger *et al.*, Phys. Lett. **B35**, 87 (1971); J. Litt *et al.*, Phys. Lett. **B31**, 40 (1970); W. Bartel *et al.*, Phys. Lett. **B25**, 236 (1967); T. Janssens *et al.*, Phys. Rev. **142**, 922 (1966).

[7] M.E. Christy *et al.*, Phys. Rev. **C70**, 015206 (2004).

[8] I.A. Qattan *et al.*, Phys. Rev. Lett. **94**, 142301 (2005).

[9] V. Punjabi *et al.*, Phys. Rev. **C71**, 055202 (2005); Erratum-ibid. Phys. Rev. **C71**, 069902(E) (2005); M. Jones *et al.*, Phys. Rev. Lett. **84**, 1398 (2000); O. Gayou *et al.*, Phys. Rev. Lett. **88**, 092301 (2002); G. MacLachlan *et al.*, Nucl. Phys. **A764** , 261 (2006).

[10] G. Ron *et al.*, nucl-ex/0706.0128; B. Hu *et al.* Phys. Rev. C **73**, 064004 (2006); S. Strauch *et al.*, Phys. Rev. Lett. **91**, 052301 (2003);

[11] B. Milbrath *et al.*, Phys. Rev. Lett. **80** , 452 (1998); Erratun-ibid. Phys. Rev. Lett. **82**, 2221(E) (1999).

[12] S. Dieterich *et al.*, Phys. Lett. **B500**, 47 (2001).

[13] T. Pospischil *et al.*, Eur. Phys. J. **A12** , 125 (2001).

[14] O. Gayou *et al.*, Phys. Rev. **C64**, 038202 (2001).

[15] M.K. Jones, *et al.*, Phys. Rev. C **74**, 035201 (2006).

[16] C.B. Crawford *et al.*, Phys. Rev. Lett. **98**, 052301 (2007).

[17] J. Friedrich and Th. Walcher, Eur. Phys. J. A **17**, 607 (2003).

[18] J.J. Kelly, Phys. Rev. C **70**, 068202 (2004).

[19] R. Bijker and F. Iachello, Phys. Rev. **C69**, 068201 (2004).

[20] F. Iachello, A.D. Jackson, and A. Lande, Phys. Lett. **B43**, 191 (1973).

[21] J. Arrington, Phys. Rev. **C69**, 022201(R) (2004).

[22] J. Arrington *et al.*, *A measurement of two-photon exchange in unpolarized elastic electron-proton scattering*, Jefferson Lab Proposal E05-017 (2005).

[23] C. Perdrisat *et al.*, Jefferson Lab Proposals E01-109, E04-108.

[24] J. Arrington *et al.*, Conceptual Design Report CD0, Hall C 12 GeV Upgrade (2002).

[25] P.A.M. Guichon and M. Vanderhaeghen, Phys. Rev. Lett. **91**, 142303 (2003); P.G. Blunden, W. Melnitchouk, and J.A. Tjon, Phys. Rev. Lett. **91**, 142304 (2003); M.P. Rekalo and E. Tomasi-Gustafsson, Eur. Phys. J. **A22**, 331 (2004); Y.C. Chen, A.V. Afanasev, S.J. Brodsky, C.E. Carlson and M. Vanderhaeghen, Phys. Rev. Lett. **93**, 122301 (2004); A.V. Afanasev and N.P. Merenkov, Phys. Rev. **D70**, 073002 (2004).

[26] J. Arrington, Phys. Rev. **C71**, 015202 (2005).

[27] P.G. Blunden, W. Melnitchouk, and J.A. Tjon, Phys. Rev. **C72**, 034612 (2005).

[28] P. Bosted, Phys. Rev. **C51**, 409 (1995).

[29] J. Mar *et al.*, Phys. Rev. Lett. **21**, 482 (1968).

[30] J. Arrington *et al.*, *Beyond the Born Approximation: A Precise Comparison of e^+p and e^-p Elastic Scattering in CLAS*, PR04-116, PAC26 (2004)

[31] J. Arrington *et al.*, *Two photon exchange of electrons/positrons on the proton*, Proposal at VEPP-3, nucl-ex/0408020 (2004).

[32] S. Kowalski *et al.*, *Measurement of the Two-Photon Exchange Contribution in ep Elastic Scattering Using Recoil Polarization*, Jefferson Lab Proposal E04-019 (2004).

[33] D.J. Margaziotis *et al.*, *Measurement of the Target Single-Spin Asymmetry in Quasi-Elastic $^3He^{\uparrow}$(e,e')*, Jefferson Lab Proposal E05-15, PAC27 (2005).

[34] Y.C. Chen, C.W. Kao, and S.N. Yang, Phys. Lett. **B652**, 269 (2007).

[35] P.G. Blunden, W. Melnitchouk, and J.A. Tjon, Phys. Rev. C **72**, 034612 (2005).

[36] S. Kondratyuk, P. Blunden, W. Melnitchouk, and T.A. Tjon, Phys. Rev. Lett. **95**, 172503 (2005).

[37] D. Borisyuk and A. Kobushkin, Phys. Rev. C **78**, 025208 (2008).

[38] M. Gorchtein, Phys. Lett. **B644**, 322 (2007).

[39] Y.C. Chen, A.V. Afanasev, S.J. Brodsky, C.E. Carlson and M. Vanderhaeghen, Phys. Rev. Lett. **93**, 122301 (2004); A.V. Afanasev, S.J. Brodsky, C.E. Carlson, Y.-C. Chen, and M. Vanderhaeghen, Phys. Rev. D **72**, 013008 (2005).

[40] N. Kivel and M. Vanderhaeghen, hep-ph/0905_0282v1.

[41] D. Cheever *et al.*, Nucl. Instr. Meth. **A556** , 410 (2006).

[42] F. Weissbach *et al.*, Eur. Phys. J. **A30**, 477 (2006).

[43] B. Nagorny, "Synchrotron radiation incident on the OLYMPUS experiment", presentation to the OLYMPUS collaboration, April 2009.

[44] B. Nagorny, private communication, calculation of synchrotron radiation at 2 GeV incident on OLYMPUS, July 2009.

[45] Axel, Schmidt, "Synchrotron radiation and the positioning of scrapers and collimatorsin the OLYMPUS experiment", OLYMPUS technical report no. 1, August 2009.

[46] M. Sands, "The physics of electron storage rings, an introduction", SLAC technical report no. 121, 1970.

[47] See information on DORIS at http://doris.desy.de.

[48] F. Brinker, "DORIS operation for the OLYMPUS experiment", presentation to OLYMPUS collaboration meeting, April 2009.

[49] C. Tschalaer, private communication.

[50] C. Altunbas *et al.*, Nucl. Instr. Meth. **A490**, 177 (2002).

[51] F. Simon *et al.*, arXiv:0808.3477v1, submitted to Nucl. Instr. Meth.

[52] G. Höhler *et al.*, Nucl. Phys. **B114**, 505 (1976).

[53] K. Dow *et al.*, to be published.

[54] F. Sauli, "GEM: A new concept for electron amplification in gas detectors", Nucl. Instr. and Meth. **A386**, 531 (1997).

[55] M.C. Altunbas *et al.*, "Construction, test and commissioning of the triple-GEM tracking detector for COMPASS", Nucl. Instr. and Meth. **A490**, 177 (2002).

[56] C. Altunbas *et al.*, Nucl. Instr. Meth. **A490**, 177 (2002).

[57] F. Simon, J. Kelsey, M. Kohl, R. Majka, M. Plesko, T. Sakuma, N. Smirnov, H. Spinka, B. Surrow, and S. Underwood, arXiv:0808.3477v1, Nucl. Instr. and Methods in Physics Research **A598**, 432 (2009).

[58] D. DeSchepper *et al.*, Nucl. Instr. and Meth. A **419**, 16 (1998).

[59] D. Cheever *et al.*, Nucl. Instr. and Meth. A **556**, 410 (2006).

[60] C. Bloch *et al.*, Nucl. Instr. and Meth. A **354**, 437 (1995).